# CONTINUUM SUPERSONIC GAS JET ENHANCED FOCUSED ELECTRON BEAM INDUCED DEPOSITION

A Dissertation
Presented to
The Academic Faculty

by

Matthew Henry

In Partial Fulfillment
of the Requirements for the Degree
Doctor of Philosophy in the
School of Mechanical Engineering

Georgia Institute of Technology
August 2018

# CONTINUUM SUPERSONIC GAS JET ENHANCED FOCUSED ELECTRON BEAM INDUCED DEPOSITION

Approved by:


Dr. Andrei Fedorov, Advisor
School of Mechanical Engineering
*Georgia Institute of Technology*

Dr. Vladimir Tsukruk
School of Materials Science and Engineering
*Georgia Institute of Technology*

Dr. Cyrus Aidun
School of Mechanical Engineering
*Georgia Institute of Technology*

Dr. Seung Soon Jang
School of Materials Science and Engineering
*Georgia Institute of Technology*

Dr. Satish Kumar
School of Mechanical Engineering
*Georgia Institute of Technology*


Date Approved: [May 25, 2018]

To my wife, without whose love, support, and inexhaustible patience, I could not have made it.

## ACKNOWLEDGEMENTS

I am thankful to Dr. Fedorov who has invested a great deal into the success of my research despite many setbacks. I am grateful to the support of our lab group and campus community, in particular Dr. Kim Songkil and Mason Chilmonczyk, who directly contributed to my research.

# TABLE OF CONTENTS

## LIST OF TABLES

## LIST OF FIGURES

## LIST OF SYMBOLS AND ABBREVIATIONS

### Abbreviations

| | |
|---|---|
| AFM | Atomic Force Microscope |
| BGK | Bhatnagar Gross Krook |
| DSMC | Direct Simulation Monte Carlo |
| EDX | Energy-Dispersive X-ray |
| ESEM | Environmental Scanning Electron Microscope |
| FEBID | Focused Electron Beam Induced Deposition |
| FIBID | Focused Ion Beam Induced Deposition |
| ID | Inner Diameter |
| MOC | Method of Characteristics |
| OD | Outer Diameter |
| RMS | Root-Mean-Square |
| RMSD | Root-Mean-Square Deviation |
| RTD | Resistance Thermal Detector |
| SEM | Scanning Electron Microscope |

### Symbols

| | |
|---|---|
| $R_U$ | Universal Gas Constant |
| $\mu_k$ | Kinematic Viscosity |
| $\mu$ | Mean Velocity |
| Kn | Knudsen Number |
| $k_B$ | Boltzmann Constant |
| $P$ | Pressure |

| | |
|---|---|
| $T$ | Temperature |
| $\gamma$ | Isentropic Expansion Coefficient |
| $M$ | Molar Mass |
| $L$ | Length |
| $F$ | Weighting Factor |
| $\Delta t$ | Simulation Time Step |
| $\sigma$ | Standard Deviation of Velocity |
| $\sigma_{ab}$ | Collisional Cross-Section |
| $V$ | Velocity |
| $N_R$ | Number of Real Particles |
| $N_S$ | Number of Simulation Particles |
| $\forall$ | Volume |
| $m$ | Mass of a Real Particle |
| $H$ | Couette Flow Gap Size |

## SUMMARY

The unconventional approach of using a continuum, rather than molecular, gas jet to deliver precursor deposition molecules is presented for the enhancement of Focused Electron Beam Induced Deposition (FEBID) in terms of significantly increasing the precursor injection rate, enhancing surface diffusion, and increasing as-deposited deposition purity. This thesis presents careful investigation of these enhancements by experiment, theory, and computational simulations and models. Use of argon as a carrier gas in the continuum flow regime through a 75$\mu m$ nozzle, results in an injection rate of the organometallic deposition precursor tungsten hexacarbonyl that is four orders of magnitude greater than the precursor gas alone injected through a 455$\mu m$ nozzle. The continuum flow regime also narrows the velocity distribution of impinging gas particles, and that velocity may be tuned by nozzle temperature – either decreasing the temperature to increase sticking and prevent desorption, or increasing the temperature to increase surface diffusion (continuum jet induced 10x increase in surface diffusion) and deposition purity (heated continuum jet resulted in 95% tungsten purity as deposited).

In order to analyze the effects of a continuum gas jet, a Direct Simulation Monte Carlo (DSMC) algorithm was developed to predict the complex flow structure developing due to a more localized and higher density flow emanating from a gas jet in the continuum flow regime. A novel adaptive algorithm was developed for DSMC to allow the simulation to efficiently and accurately simulate flows with Knudsen numbers varying from O(0.01) (continuum flow) to O(10) (molecular flow) in a single simulation. Surface impingement data provided by the DSMC algorithm was used in numeric integration of the hard-cube model to accurately predict the surface thermal responses to jet impingement as measured

by a microscale Resistance Thermal Detector (RTD). Because the measured and predicted surface thermal response is inadequate to yield measurably enhanced diffusion, the gas jet must induce an effective adatom temperature that drastically differs from the surface temperature. Therefore, the hard-cube model was used to calculate, for the first time, the spacial distribution of the effective temperature of the adsorption layer. This adsorption layer effective temperature is the key to understanding and controlling the enhanced diffusion and enhanced deposition purity effects achieved *via* continuum flow gas jet injection.

# CHAPTER 1: INTRODUCTION

Focused Electron Beam Induced Deposition (FEBID) is a process of additive nano-scale fabrication. A typical configuration for FEBID is illustrated in Figure 1.1. Vapor phase of a deposition precursor material is delivered to the deposition region through a nozzle approximately 0.5*mm* in diameter. Depending on material properties and the substrate temperature, a fraction of precursor molecules – known as the sticking coefficient – will adsorb to the substrate. The adatoms are then subject to surface diffusion along and desorption from the surface. The electron beam interacts with the solid surface to generate low-energy secondary electrons that dissociate precursor molecules such that the material of interest will chemisorb to the substrate and other materials of the precursor molecule either desorb or become entrapped as contaminants in the deposit.

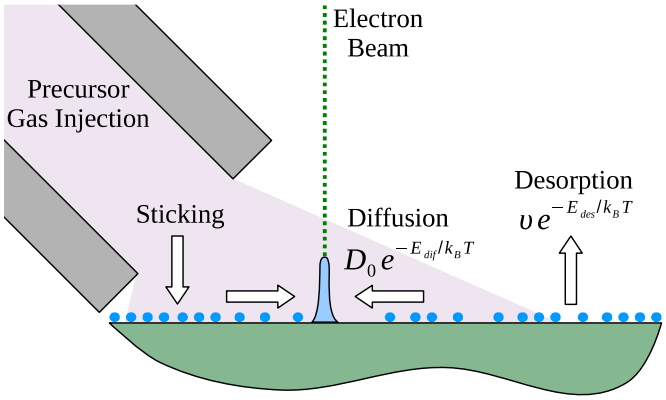


***Figure 1.1: Typical FEBID configuration***

Applications of interest in FEBID are too varied and diverse to meaningfully summarize. One of which is the development of 3D nanomagnetic logic in which exploit the nanoscale size effects that alter the behavior of magnetic materials [1]. Another is the fabrication of multilayer superconducting structures [2][3][4]. An additional example

follows from the observation that, charge transport in nano-granular FEBID structures is dominated by tunneling, which has an exponential dependence on inter-grain distance. Therefore, such structures are highly sensitive to strain and may be incorporated into MEMS sensors [5]. The range of potential applications is multiplied by techniques such as co-deposition in which two precursors are injected *via* the same or separate nozzles [6][7][8][9][10], or injection is pulsed between precursor materials, allowing time for two subsequent layers of different materials to intermix under electron irradiation [11][12]. The ability adjust the relative concentrations of two deposition species allows researchers to change to composition, lattice structure, or electrical and magnetic properties of the deposit.

These developments are despite initial application of FEBID being limited due to poor deposit purity and a low deposition rate as compared to focused ion beam induced deposition [13]. Part of this problem is that FEBID precursor molecules are usually developed for chemical vapor deposition and do not efficiently dissociated by electron beam. However, there is strong interest in addressing these problems because FEBID greater resolution capability and neither subjects the substrate to ion implantation nor surface destruction due to ion bombardment, which can be destructive in the fabrication of MEMS devices. The deposition rate for FEBID can be increased by increasing the supply rate of precursor molecules, which also increases the deposition aspect ratio when the precursor supply rate is high relative to electron beam current. This has been achieved by cryogenically cooling the substrate to increase the sticking coefficient, resulting in unusual deposit morphology [14][15]. This has the adverse effect of also decreasing the adatom diffusion rate, which requires the electron beam to raster across the surface rather than form

a desired 3D structure. An alternative approach is the introduction of liquid suspended precursor to the substrate, which offers a much higher density of precursor molecules. Dissociation can occur in the path of the beam throughout the height of the thin liquid film, allowing a segment of deposition to grow simultaneously rather than exclusively at the base [16][17].

Greater focus has been applied to improving deposition purity. The initial approach has been post-deposition annealing, which was successfully done to purify FEBID platinum [18]. Similar post-treatment results have been obtained by electron irradiation with exposure to a reactive gas, such as oxygen or water vapor [19][20][21][22][23]. However, post-treatment processes tend to alter deposit morphology and introduce voids. In-situ avert this problem. Laser pulses alternated with the electron beam provided sufficient heating to drive of contaminant ligands, but not so much as to induce pyrolysis of undeposited surface adsorbed precursor molecules [24][25]. Similarly, deposition in the presence of the reactive gas, oxygen, produces void-free, high-purity metal deposits [26].

The ability to design FEBID processes remains limited as much of the process is poorly understood. The best understood aspect is the interaction between the electron beam and the substrate in the generation of secondary electrons. The importance of this step was recognized early on and it can be effectively simulated by Monte Carlo [27]. The sticking coefficient is best estimated by the hard-cube model [28], yet does not appear to have ever been applied. Instead, attempts are made to directly measure the sticking coefficient for specific cases with little ability extrapolate to general application [29]. This surface diffusion and desorption rates are generally regarded in the Arrhenius form, but recent

work is investigating the mobility and stability of adatoms *via* DFT. In concert, these parameters can be used in the reaction-diffusion equation coupled with the electron trajectory Monte Carlo to reasonably reproduce experimental deposition rates and morphologies [30][31][32][33]. Improved theoretical understanding of these phenomena will improve the predictive ability of simulations.

In tangent to the significant progress being made in improving the deposition rate, purity, and theoretical modeling of FEBID, further progress is being contributed in these areas by the unconventional technique of continuum gas jet injection. Precursor molecule vapor is introduced to a reservoir of carrier gas, such as argon, the two gases mix according to relative vapor pressures, and are accelerated together to choked flow at the injection nozzle. The nozzle diameter is reduced to below $100\mu m$ to maintain continuum flow at the exit at the desired flow rate, whereas molecular gas injection nozzles are typically $500\mu m$ in diameter. This decreases the surface area of gas impingement and increases the precursor supply rate, in one case by four orders of magnitude. The isentropic expansion of the continuum gas jet narrows the velocity distribution of impinging particles, which is tunable by choosing a carrier gas of greater or lesser mass, or by heating or cooling the nozzle to modulate the sticking coefficient. The continuum gas jet also stimulates enhanced surface diffusion to improve growth rate and enhanced desorption of contaminant radicals to enhance deposit purity. Modeling of the continuum gas jet interaction with the substrate – based on generalized material parameters rather than FEBID experiment-specific parameters – allows the effective temperature of surface adsorbed molecules to be predicted, in order to predict the surface diffusion rate. The model, verified by experiment, reveal that the substrate temperature is relatively unaffected by the gas jet, suggesting that

the sticking coefficient and surface diffusion rates may be controlled independently by two distinct temperatures.

# CHAPTER 2: TOWARDS USE OF INERT GAS JETS FOR GROWTH CONTROL IN ELECTRON BEAM INDUCED DEPOSITION

An inert, precursor free, argon jet is used to control the growth rate of FEBID. It is demonstrated that a change in the jet inlet temperature either increases surface diffusion to greatly enhance the deposition rate or depletes the surface precursor due to impact-stimulated desorption to minimize the deposition or completely clean the surface. Physical mechanisms for this process are described. It is also observed that the electron beam generates plasma upon interaction with an argon jet, and it is concluded that the potential effects of plasma do not substantially contribute to the enhanced deposition rate.

## 2.1 Motivation

FEBID is an emerging method for controlled deposition of topologically-complex nanostructures from a variety of materials. With a few notable exceptions [34], FEBID precursor material is supplied via gas impingement and adsorption to the surface during deposition [13] or it is applied to the surface prior to use in the scanning electron microscope (SEM) [35][36][37]. Adsorbed precursor is then transported to the deposit site by surface diffusion [38][39][40]. Nozzle injection is the favored method of precursor delivery because it applies a high concentration of precursor molecules to a localized area without significantly raising the chamber pressure or defocusing the beam [13]. A similar deposition process, focused ion beam induced deposition (FIBID), is often preferred over FEBID due to its higher deposition rate in the beam-limited growth regime [13][41]. It has, however, the disadvantages of surface damage, ion implantation, and a generally lower resolution [13]. By increasing the rate of precursor supply, one can allow for a higher beam current in beam-limited FEBID and therefore improve the achievable growth rate. Beam-

limited deposition is desirable both to minimize surface damage and to maximize resolution [13]. On the other hand, in SEM imaging, carbon film deposition from residual hydrocarbons is a significant problem that reduces the quality of images. Techniques have been developed to clean the surface, albeit with the potential to damage the surface, [42] and others to negate the effect of contaminant deposition in the imaging [43]. In this chapter, the use of an inert gas jet injection system is introduced for the specific purpose of modulating (increasing or decreasing) precursor supply *via* surface diffusion, and not the delivery of precursor molecules to the surface. This results in effects that would have direct impact on the above mentioned applications of focused electron beams.

## 2.2 Methods

In each set of experiments a nozzle injection system supplies a jet of pure argon gas (i.e., with no precursor) that alters the supply rate of an adsorbed paraffin precursor. The jet is injected through a $75\mu m$ inner diameter capillary onto the substrate surface at a rate of $1.26\times10^{-7} kg/s$. Paraffin was dissolved into methanol and placed on the silicon substrate one day prior to use in the SEM. All carbon deposits were grown in 10 minute intervals under identical beam settings of $25kV$ accelerating voltage and ~$90pA$ beam current. The reference deposits, shown in Figure 2.1.a, are formed without the jet. Figure 2.1.b shows pillars deposited while argon gas was injected from a reservoir at $20°C$. The growth of the reference deposits is diffusion-limited since an increase beam current does not increase the volume of the deposits. Therefore, an enhanced precursor supply rate must have been promoted by the jet to produce the larger pillars. The heights of the reference deposits (without a jet) are $2\mu m$, and the pillars formed with the use of an argon jet are ~$20\mu m$ high and grown at a deposition rate ten times greater than that of the baseline. With diameters

of ~200*nm*, the pillar aspect ratio is 100, which is difficult to achieve using conventional EBID methods with residual hydrocarbons. All deposits in Figure 2.1 are formed in the same area in rapid succession, and since the size of both the reference deposits and the pillars are consistent throughout, there is no observable precursor depletion.

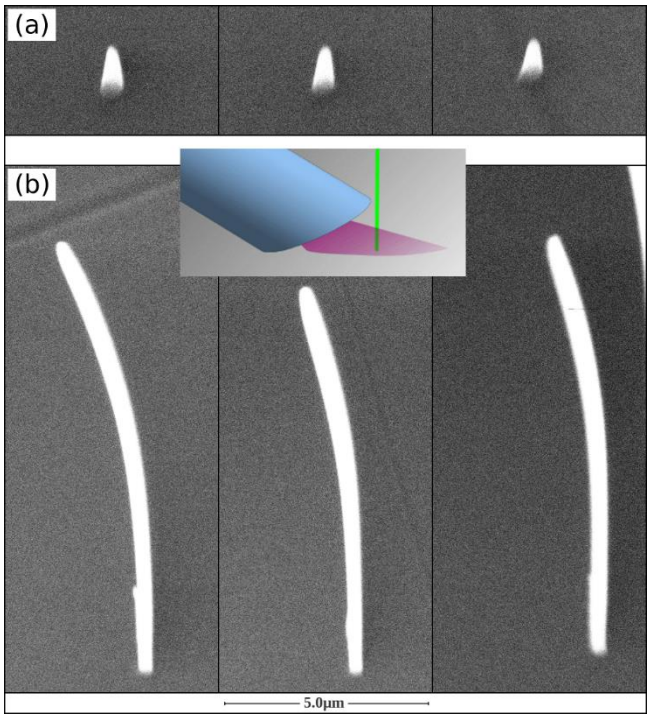


***Figure 2.1: 30° tilted views of deposits formed with (a) the jet off (reference control experiment) and (b) the jet on.***

The results of experiments with the 20°*C* gas reservoir indicate a greatly enhanced rate of FEBID growth. However, when the jet energy is increased (e.g., by increasing the temperature of the reservoir), the deposit growth rate is significantly diminished. This is first observed by heating the reservoir to 140°*C*, exposing the surface to the heated argon jet for 11 minutes, turning the jet off, and immediately forming an FEBID deposit. Each of these deposits shown in Figure 2.2.b is smaller than its preceding reference deposit (directly above it in Figure 2.2.a) that was formed at the same location with no jet treatment. The

temperature was chosen such that the depletion effect would be observable but not completely “clean-up” the surface such that no deposit could form. Next, the reservoir is heated to 200°*C* to demonstrate reduction of the jet-enhanced deposition in contrast to the first experiment. Figure 2.2.c shows subsequent pillars deposited 20$\mu m$ apart with the jet on. Similar to the first experiment, the jet increased precursor supply to the deposit and resulted in larger deposits, but as time proceeded, the precursor concentration became depleted and the rate of precursor supply, and in turn the deposit size, diminished.

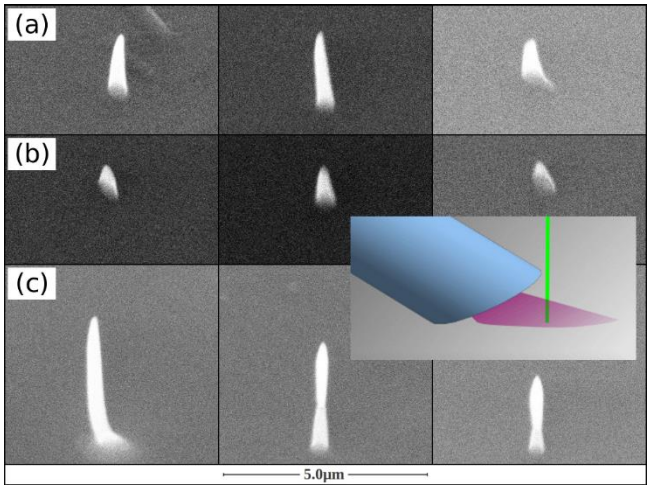


***Figure 2.2*: 30° tilted views of (a) deposits formed with jet off at a fresh location (b) deposits formed at a location partially depleted by 140°C gas jet (c) subsequent deposits (left to right) with 200°C gas jet.**

When an electron beam passes through an argon gas, it ionizes the gas to produce plasma [44]. It has been suggested that the plasma in chemical vapor deposition can be adjusted to increase the precursor surface mobility and therefore produce a more conformal surface deposit [45]. Photon impingement in particular has been considered as a mechanism to increase surface diffusion [46]. Alternatively, the kinetic energy of the argon bombardment has been identified as having key importance in argon plasma cleaning [47]

and may, at lower energies, enhance diffusion. In our setup, the mean free path of a primary electron through the argon jet is significantly greater than the cross-section of the jet, so only a small percentage of the beam is affected. The scattering events that do occur deduct energy on the order of tens of electron volts - a negligible portion of the primary electron's energy [43]. Also, when the $25keV$ primary electron beam passes through the argon jet, there is a negligible probability of it having a non-zero elastic [48] or inelastic [49] scattering angle. Therefore, the primary electron beam is effectively unchanged as it produces plasma in the described jet, but some of the secondary electrons and photons will reach the substrate in the area surrounding the deposit. The anticipated effect of these particles on the surface is that they may be absorbed to raise the local energy (temperature) and therefore increase the precursor diffusion coefficient, or they may dissociate precursor molecules - depleting the concentration. The other aspect of the plasma is ionized argon atoms in the jet. These represent a negligible proportion of the jet and their interactions are not expected to differ from the rest of the argon jet.

An experiment is constructed to determine the degree that plasma contributes to the enhanced deposition rate apart from argon impingement. The capillary is laid on its side on the substrate with the bottom of the $75\mu m$ orifice offset $32\mu m$ from the surface to produce a gas jet emanating from the nozzle parallel to the substrate surface. Then, the electron beam passes through the argon jet at the base of the capillary such that argon atoms do not strike the surface in the vicinity of the deposition, but the diffusely-scattered secondary electrons and photons do. The flux of the energetic plasma-generated particles to the surface may be reduced in this geometry, so the argon gas flow rate was increased to $3.56\times10^{-7} kg/s$ to compensate. Any net effect of the plasma shall result in either an

increased precursor supply due to enhanced surface diffusion or a decreased supply due to the surrounding precursor being dissociated. The deposits formed under the plasma jet in Figure 2.3.b are clearly shorter and broader than the reference deposits shown in Figure 2.3.a, but there is no significant difference in deposit volumes. In the diffusion limited-regime, assuming all deposits are of similar density, an increase in precursor supply must result in an increase in the material volume deposited. Since this is obviously not supported by experiments, plasma is not contributing in a measurable way to the observed effect. The broadening of deposits is due to defocusing of the beam as it passes through the dense jet, whereas in the prior experiments defocusing was negligible.

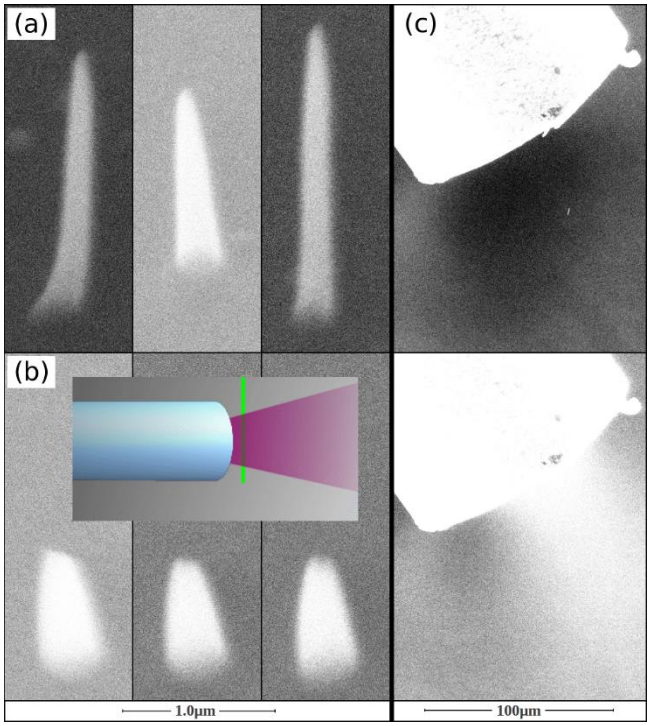


***Figure 2.3: 30° tilted views of (a) deposition with jet off (b) deposition with electron beam passing through the jet cross section (c) secondary electron 'glow' in the argon plasma compared to jet off***

Rather than plasma effects, it is expected that enhanced deposition is the result of jet impingement that delivers kinetic energy to the surface and, in turn, increases the energy (effective temperature) of the adsorbed precursor. The surface diffusion rate and the desorption rate, vary with temperature according to $\exp(-E_{dif}/k_BT)$ and $\exp(-E_{des}/k_BT)$ respectively. The activation energy of desorption $E_{des}$ is generally much greater than that of diffusion $E_{dif}$ [50], so an increase in temperature will increase diffusion more significantly than desorption at a lower temperature range, thereby providing precursor to the deposit more rapidly. Since the diffusion radius expands with time according to $(Dt)^{1/2}$, the area of the precursor consumed increases linearly with time. Therefore, the growth rate of the pillars in the diffusion dominated regime should be constant as was observed in Figure 2.1.b. This is true when the duration of the experiment is small compared to the desorption time scale. On the other hand, a more energetic jet impinging on the surface leading to a higher effective temperature will increase the rate of desorption and reduce the desorption time scale. As a result, desorption continually depletes the precursor molecules from the surface such that the rate of precursor supply by diffusion also diminishes with time. This, in turn, yields a diminishing growth rate as observed in Figure 2.2.c. Similar reasoning was taken by Wei, et al. to explain rates of deposit growth around a heated carbon nanotube [51].

The same enhanced diffusion and desorption can be achieved by heating the entire substrate [52]. However, since the thermal mass of a thin film of adsorbed precursor molecules is negligibly small, the effective temperature of the precursor can be changed rapidly and locally as soon as the jet is applied. When the jet is removed, the heat quickly dissipates into the substrate. As a result, an impinging gas jet allows for a quick-switching

FEBID process control that can locally activate and deactivate enhanced surface diffusion without the latency inherent in changing the bulk substrate temperature. In addition, by increasing the jet temperature to promote precursor desorption, the substrate "cleaning" effect can be achieved locally under the area of the jet impingement such that the precursor is not depleted over the rest of the surface.

### 2.3 Conclusions

In summary, it has been shown that an inert gas impinging on a surface can be adjusted to significantly increase surface diffusion or to deplete precursor supply, depending on the reservoir temperature (impinging kinetic energy) of the gas jet. Plasma effects have been decoupled from jet impingement and it was experimentally demonstrated that the plasma is not substantially contributing to the enhanced surface mobility of an adsorbed precursor. Instead, the energy transfer in the course of gas jet impingement has the effect of raising the precursor temperature, which consistently describes all phenomena observed in experiments. Use of an inert gas jet for FEBID growth modulation is expected to be applicable to different modes of the precursor introduction to the substrate, albeit perhaps in a more complex fashion when both the precursor and an inert gas are co-jetted onto the surface. Since the jet has a local effect on the surface and allows for rapid changes in the precursor behavior, this technique will allow for new degrees of freedom for FEBID in nanomanufacturing. Additionally, a high-energy inert jet may be applied to locally clean the surface, which is of relevance to high-resolution SEM imaging.

# CHAPTER 3: HIGH PURITY TUNGSTEN NANOSTRUCTURES VIA FOCUSED ELECTRON BEAM INDUCED DEPOSITION WITH CARRIER GAS-ASSISTED SUPERSONIC JET DELIVERY OF ORGANOMETALLIC PRECURSORS

A substantially enhanced purity of tungsten nanostructures, with up to 95% of metal content relative to carbon contaminants with no post-processing, is achieved by using a supersonic inert carrier gas jet in the continuum flow regime to deliver the organometallic precursor for FEBID. Through impact-enhanced desorption of residual organic ligands at the deposition site, high kinetic energy of the gas jet assists in completing the secondary electron induced dissociation of precursor molecules, resulting in both increased metal purity as well as enhanced deposit growth rate. The inert gas jet at low Knudsen numbers also serves as a carrier gas to increase precursor flux to the substrate. Operating in the continuum flow regime reduces jet spreading and allows the use of smaller diameter nozzles to increase localization of precursor delivery to the deposition site. This drastic increase in localized precursor flux to the substrate is shown to compensate for the diminished sticking coefficient resulting from an increased impingement velocity of the continuum-flow gas jet relative to a molecular-flow gas jet. Increasing the jet temperature increases the delivered kinetic energy and allows tuning the balance between enhanced ligand contaminant desorption to increase deposit purity and the reduced sticking coefficient, resulting in the net increase of pure metal growth rate. Relevant physical mechanisms are discussed with support of experimental observations and multi-scale numerical simulations of the gas jet, comparing the conventional molecular gas-flow versus continuum gas-flow. Collectively, our results suggest a promising path forward for delivery of organometallic precursors in gas phase that results in high purity metal deposition without sacrificing the high growth rate.

### 3.1 Motivation

In FEBID of organometallic molecules, the precursor is typically introduced *via* a large diameter nozzle (~500$\mu m$) with molecular gas flow driven by the precursor's vapor pressure [13]. The ubiquitous problems with organometallic precursors are that they may not completely dissociate upon interactions with secondary electrons and that the ligands produced upon dissociation may become co-deposited as undesirable contaminants. Both effects reduce the metal content in the grown nanostructure with a negative impact on material properties. One such precursor, tungsten hexacarbonyl, is of interest for tungsten's conductive properties, corrosion resistance, and hardness; but its utility in FEBID has been limited by low purity of deposited nanostructures – typically tungsten purity as deposited is no greater than *ca.* 60% based on energy-dispersive X-ray (EDX) measurements [18][53][54]. A common method of improving the purity of FEBID nanostructures is post-deposition heating in an oxidizing environment to volatilize and remove carbon contaminants, which results in undesirable shrinkage, porosity due to gas phase formation and structural deformation [55]. Thus, it is desirable to purify the deposit as grown, and techniques to accomplish this goal include *in-situ* laser pulse heating [25] and direct substrate heating [56][57][58][59] which complete precursor dissociation and drive off contaminant by-products. Additionally, there are low temperature oxidation techniques of removing contaminants *via* pulsed laser treatment in presence of oxygen [19] or *in-situ* water vapor exposure under low vacuum environmental SEM (ESEM) conditions [20].

A new alternative and expedient method of *in-situ* removal of surface adsorbed contaminants is applying kinetic energy directly to the deposition zone *via* a heated or unheated inert gas jet at high impingement velocity. Advantages of using a supersonic gas

jet in the continuum flow regime as a carrier gas to supply precursor molecules include 1) tunable local surface heating *via* adjustable gas jet temperature [60] and 2) significantly greater precursor flux due to the carrier gas and the reduced spreading angle. This approach to FEBID of high purity tungsten nanostructures nearly 100% free of carbon contaminants is explored in this work, using a synergistic experimental and theoretical study of the fundamental physico-chemical mechanisms responsible for selective deposition of metal from the tungsten hexacarbonyl precursor.

The underlying principle of this technique is to use the continuum gas jet to enhance desorption of ligands produced in large amounts as a result of the secondary electron-assisted dissociation process. This yields a dual benefit of both reducing the likelihood of carbon-containing ligands being co-deposited with tungsten and mediating the rate-limiting step, which is adsorption of organic ligand byproducts that eventually saturate the deposition site and inhibit further decomposition of tungsten hexacarbonyl [61]. For reference, in conventional chemical vapor deposition of tungsten hexacarbonyl on nickel surfaces, the dissociation process at low to moderate temperatures is limited by surface site saturation with carbon monoxide ligands. The ligands can be fully desorbed with the surface heating to 130°*C*, but that temperature is also high enough to dissociate some ligands and introduce atomic carbon and oxygen contaminants [62]. Similarly, using electrons to dissociate tungsten hexacarbonyl first results in desorption of between 2 and 2.6 carbon monoxide ligands per precursor molecule; however, further electron interactions result in ligand dissociation which again introduces atomic carbon contamination [63]. If impingement *via* a high velocity gas jet can directly, *i.e.*, *via* momentum exchange upon impact between impinging and adsorbed molecules, promote

ligand desorption without ligand dissociation, then it may be possible for the dissociation processes of tungsten hexacarbonyl to proceed at a high rate and with minimal introduction of carbon-containing contaminants in the resulting pure metal deposits.

### 3.2 Experiment

Tungsten hexacarbonyl precursor is pre-loaded into a cartridge attached to the system according to Figure 3.1.a. The cartridge has a length of 8*cm*, an inner diameter of 0.32*cm*. It is heated in a hot water bath to 90°*C*, which is well below the decomposition temperature in argon (see Appendix B) [64], to increase the precursor's vapor pressure. A resistive heater is wrapped around the metal tubing that delivers the vaporized tungsten hexacarbonyl to the deposition chamber to prevent line condensation. As a reference baseline, the precursor is first injected into the SEM deposition chamber through a 455$\mu m$ inner diameter (ID) tube in the conventional molecular gas flow regime with resulting deposits used for comparison of both purity and growth rate. The outer diameter (OD) of the tube forces the orifice to be a significant distance from the substrate as indicated in Figure 3.1.b and discussed in the results. Experiments in the continuum flow regime are performed with a 75$\mu m$ ID capillary so an appropriate flow rate may be used without compromising chamber vacuum. The nominal chamber pressure is $1\times10^{-4}$ *torr* and the highest pressure reached is $4.2\times10^{-4}$ *torr* at an argon flow rate of $1.2\times10^{-7}$ *kg/s.* As an alternative, experiments could be performed with a modulated gas flow at high flow rates for short periods of time so that the larger nozzle could be used without overwhelming the vacuum pumps. Results from the two nozzles are generalized using the Knudsen number (defined as the ratio of molecular mean free path to the characteristic physical dimension as given by the inner diameter, ID, of injection nozzle) over each nozzle's range of

operation. For consistency of comparison, the Knudsen numbers are calculated using gas densities based on a given mass flow rate and conditions for the choked flow at the nozzle exit, even though the molecular and transitional flow regimes do not have sonic exit velocities.

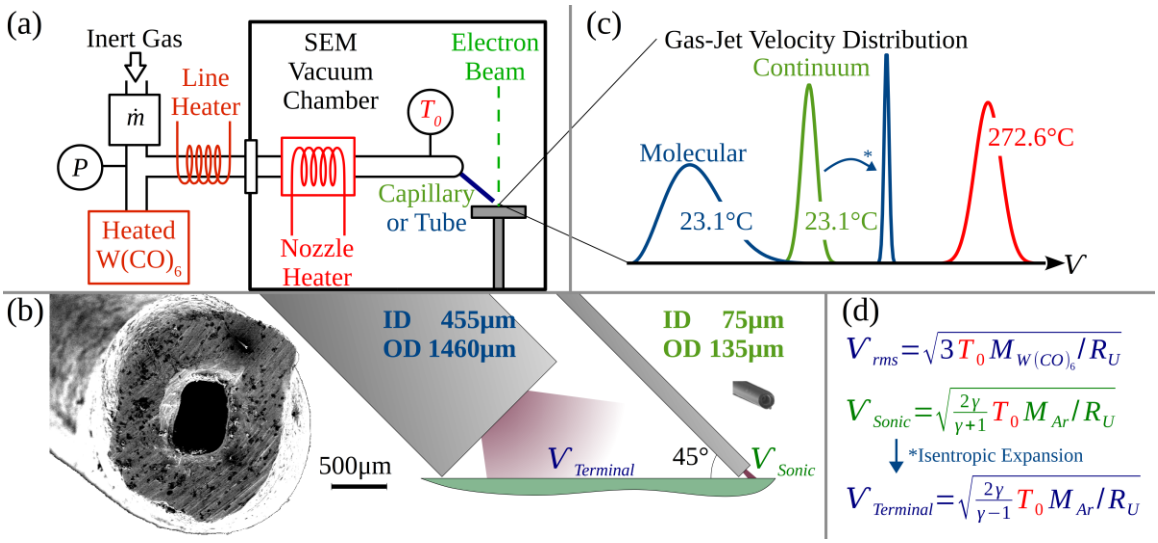


***Figure 3.1: (a) Diagram of the experimental setup (b) Relative geometries of the 455µm ID / 1460µm OD tube and the 75µm ID / 135µm OD capillary (c) Schematic of the velocity distributions at the orifice (d) Characteristic velocities of the gas jets***

The impingement velocity in the molecular gas flow regime follows the Maxwell-Boltzmann distribution, as indicated in Figure 3.1.c [65]. Its root-mean-square (rms) velocity (Figure 3.1.d) is 145 *m/s* when the temperature at the inlet to the nozzle ($T_0$) is 24°*C*, the molar mass of tungsten hexacarbonyl ($M_{W(CO)6}$) is 351.9 *kg/kmol*, and the universal gas constant ($R_U$) is 8314 *J/kmol·K*. The vapor pressure of the precursor is not sufficient to reach the transitional or continuum flow regimes because the pressure gradient required to achieve the higher flow rates would require heating the precursor beyond the point of auto-dissociation. Therefore, argon is introduced through a mass flow controller as an inert carrier gas to sweep along the tungsten hexacarbonyl and carry to the deposition

chamber with an increased impingement energy. In the continuum flow regime, the gas accelerates in the nozzle and its temperature drops according to Fanno flow [66], resulting in sonic velocity at the exit with a Gaussian velocity distribution (Figure 3.1.c). Assuming $W(CO)_6$ is dilute in argon gas, the sonic velocity (Figure 3.1.d) is 278$m/s$ using $T_0$ = 24°$C$, the isentropic expansion coefficient of argon ($\gamma$) 1.4, and the molar mass of argon ($M_{Ar}$) 39.9$kg/kmol$. If the continuum gas were free to then expand isentropically into the vacuum, it would approach its terminal velocity as its temperature asymptotically approached zero [67]. Since the terminal velocity for all monotonic gases is twice their sonic velocity, the average substrate impingement velocity of a continuum gas jet is a supersonic velocity between these two limits. Because of the temperature reduction upon expansion, the velocity variance, which corresponds to the gas temperature prior to impingement on the substrate, is smaller than that of the molecular flow regime. The impingement energy can be further increased by increasing the nozzle inlet temperature with the locally integrated miniature resistive heater (Figure 3.1.a). Transitional flow impingement velocity distributions are expected to be between those of molecular and continuum distributions in terms of both average velocity and span of distribution.

Both dielectric and metallic substrates were used in deposition experiments. The dielectric substrate was a silicon wafer with a thermally grown 300$nm$ thick oxide layer, which was cleaned by soaking in isopropyl alcohol and rinsed with deionized water before use. The metallic substrate was made by sputtering a 750±50$nm$ thick layer of gold-palladium alloy onto a silicon oxide substrate. All deposits were grown in spot mode using a 10$kV$ focused electron beam at a working distance of 16$mm$, a current of 0.5$nA$, and an approximate beam diameter of 400$nm$ to produce sufficiently large nanostructures for EDX

analysis. Deposition time was recorded to compare relative growth rates between deposits. Because oxygen is present in the silicon oxide substrate and the expected contaminants from deposition using tungsten hexacarbonyl are oxygen and carbon, all EDX results for the silicon oxide substrate are reported as the atomic percent of tungsten versus carbon only. As a complimentary assessment of deposit purity supporting the conclusions of EDX analysis, topological analysis using atomic force microscopy (AFM) imaging of deposits was performed before and after heating in an oxygen environment. AFM topography images were obtained using a Dimension-3000 microscope with a silicon tip in a tapping mode. The heating oxidizes and volatilizes the carbonaceous species in the nanostructures. Thus, the percentage reduction of each deposit's volume upon carbon burnout is indicative of non-tungsten content and is important for independent substantiation of the EDX analysis, which has intrinsic deficiencies in quantitative analysis and is best reliable for qualitative composition change assessment only.

### 3.3 Results

Figure 3.2 shows that decreasing the Knudsen number toward the continuum flow regime improves the as-deposited purity of the tungsten pillars as measured by reduction of the atomic carbon content. This result demonstrates an important benefit of increasing the impingement energy to assist with complete precursor dissociation due to impact-enhanced desorption of CO ligands with increased purity of the resulting tungsten deposits. Tungsten deposits on the silicon oxide substrate (Figure 3.2.a) have an average (baseline) purity, defined as the fraction of atomic tungsten relative to carbon, of 26%. The precursor delivery *via* 455$\mu m$ ID nozzle yielded no increase in purity across the higher range of Knudsen numbers (molecular and transitional flow). For the 75$\mu m$ ID nozzle, a transition

to enhanced purity occurs at the Knudsen number of 0.015, and the maximum purity of 95% is achieved deeply in the continuous (Kn<<0.1) flow regime. The figure includes data from two sets of experiments with different nozzles with the same 75$\mu m$ ID (the second nozzle designated in Figure 3.2.a as 75$\mu m$*) is slightly different in length from the original nozzle denoted as 75$\mu m$, which was used in the first set of experiments on the silicon oxide substrate and all experiments with the gold-palladium substrate throughout the rest of the paper. The results of Figure 3.2.a must be qualified by the fact that the first characteristic x-ray for tungsten, 1.774$keV$, is difficult to distinguish from the characteristic x-ray for silicon, 1.739$keV$. The gold-palladium substrate was prepared to ensure that silicon in the substrate would not bias the tungsten measurement. The EDX measurement of the bare Au-Pd substrate indicated negligible (<3%) silicon content.

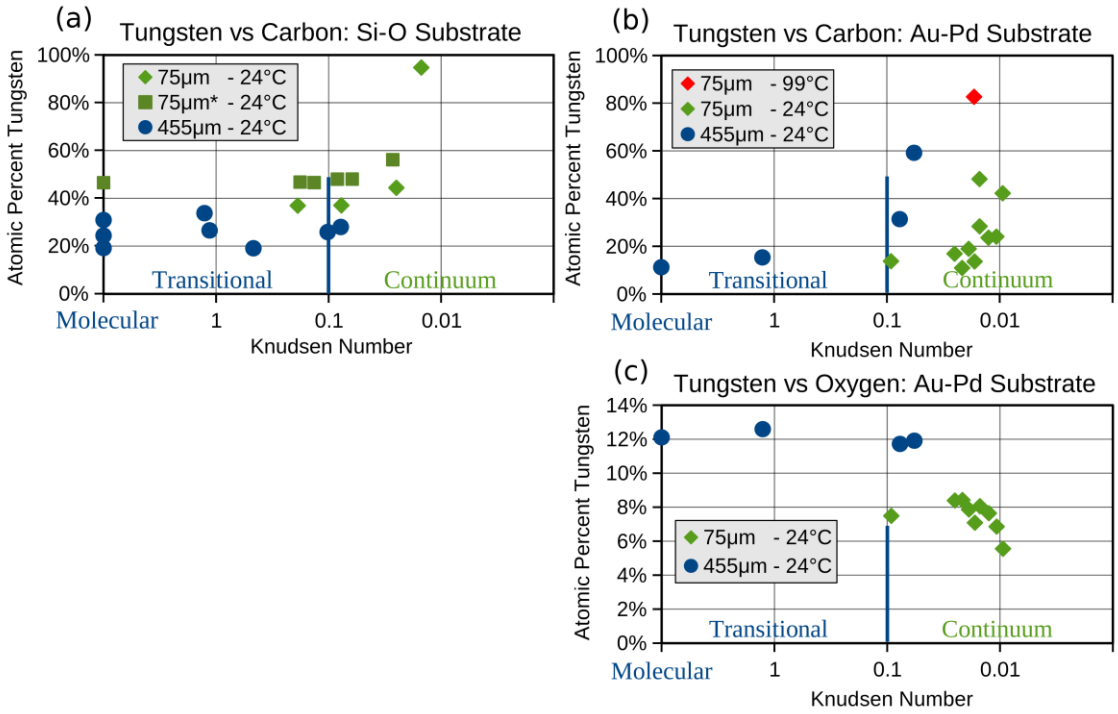


***Figure 3.2: EDX measurements of deposit composition as a function of the flow regime, nozzle size, and deposition substrates. Atomic percentages in terms of (a, b) tungsten***

***relative to the total amount of tungsten and carbon (c) tungsten relative to the total amount of tungsten and oxygen***

Tungsten deposits on the gold-palladium substrate (Figure 3.2.b) with the 455$\mu m$ ID nozzle exhibit an earlier transition to enhanced purity at the Knudsen number 0.077, which is appreciably higher than the transitional Kn=0.015 for the 75$\mu m$ ID nozzle (this was not observed in Figure 3.2.a because flow from the 455$\mu m$ diameter capillary does not span the same range of Knudsen numbers). The difference in the transitional *Kn* numbers between the large and small ID nozzles is due to the distance from the nozzle orifice to the substrate as indicated in Figure 3.1.a. Geometrically, the large ID nozzle allows a greater time-of-flight for the jet to reach the substrate; therefore, the gas jet from the larger nozzle with the same choked flow exit velocity of 278 *m/s* isentropically expands to a greater velocity. To further assess the effect of impingement energy on deposit purity, two subsequent deposits were made with the 75$\mu m$ ID nozzle at the same flow rate of $7.4\times10^{-8}$ *kg/s* and inlet temperatures $T_0$ of 24°*C* and 99°*C*. The sonic velocities increased from 278 *m/s* to 311*m/s*, and the tungsten purities increased from 48% to 83%, respectively. Further increase of $T_0$ resulted in an inability to grow deposits due to complete reduction in the sticking coefficient.

Three effects are considered to account for greater deposit purity at increased impingement velocities. One possibility is that the gas jet heats the surface to complete the precursor dissociation and to drive off ligands via thermally-enhanced desorption. It is known that the gas jet delivers kinetic energy to the substrate to stimulate enhanced surface diffusion [60]; however, direct measurement of the substrate temperature using microfabricated resistance thermometry (see Appendix B) reveals only 0.5°*C* increase in

temperature upon interaction with an unheated gas jet and 1.7°$C$ when the gas temperature at the nozzle inlet is $T_0$ is 205°$C$. The second possibility is the impact induced precursor dissociation. However, because no deposit could be grown in the absence of the electron beam, the precursor impingement velocity must not have been sufficient to dissociate the impinging molecules. The remaining and most plausible pathway is that carrier gas molecules deliver sufficient kinetic energy to remove weakly-bound physisorbed ligands from the surface before they become part of the deposit, leading to observed enhanced purity of deposits.

Comparing carbon and oxygen content in deposits produced by conventional molecular flow delivery of tungsten hexacarbonyl precursor (Figures 3.2.c and b at high Kn>0.1) shows uniform and comparable ratio (10%) of oxygen to tungsten and carbon to tungsten in deposits. This one-to-one relationship between oxygen and carbon suggests co-deposition of carbon monoxide ligands is the primary source of contamination responsible for low tungsten purity of FEBID deposits. Based on our suggested mechanism for increased purity, carbon can only be removed in the form of carbon monoxide, which should lead to the proportional decrease of the oxygen and carbon contents in the deposits. However, at lower Knudsen numbers, while the carbon content does decrease as expected, the oxygen content is actually increasing. This unexpected trend in increased oxygen to tungsten ratio is not an outcome of the deposition process but an artifact of extended exposure to oxygen rich atmosphere outside of the SEM chamber vacuum environment, leading to deposit oxidation prior to EDX measurements. It should be noted that tungsten oxidation is not typically observed in FEBID nanostructures, but it is owing to the fact that such deposits are low purity with tungsten embedded into carbonaceous matrix, which

protects it from oxidation upon exposure to ambient environment. In fact, pure tungsten is a highly oxidizing material forming various stable forms of tungsten oxide even at room temperature, especially in a high humidity environment [68]. The process is further accelerated in nanostructures due to their large specific (per unit volume) exposed surface area. It should be noted that tungsten oxidation is not typically observed in FEBID nanostructures, but it is owing to the fact that such deposits are low purity with tungsten embedded into carbonaceous matrix, which protects it from oxidation upon exposure to ambient environment. Collectively, these observations suggest that only carbon content should be used as a true proxy of deposit purity, as given by Figure 3.2.a and b, especially in the case of metals with propensity to oxidation.

To confirm the EDX results, deposits made at different Knudseni) numbers on the gold-palladium substrate were heated to $450°C$ in an oxygen environment to volatilize and remove carbon content. The deposits made with the $455\mu m$ ID nozzle were heated for $20min$, and those made with the $75\mu m$ ID nozzle were heated for $15min$. There are three possible changes the deposits can undergo as carbon is volatilized and leaves the structure as CO or $CO_2$ gas: (1) the remaining tungsten structure may shrink to fill in the gaps left by vacated carbon matrix; (2) it may become porous but maintain the same topological structure made of a tungsten agglomeration; (3) or, in parallel to the steps 1 and 2, it may oxidize tungsten forming lower density oxide structures of $WO_3$ (density of $7{,}160 kg/m^3$) or $WO_2$ (density of $10{,}800 kg/m^3$). Since the density of pure tungsten ($19{,}250 kg/m^3$) is much higher than that of tungsten oxides, oxidation cannot reduce the volume of a deposit. Therefore, reduction in volume of a deposit after heating is strong evidence for a loss of carbon contaminants resulting from the deposition process. AFM measurements of the

deposits before and after heating are used to calculate the volume changes (see Appendix B). Loss of volume is greatest at 86% for a primarily carbon structure deposited without tungsten using surface contamination for reference in Figure 3.3. Material loss of deposits made from tungsten hexacarbonyl without use of a carrier gas is similar at 74%. For both nozzle sizes, deposits made at an increased flow rate into the continuum flow regime have shown a rapid decrease in volume loss by carbon volatilization. This result unambiguously indicates that as-deposited tungsten purity can significantly be increased by increasing the impingement energy of the precursor gas, with the suggested primary mechanism of enhanced gas jet impact-induced desorption of the contaminant ligands.

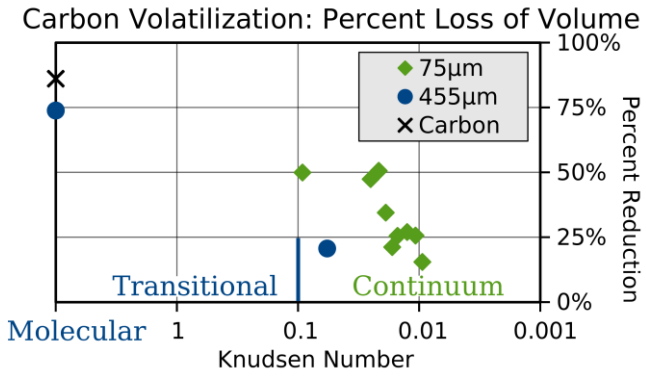


***Figure 3.3: Percent loss of volume of deposits on the gold-palladium substrate as measured by AFM before and after heating to 450°C in an oxygen environment.***

There is a trade-off, however, that greater impingement velocities result in a diminished sticking coefficient of the precursor to the substrate [28]. Higher impingement velocities were attempted with both substrates to reach higher deposit purities. While a nozzle inlet temperature of ~99°*C* and sonic velocity of 311 *m/s* yielded the desired effect of enhanced purity (83% of tungsten vs carbon) of the metal deposit, further increase to ~184°*C* (345 *m/s* sonic velocity of choked flow at the nozzle exit) resulted in an inability

to grow deposits due to the vanishing sticking coefficient between the precursor molecule and the substrate. Likewise, higher impingement velocities were tested on a $SiO_2$/Si substrate with the 75$\mu m$ ID nozzle and the elevated nozzle inlet temperature of ~272°*C*. In Figure 3.4.b the sonic choked flow velocity is 280 *m/s* and in Figure 3.4.c it is increased to 377 *m/s*, clearly demonstrating that too high of an impingement velocity precludes any deposition due to the substantial reduction of the sticking coefficient.

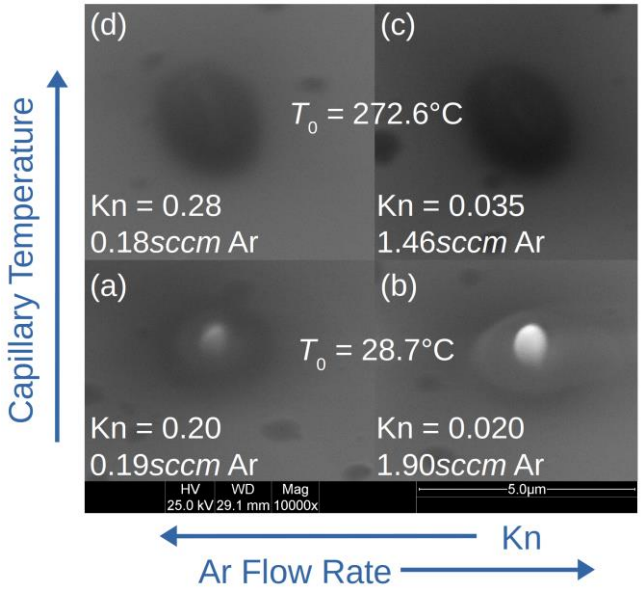


***Figure 3.4: Deposition morphology due to inlet temperature and flow rate. Left-to-right) Constant temperature increase flow rate. Bottom-to-top) constant flow rate increase temperature.***

When the sticking coefficient is not zero, its reduction can be compensated for by the increased precursor flux to the substrate. Comparison between Figures 3.4.a and b illuminates this effect, showing that the growth rate in the continuum flow regime is greater than in the transitional flow regime even though the sticking coefficient is diminished. In the case of gas injection in the molecular flow regime, the tungsten hexacarbonyl precursor flow rate is only $1.5\times10^{-12}$ *kg/s* as given by $(dm/dt)_{W(CO)6} = M_{W(CO)6}P_{vapor}(T_P)$ ·

$\left(2\pi M_{W(CO)6} R_U T_P\right)^{-1/2} \cdot (\mathrm{ID}^3/L)$ where $R_U$ is the universal gas constant, the nozzle ID is 455μm, $L$ is the tube length of about 30$cm$ [69], $T_P$ is the precursor temperature at the reservoir, and the vapor pressure of tungsten hexacarbonyl at 90°$C$ is 1$kPa$ [70]. When argon is then introduced as a carrier gas to operate in the continuum flow regime, the precursor flow rate in the gas jet increases by four orders of magnitude to $2\times10^{-8}$ $kg/s$. This is given by $V_{rms}$=$P_{vapor}(T)\cdot M_{W(CO)6} P_{vapor}(T)\cdot(dm/dt)_{Ar}$, where $P$ is the measured line pressure that, being linearly related to the argon mass flow rate $(dm/dt)_{Ar}$, has no influence on the precursor flow rate for a given nozzle configuration. If the nozzle had a different geometry, then its flow resistance would differ and alter the relationship between the pressure and flow rate. Therefore trends in results cannot be directly compared between different nozzles. In the configuration used, a line pressure of 26$kPa$ corresponded to an argon flow rate of $6\times10^{-8}$ $kg/s$. To the same effect, further increase of the Argon carrier gas flow rate in the continuum regime reduces the spreading angle of gas jet, thereby focusing the precursor flux to the deposition region.

The transition to increased flux focusing is illustrated by simulations performed using the DSMC [71]. This algorithm is well established to simulate the molecular flow of precursor molecules impinging onto the substrate in conventional gas injection systems, which has a significant impact on growth dynamics [30][72][73]. In order to simulate the continuum gas jet in a domain that also includes transitional and molecular flow regimes, the DSMC algorithm has been extended to allow for dynamic adaptation of the simulation according to the local particle density (Chapter 4). A cross-sectional view of the deposition conditions and the deposition location relative to the nozzle are given in Figure 3.5.a. The substrate fluxes of argon at the substrate surface (*i.e.*, deposition site) are compared in

Figure 3.5.b for both molecular and continuum flow regimes for the 75$\mu m$ ID nozzles. The results, normalized by the total flux, indicate that the transition into the continuum flow regime significantly increases the maximum flux achieved. This flux focusing effect *via* micro-jet continuum flow has been experimentally validated by profiling the gas-assisted etching rates in a confined zone surrounding the projected trajectory of gas impingement from the nozzle [74]. Although the optimal point for maximum precursor flux is not accessible due to beam "shading" by the nozzle, the deposition location is kept at a constant location relative to the nozzle, resulting in variation of precursor flux and impingement energy depending only on each flow condition and not on a spatial location for a given experiment. Further, the simulations indicate that the spatial variations of flux and orthogonal velocity near the deposition point are relatively small. This conclusion and the consistency of deposition conditions within a 20$\mu m$ radius of the deposition point has been experimentally verified as described in Appendix B.

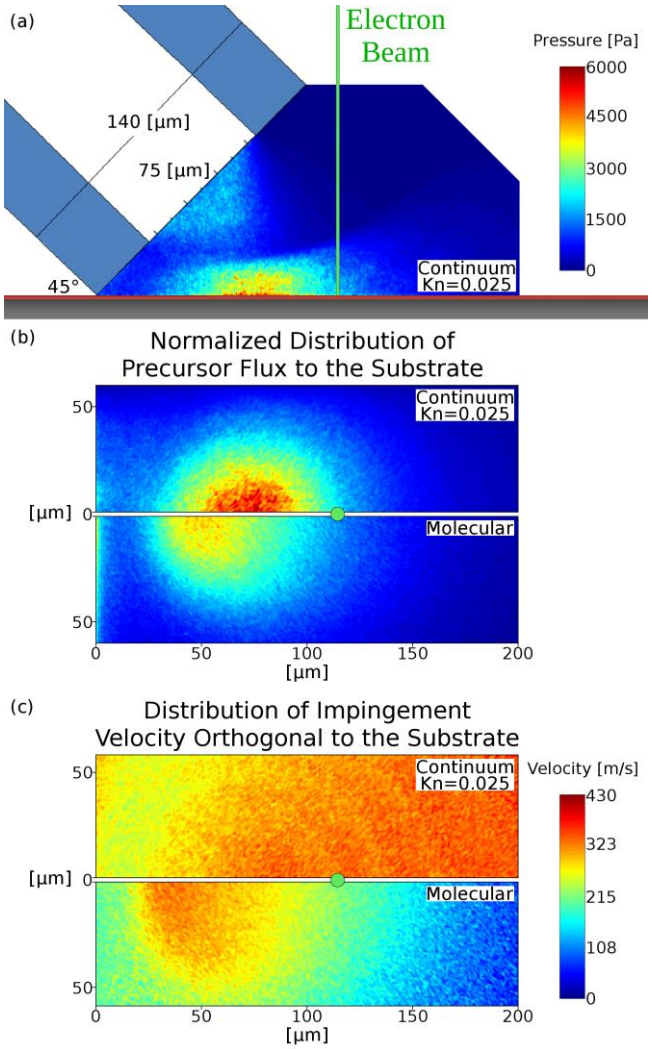


***Figure 3.5: Adaptive DSMC simulation of limiting (continuum or molecular) flow regimes at 24°C (a) Centerline cross-section (b) Comparison of normalized precursor (c) Comparison of the orthogonal impingement velocity to the substrate.***

There are three competing phenomena associated with carrier gas induced continuum gas jet precursor delivery that determine the net (*i.e.*, pure metal) deposition rate: (1) precursor flux enhancement, (2) sticking coefficient reduction, and (3) a decrease of carbon-containing parasitic by-products resulting from precursor dissociation. Total (*i.e.*, including contaminant) deposit volumes calculated from the AFM measurements were used to estimate deposition rates in Figure 3.6 for different conditions on the gold-

palladium substrate (see Appendix B). The highest deposition growth rate is observed with the large nozzle with no carrier gas, which is notably the least pure deposit. It is deposition of carbon impurities that artificially inflate the deposition rate of this data point. Introducing the carrier gas and transitioning to the continuum gas jet injection regime results in a lower overall deposition rate, but much higher purity (tungsten content) of the deposits and thus an increased net growth rate of pure metal. The growth rates from the 455$\mu m$ ID nozzle cannot be directly compared to those of the 75$\mu m$ ID nozzle, which ostensibly appear lower, because the low flow restriction of the larger precursor delivery tube allows a lower ratio of line pressure to carrier gas mass flow rate, which results in a significantly higher precursor mass flow rate in the continuum regime. However, taken on their own, the volumetric deposition rates from the 75$\mu m$ ID nozzle monotonically increase as the Knudsen number decreases and the supersonic jet exiting the nozzle moves deeper into the fully continuous flow regime. This indicates that an increased precursor flux more than compensates for the effects of a diminishing sticking coefficient and increasing deposit purity due to desorption of undesired co-deposited impurities.

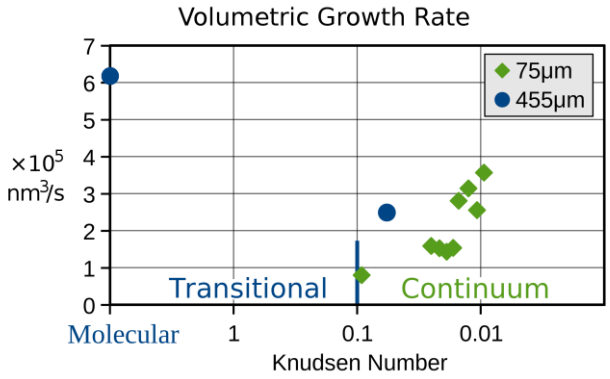


***Figure 3.6: Total deposit volumes on the gold-palladium substrate were measured by AFM***

### 3.4 Conclusions

A new process has been demonstrated for using the supersonic expansion of the carrier gas to increase the flux and impingement energy of precursor molecules, resulting in substantial improvement of electron beam induced metal deposit purity and growth rate. Deposition experiments aimed at mechanism elucidation and characterization with EDX and AFM substantiated the impurity content *via* independent chemical composition and deposit topography measurements. Use of a carrier gas to deliver organometallic precursor molecules in a continuum-flow supersonic gas jet offers the advantages of increased deposition rate due to locally increased precursor flux and increased deposition purity due to carrier gas impact-induced desorption of ligand contaminants. This technique should be applicable to any organometallic precursor for which the source of impurity is incompletely dissociated ligands, which are weakly bound to the surface and can removed upon impact of the sufficiently high kinetic energy inert gas jet. Further increase of the impingement energy, achieved by heating the gas jet at the nozzle or by increasing the distance between the nozzle orifice and the substrate, allows the gas jet to expand toward its much higher terminal velocity resulting in further improvement in deposit purity. The adverse effect of the increased impingement velocity is the reduction of the sticking coefficient. However, because it is the impingement energy, not specifically the velocity, that assists in enhanced desorption of contaminating ligands, a carrier gas with a greater molecular mass can preserve all the advantages of operating in the continuum gas jet regime, while simultaneously delivering a reduced impingement velocity and thus higher sticking coefficient. Additionally, because it is the line pressure at the point of entrainment of precursor molecules at a specific continuum flow regime that limits the precursor mass

flow rate, precursor supply can be further increased (*i.e.*, having a greater fraction of precursor molecules in the carrier gas) by minimizing hydrodynamic resistance to the flow through the nozzle.

The supporting information describes the method of calculating deposit volumes from AFM measurements before and after thermal annealing, discusses how these calculations account for changes in substrate thickness due to thermal ablation, and provides tilted SEM images of deposits before and after heating. Data for three deposits grown at slightly different positions relative to the nozzle are presented to support the claim that minor errors in beam location do not significantly affect results. Results from thermal measurement at the jet impingement zone are included to support the assertion that the gas jet does not appreciably heat the surface. The decomposition rate and temperature of tungsten hexacarbonyl is given. A brief explanation of the adaptive algorithm that was developed as a DSMC extension for multi-regime simulations is included in the supporting information.

# CHAPTER 4: ADAPTIVE DIRECT SIMULATION MONTE CARLO ALGORITHM FOR UNIFIED CONTINUOUS THROUGH MOLECULAR FLOW REGIME SIMULATIONS WITH IMPROVED COMPUTATIONAL EFFICIENCY

A new approach has been developed for an adaptable DSMC algorithm for gas flows spanning the range of Knudsen numbers from O(0.01) (continuum flow) to O(10) (molecular flow) using a single domain and a unified computational physics for the entire simulation. This technique is based on introducing a dynamically adjusting local weighting factor, which represents the ratio of physical particles (molecules) to simulation particles, to always maintain sufficient particles per cell for simulation accuracy, yet keeping the number of simulation particles to a minimum for computational efficiency. In this chapter, the fundamental principles of the adaptive algorithm are describe, its viability as a DSMC technique is demonstrated, computational improvements for the verification cases are discussed, and one of the algorithm's important applications for nanoscale materials processing is illustrated.

## 4.1 Motivation

The DSMC technique is predicated on the idea that a relatively small number of simulation particles can capture the physical behavior of an unmanageably large number of real particles. In order to accomplish this, all of the physical interactions that take place among individual particles are adapted to apply to simulation particles that represent a large number of real particles. The technique has been demonstrated to produce accurate results for molecular, transitional, or continuum flow regimes [71]; however, it is typically applied to the problems involving only one of these flow regimes and requires special treatment and increased computational overhead under conditions in which all three flow regimes are

realized within the same computational domain. The presence of multiple regimes implies significant variation of particle density from one location to another since the weighting factor, $F$, representing the ratio of the real molecules to the simulation particles is commonly set to a fixed value for all cells in the simulation domain. This necessarily results in too few particles per a cell in the molecular flow regime for accurate results or too many particles per another cell in the continuous flow regime for computational efficiency.

Several techniques have been applied to circumvent this problem. The simplest approach is to accept the computational inefficiency and provide the necessary computer memory and time to run a simulation with an excessive number of particles. Computational time may be reduced for this method by applying different time-steps to domains of significantly different densities in order to reduce the computational resources committed to the low-density regions [75]. This technique has further been adapted to allow each cell to have its own optimal time-step [76]. Another alternative is to custom tailor the cell dimensions to increase in regions where particle densities decrease; this has been done, for example, to simulate flow through an expanding nozzle [77]. More recently it has become common to automate cell transitions between a Navier Stokes solver and DSMC [78][79][80][81][82]. The latter approach is particularly effective when the majority of the domain is in the continuum flow regime and the minority of the domain requires the DSMC approach. However, it does not address the significant variation in particle density that may occur within the regions of transitional and molecular flow regimes.

One such problem is that of a continuum gas micro-jet emanating into a vacuum and impinging upon a substrate. This problem is motivated by beneficial deposition effects

(growth rate and composition) obtained by continuum gas micro-jets in FEBIP [60][83]. The complex gas flow structure requires continuum through molecular flow regimes in a full three-dimensional simulation. To obtain full simulation results for this application, we introduce an adaptive DSMC algorithm, which adjusts cell weighting factors according to cell populations. This allows DSMC simulations to seamlessly transition from the continuum flow regime at the nozzle to transitional and molecular flow regimes where the transition boundaries are not known a-priori or are not readily defined. This approach aims to maintain appropriate simulation particle populations in each cell for both simulation accuracy and computational efficiency. Further, this simulation method can apply the same uniform computational representation of flow physics throughout the domain.

### 4.2 Direct Simulation Monte Carlo

The velocity distribution of the real particles in the isolated gas of Figure 4.1.a can be matched by a relatively small number of representative particles (Figure 4.1.b). The temperature and field velocity may be calculated from the velocity variance and average of the representative particles just as well as from the real particles, greatly reducing the information needed to perform a simulation. The number of real particles represented by a simulation particle is denoted by the weighting factor $F$.

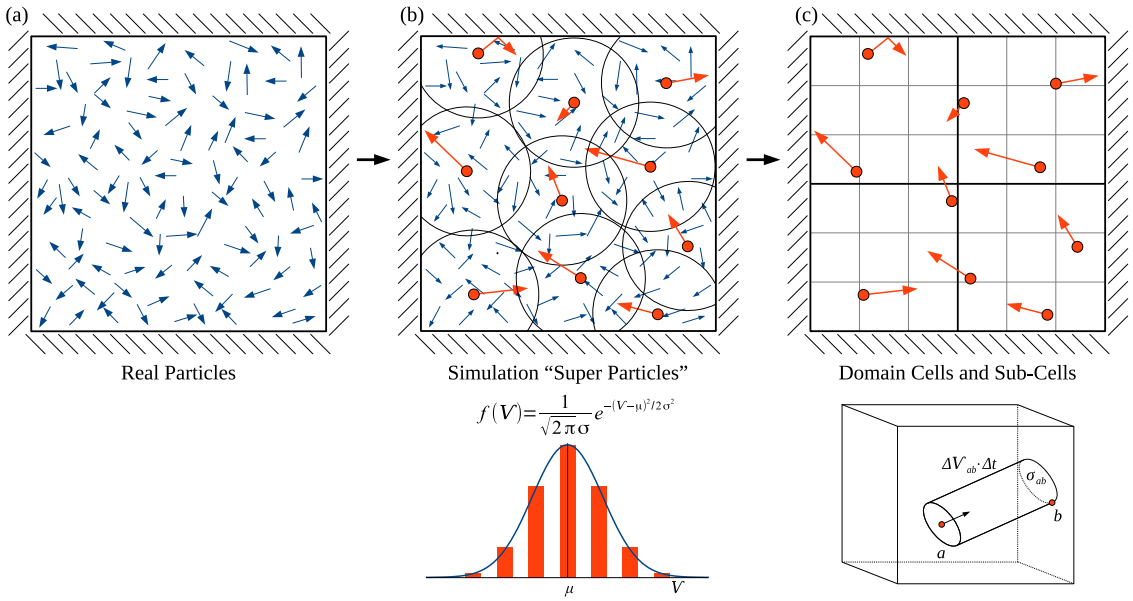


***Figure 4.1: Overview of DSMC physics a) Sample domain of real particles b) Real particles represented by simulation particles that capture velocity distribution c) Collisional cells simplify collision calculations.***

The second approximation of DSMC is the manner in which simulation particle collisions are implemented. Rather than calculating the position and time of particle intercepts, adjacent particles are made to collide with each other based on a locally calculated probability of collision. The domain is divided into cells and sub-cells, as indicated in Figure 4.1.c, and representative particles are only considered to collide with each other if they are both within the same sub-cell. Based on the experience of previous DSMC developers, *F* should selected such that approximately 20 representative particles are in each a sub-cell (not as represented in Figure 4.1.c) [84][85], and the sub-cell dimensions must not exceed one third of the local mean free path [71][85][86]. The simplest collision model is that of the Hard-Sphere, which will be described by first considering real particles. In a given time step, $\Delta t$, two real particles in a sub-cell sweep out a collisional volume of $\sigma_{ab} \cdot (\Delta V_{ab} \Delta t)$ where $\sigma_{ab}$ is the cross-sectional area using the

average of the two diameters, and $\Delta V_{ab}$ is the relative velocity of particle $a$ to particle $b$. The time step should be chosen such that between time steps no particle may travel further than the nearest neighbor cell and no collisional volume is greater than the sub-cell volume. The collisional probability between these two real particles in a given time-step is then the collisional volume divided by the cell volume. The total number of real collisions is the sum of collisional probabilities between every pair of particles in the cell. Using $N_R$ to represent the number of real particles in the cell, the total number of combinations is $(N_R^2 - N_R)/2$. (This can be visualized by taking a matrix of $N_R$ rows and $N_R$ columns. The number of combinations is $N_R^2$. A particle cannot collide with itself, so the diagonal is removed. And the upper-right triangle is a duplicate of the lower-left triangle, so the result is divided by two.) The total number of real collisions is then given by Equation 4.1. The number of simulation particles is $N_S = N_R/F$, the number of simulation collisions is $1/F$ times the number of real collisions, and $N_R^2 \gg N_R$, so the number of simulation collisions per sub-cell is given by Equation 4.2. The collision is then evaluated relative to the center of mass velocity with one particle randomly assigned a rebound zenith angle between 0 and π (where 0 is total rebound and π indicates no trajectory changes) and an azimuth angle between 0 and 2π. The other particle is assigned the resultant velocity that conserves energy and momentum.

$$\text{Real Collisions} = \frac{[(N_R^2 - N_R)/2]\langle \sigma_{ab} \Delta \mathrm{V}_{ab} \rangle \Delta t}{\forall_{\text{sub-cell}}} \tag{4.1}$$

$$\text{Simulation Collisions} \approx \frac{N_S^2 F \langle \sigma_{ab} \Delta \mathrm{V}_{ab} \rangle \Delta t}{2 \forall_{\text{sub-cell}}} \tag{4.2}$$

The Hard-Sphere model does not, however, accurately represent real particle interactions. The surface of an atom, for example, is the result of its electron cloud exerting a repulsive force on other particles that are close enough to appreciably interact with it. As such, they are effectively soft spheres. When particles pass by each other at significant velocities, there is less time for the repulsive force to affect particle trajectories. Therefore, the Variable Hard Sphere [87][88] and the Generalized Hard Sphere [89] models were developed to adjust particle cross-sections based on relative velocity. Further, the non-rigid nature of a particle's surface causes the rebound angles to not be uniformly distributed as described; therefore, the Variable Soft Sphere [71][90] and the Generalized Soft Sphere [89] models use weighting factors in selecting rebound angles. The capability and limitations of the Hard-Sphere model are further addressed in Appendix C.

In summary, the main DSMC cycle is composed of three steps 1) Collisions: particle trajectories are adjusted based on probabilistic local sub-cell collisions, where the likelihood of a collision is based solely on collisional volume and not proximity. Since the representative particles are representative of particles throughout the cell, a single cell is effectively a single point, and the proximity nature of collisions is satisfied by the constraint of interacting only with other particles in the same sub-cell. 2) Motion: particles are moved on their trajectories for a single time step in which they may cross into new sub-cells or interact with a boundary. 3) Indexing: when particles move to a new sub-cell, their computational addresses must be updated. It is common to separate this from the motion module to facilitate parallel computing. To initiate an isolated simulation, as in the example given in Figure 4.1, it is necessary to specify the initial temperature, pressure, and velocity of each cell. The number of particles to place in each sub-cell is $N_S = \forall_{\text{sub-cell}} P/(Fk_B T)$,

where $P$ is the specified pressure, and $T$ is the specified temperature. Each axis of the particle's velocity is selected by a random number from the Gaussian distribution $f(\mathrm{V}) = exp\,[-(\mathrm{V}-\mu)^2/2\,\sigma^2]/\sqrt{2\pi}\,\sigma$, where $\mu$ is the specified mean velocity, $\sigma = R_U\,T/M_m$, $R_U$ is the universal gas constant, and $M_m$ is the molar mass.

If one of the boundary surfaces has an imposed gas flow across it, a permeable surface, then there is implicitly a fourth step to the cycle of adding boundary flux particles. Calculating the velocity distribution and the number of particles to add at such a boundary is non-trivial and is included here for a lack of the clear derivation in existing literature. In considering the inlet flux across a boundary surface, the average velocity of particles moving in the "positive" direction is given by Equation 4.3, for which $\Phi(x) = 1 + erf\left[x/\sqrt{2}\right]/2$, and $\mu$ is not necessary positive. The density of particles entering the domain is given by Equation 4.4 as the local particle density, $n$, times the fraction of particles moving in the "positive" direction. The inlet flux across the surface is the product of the average velocity and density of the inlet particles. This leads directly to Equation 4.5 for the number of particles to add to the surface of a boundary sub-cell at each time step. Of the particles moving in the "positive" direction, the probability of a particle crossing the surface is proportional to its velocity. Therefore, the velocity distribution is $g(\mathrm{V}) = \mathrm{V}f\,(\mathrm{V})/c$, in which $c$ is the normalizing parameter $c = \mu \cdot [1 - \Phi(-\mu/\sigma)] + \sigma \cdot exp\,(-\mu^2/2\,\sigma^2)/\sqrt{2\pi}$. In this manner, the number of particles introduced at a permeable surface, and the orthogonal projection velocity distribution, are fully defined by the imposed pressure, temperature, and mean velocity at the boundary. The velocities for the two axes tangent to the surface are given by the baseline distribution $f(V)$.

$$\langle \mathrm{V}_P \rangle = \frac{\int_0^\infty \mathrm{V}\, f(\mathrm{V}) d\mathrm{V}}{\int_0^\infty f\,(\mathrm{V}) d\mathrm{V}} = \frac{\sigma\, e^{-\mu^2}/2\,\sigma^2}{\Phi(\mu/\sigma)\sqrt{2\pi}} + \mu \tag{4.3}$$

$$n_P = n \cdot \int_0^\infty f\,(\mathrm{V}) d\mathrm{V} = \frac{P}{k_B T} \cdot \Phi\left(\frac{\mu}{\sigma}\right) \tag{4.4}$$

$$N_{boundary} = \frac{A_{\text{sub-cell}} \Delta t}{F} \frac{P}{k_B T} \left[ \frac{\sigma\, e^{-\mu^2}/2\,\sigma^2}{\sqrt{2\pi}} + \mu \cdot \Phi\left(\frac{\mu}{\sigma}\right) \right] \tag{4.5}$$

The remaining boundary conditions are less complex. When a gas is in equilibrium across a free surface with a mean velocity of zero, the velocity distribution orthogonal to the boundary is $g(V)$, and the two tangential velocity distributions are still $f(V)$. The same constraints are applied for a particle rebounding from a diffuse non-adiabatic surface (see Supporting Information). For a diffuse adiabatic surface, the original velocity is preserved and the direction is selected based on equal probability for motion over a hemisphere above the surface. For a surface of symmetry, particles are specularly reflected back from the surface.

The results of the simulation are obtained by sampling the number of particles, the average velocity, and the velocity variance in the cells and sub-cells. According to the velocity distribution $f(V)$, the temperature of a particle species is related to the velocity variance along a single axis according to Equation 4.6, where $m$ is the mass of an individual real particle, and $N$ is the number of simulation particles that have been sampled. Pressure is determined from the number of particles, the temperature, and the volume. When

multiple species are involved, the cell pressure is the sum of the partial pressures of each species, and the temperature and velocity are the averages of each species weighted by the relative population number density. Because there are typically 20 particles in each sub-cell, there are insufficient particles in a given time step for statistical calculations. If the simulation of interest is a steady-state simulation, then the same sub-cell of a converged simulation may be sampled over several time-steps to acquire an adequate sampling. To extract results from a transient simulation, it is necessary to collect a larger number of particles at each time step. The main purpose of designating sub-cells within cells is to provide a sufficient particle population in a cell to calculate the field properties of the cell (rather than the sub-cell), yet maintaining sufficiently few particles in each sub-cell for computational efficiently. (The other purpose is to increase proximity of collision pairs [91] and therefore preserve flow rotation [92][93].) In this way, spatial resolution can be traded in exchange for temporal resolution with the same computational efficiency.

$$T_{x,i} = \frac{m_i}{k_B N_i^2}\left[N_i \sum^{N_i} u_i^2 - \left(\sum^{N_i} u_i\right)^2\right] \quad (1)$$

The DSMC technique is known to produce accurate results for molecular, transitional, or continuum flow regimes; however, it is typically applied to the problems involving only one of these flow regimes and requires special treatment under conditions in which all three flow regimes are realized within the same computational domain. The involvement of multiple regimes implies significant variation of particle density from one cell to another such that any choice for *F* necessarily results in too few particles per a sub-

cell in the molecular flow regime for physical accuracy or too many particles per sub-cell in the continuous flow regime for computational efficiency.

### 4.3 Adaptive Algorithm

Here, we introduce an adaptive algorithm, which adjusts *F* for each sub-cell according to sub-cell populations, to allow DSMC simulations to seamlessly transition between flow regimes where the transition boundaries are not known a-priori or are not readily defined. By allowing each sub-cell to have its own ratio between simulation particles and physically real particles, the simulation can capture the full range of flow regimes using uniform computational representation of flow physics throughout the simulation domain.

When a particle moves from one sub-cell to another with a lower *F* factor, it must be split into two particles to conserve mass, as illustrated in Figure 4.2. When a particle moves into a sub-cell with a higher *F* factor, it must be managed in one of two ways to conserve mass. It may be put into a holding array for that sub-cell until a second particle arrives for it to merge with, or it may be subjected to a fifty percent chance of being either deleted or doubled in mass. The former strictly conserves mass, and the latter conserves mass on average. Because particles can only double or halve in mass, each sub-cell *F* factor must relate to all other factors by a power of two. The concern is how to accommodate these adjustments without distorting the velocity distribution; without adding or deducting net mass, energy, or momentum from the simulation; and without biasing the simulation.

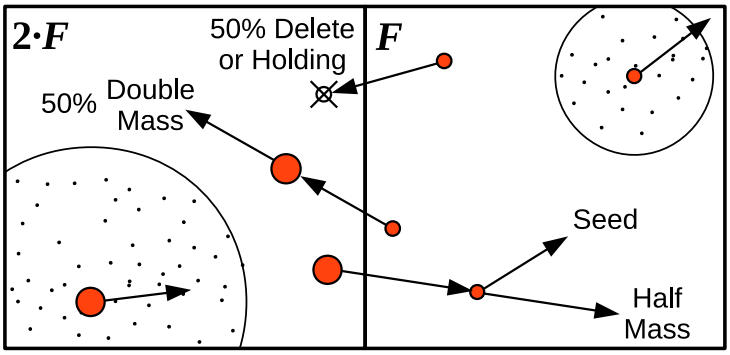


***Figure 4.2: Particle movement towards a lower F requires a split and seeded with velocity information for the new particle. Particle movement toward a higher F 50% of particles deleted and 50% doubled in mass.***

When applying the merge strategy to particles that move to a sub-cell with a higher *F* factor or to sub-cells being adjusted to a higher *F* factor, only the velocity of one of the two merging particles can be preserved. Any combination of the velocities will distort the velocity distribution. The discarded particle velocity may be greater or lower, but the velocity distribution of the deleted particles, of the particles not deleted, and of the particles prior to merging, are locally all the same distribution. Therefore, the velocity distribution is unchanged by discarding the velocity information of half of all merged particles. The potential error that a merging event introduces is equal to the resolution error of the sub-cell with the higher factor (half of a particle), so the important aspect of this error is that it not be directionally biased towards higher or lower energy. Because the velocity data of half of all merged particles is discarded, none of their information persists beyond the merge event. It is therefore expedient to use the deletion strategy instead of the holding strategy.

When a particle is split due to entering a sub-cell with a lower *F* factor, or when its sub-cell is being adjusted to a lower *F* factor, one particle adopts the original velocity

information, but new information must be generated for the second particle. This information cannot be taken from previously discarded information of merged particles because there is no one-to-one relationship between merging and splitting events. The conventional strategy, particle cloning, is to assign the same velocity information to the second particle [94][95]. (This strategy is also used when transitioning to regions of larger cell size that have the same particle density, but do not require the same spatial resolution [71].) Particle cloning should be minimized or avoided if possible due to statistical error. Specifically, the cloned particle increases the number of particles used to calculate the velocity variance, but it has zero variance relative to the original particle. As a result, particle cloning artificially reduces gas temperature. The problem is resolved by using the most current temperature and velocity sampling information from the cell to seed the second particle's velocity information. This approach is readily applicable to steady-state simulations; however, transient simulations should account for the fact that velocity information seeded into the simulation is generated from sampling a prior simulation time state.

An excessive number of particles in a sub-cell diminishes computational efficiency and insufficient particles compromises simulation accuracy. Therefore, sub-cells must double or halve their individual cell factors to maintain a local particle population close to the specified target value, $N_T$. Three options for the adjustment threshold are presented in Figure 4.3. One option is to adjust the cell factor only when the particle population exceeds double or drops below half the target population. This option moves the particle population directly to the target value; however, it also produces the widest span of particle populations. A second option is to adjust the cell factor when the local population deviates

from the target value by a multiple of $\sqrt{2}$. This option adjusts the local cell population from one bounding threshold to the other bounding threshold, which, due to random population fluctuations, will persistently produce frequent cell adjustments. When a sub-cell merges its particles to double its cell factor, it purges information from the system. When a sub-cell splits its particles to halve its cell factor, it introduces seeded information. Therefore the frequency of cell factor adjustments must be minimized. The compromise threshold used to minimize the population span and the adjustment frequency is therefore $2^{0.75} = 1.682$. If cell adjustment would result in a neighboring sub-cell factor differing by more than a multiple of two, then it is not allowed. The cells should adjust up or down together.

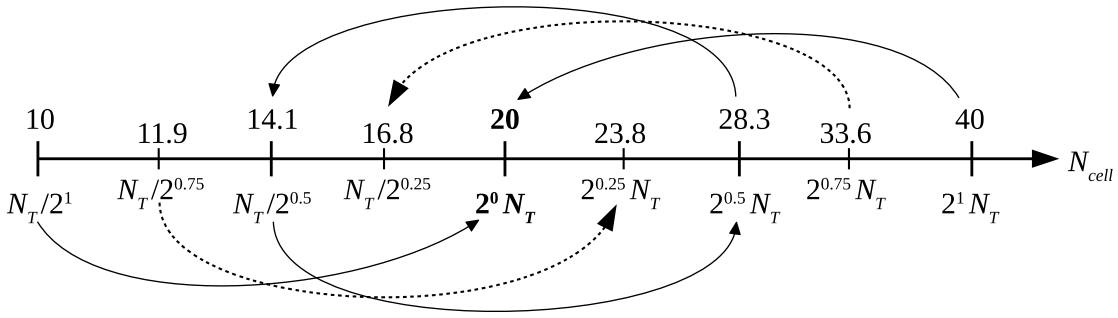


***Figure 4.3: Cell population thresholds trigger cell factor (F) adjustments. The optimal threshold to minimize adjustment frequency is a deviation factor of $2^{0.75}$ from the target population***

### 4.4 Verification Case Studies

We have applied our adaptive DSMC algorithm to reproduce the results presented for the expansion of an argon gas jet into a vacuum. The inlet conditions are a plug flow in the transitional flow regime at Mach number of three and the Reynolds number of 25. Previously, the problem was solved by treating the transitional and molecular regime flows as a continuum inviscid flow, and the solution was compared to the Method-of-

Characteristics (MOC) solution to the Bhatnagar Gross Krook (BGK) approximation of the Boltzmann Transport Equation [96]. The adaptive DSMC simulation uses the hard sphere collision model with an inlet Knudsen numbers of 0.1 and 0.01. Horizontal and vertical symmetry are applied to reduce the axially symmetric simulation to one quarter of the total 3D domain. Local density predictions are compared in Figure 4.4. The normalized density values predicted by the MOC at the flow centerline are compared to the DSMC predictions yielding Root-Mean-Square Deviations (RMSD) of 0.112 and 0.118 for inlet Knudsen numbers 0.1 and 0.01, respectively, which normalize by the MOC data ranges to 0.555 and 0.585.

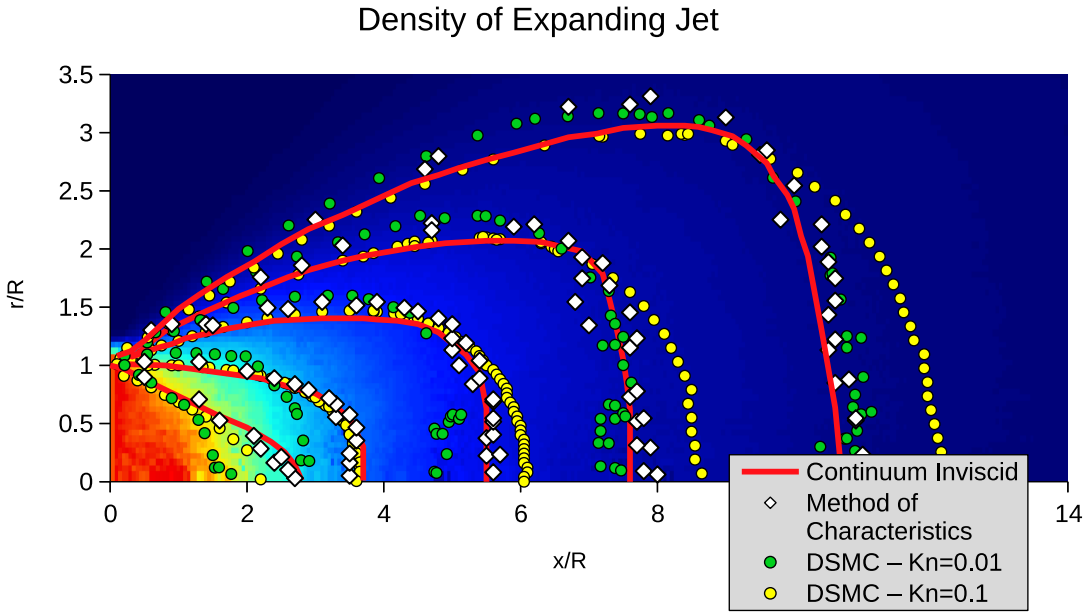


***Figure 4.4: Comparison of DSMC results, the continuum inviscid calculation, and the BGK approximation. Density contours of each (normalized to stagnation density) are at 0.1, 0.05, 0.02, 0.01, and 0.005. The background gradient is the density distribution of the DSMC simulation with inlet Kn=0.1.***

The agreement between the continuum inviscid calculation, the MOC solution to the BGK approximation, and the adaptive DSMC algorithm is expected in the rarefied transitional and molecular flow regimes in which viscosity is negligible. When the inlet

Knudsen number is reduced to 0.01, the expansion of the gas jet from the continuum flow regime differs slightly from the rarefied flow. As one would expect, including viscous effects would decreases the penetration depth of the jet due to an increased viscous momentum dissipation and this is well captured by the adaptive DSMC.

The DSMC collision model results in a simulation time that scales linearly with the number of simulation particles in a sub-cell [71]. Simulations in the transitional and molecular flow regimes may span a wide range of appropriate particle densities. In this particular jet expansion simulation, there is a region of the domain that bottoms out at an $F$ factor of unity (one simulation particle represents one real particle), as shown in Figure 4.5 for the inlet Knudsen number of 0.1. If that $F$ factor were applied throughout the domain (as is typically required for DSMC), then the simulation would require $4.72\times10^{9}$ particles, which is 130 times more than the $3.61\times10^{7}$ simulation particles used in our simulations, and the inlet cells would be populated with 70,000 particles. Because computation time scales linearly with the number of simulation particles in a cell, a parallelized simulation with a sufficient number of nodes runs 130 times faster.

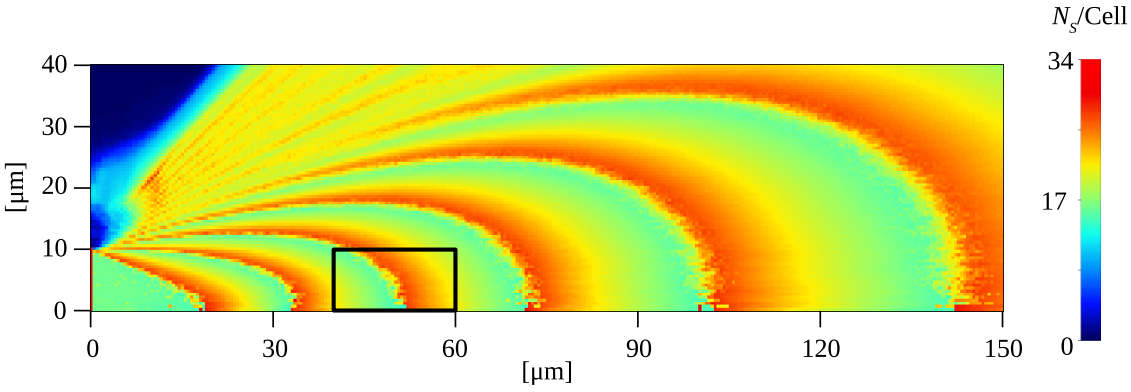


***Figure 4.5: Local cell population generated by adaptive DSMC algorithm.***

The total mass and energy entering and leaving the entire simulation domain, and those entering and leaving the rectangular sub-domain indicated in Figure 4.5 are recorded to ensure global and local conservation, respectively. The global percent difference in mass and energy are 0.33% and 3.1%. Locally, they are 0.95% and 0.70%. Data for other simulations is available in Supporting Information.

When a gas jet expands into a vacuum, it loses local thermal equilibrium. For argon gas jet simulations with inlet Knudsen number 0.1 (slip flow) and 0.01 (continuous flow), the normalized temperatures are plotted along the centerline axis in Figure 4.6. The axial temperature normalized by inlet temperature is $T_x$, and the normalized orthogonal component of temperature is $T_r$. The RMSD of $T_r$ and $T_x$ relative to data predicted by the MOC are $4.94\times10^{-4}$ and $3.98\times10^{-4}$, which normalize by the MOC data ranges to $2.11\times10^{-3}$ and $2.66\times10^{-3}$. For the inlet Knudsen number of 0.1, the axial and orthogonal components of temperatures are significantly different from each other and exactly match the predictions provided by the MOC solution. However, the lower Knudsen number simulation yields different results, which are expected due to a greater region of higher gas density in which local thermal equilibrium prevails. In both simulation cases, the axial and orthogonal temperatures distinctly separate when the Knudsen number exceeds 0.1 (flow entering the transitional regime).

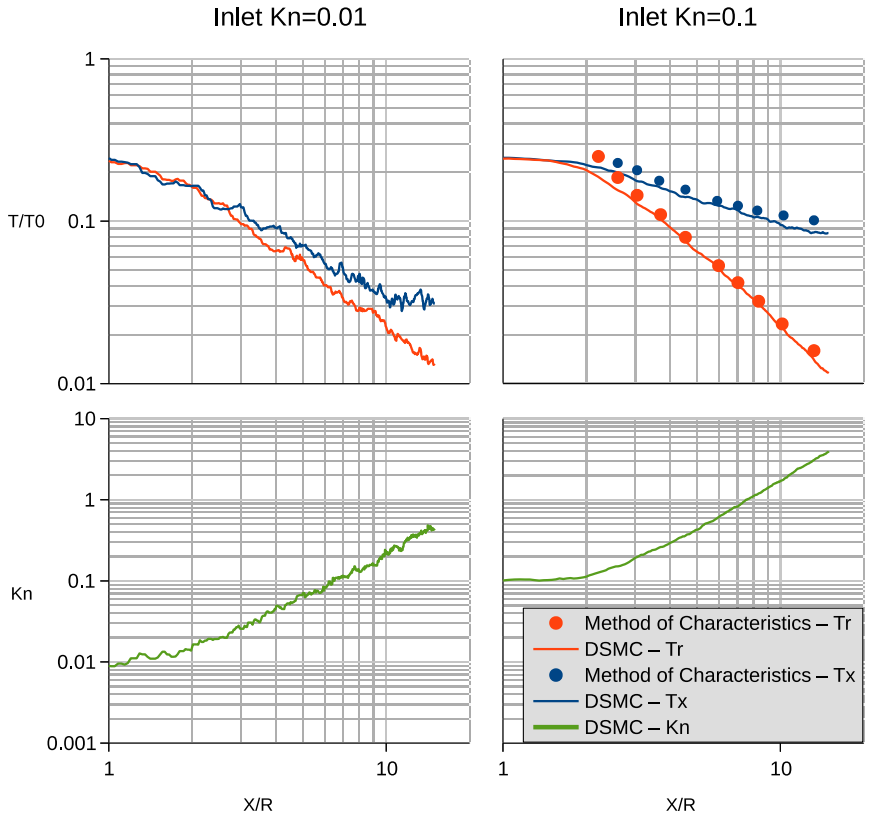


***Figure 4.6: Axial and orthogonal temperature components (normalized by stagnation temperature) and the local Knudsen number are plotted along the centerline of each argon gas jet simulation.***

Potentially the most challenging application of variable weighting factor schemes is periodic flow in which errors may feed-back upon themselves. The adaptive DSMC algorithm is applied to a periodic flow in the continuum regime to reproduce the expected temperature variation of argon gas in plane Couette flow accounting for volumetric heat generation due to viscous heat dissipation. Referring to Figure 4.7, both surfaces are maintained at $T_{Wall} = 273K$, the bottom and top surfaces are moving in opposite directions at $U_{Wall} = 100\,m/s$, the gap is $H = 1m$, the viscosity of argon is $\mu_k = 2.16 \times 10^{-5}\,kg/m\,s$, the thermal conductivity of argon is $k = 1.772 \times 10^{-2}\,W/m\,K$, and the average density is $7.04\times10^{-6}$ $kg/m^3$. Using the hard sphere Van der Waals diameter, the

Knudsen number is $Kn$~0.01. For this configuration, the analytical solution for the temperature profile is given by Equation 4.7 [85]. With reference to Figure 4.7, the entire simulation domain is divided into two sub-domains with distinct imposed weighting factors ($5.78\times10^{10}$ in the core and $1.16\times10^{11}$ near the upper and lower walls). This forced assignment of weighting factors tests the proposed merging and splitting algorithm in handling periodic flow. The simulation has an RMSD 0f 0.232 relative to the theoretical prediction, which normalizes by the theoretical range to 0.0340. This is compared to the same simulation with a single uniform weighting factor, which has an RMSD of 0.013 which normalizes to 0.0022.

$$T = T_{Wall} + \frac{2\mu U_{Wall}^2}{k}\left(\frac{1}{2Kn+1}\right)^2\left[\frac{z}{H} - \left(\frac{z}{H}\right)^2 + \frac{2m}{2c_P m - k_B}\frac{Knk_B}{\mu}\right] \qquad (4.7)$$

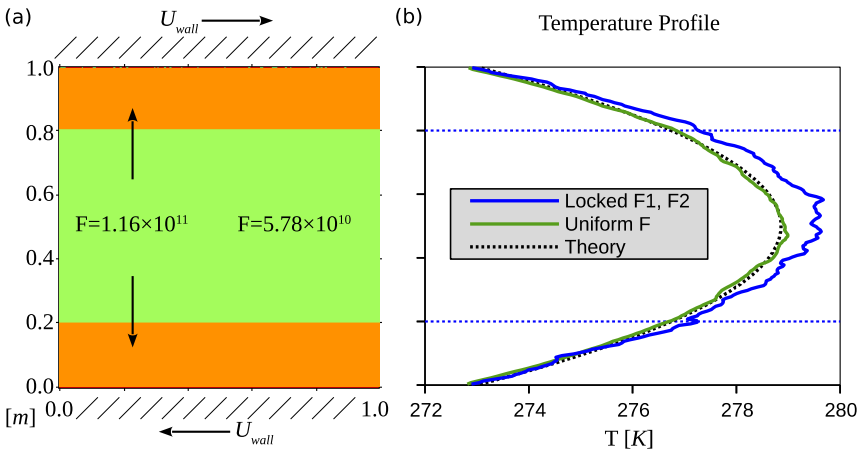


***Figure 4.7: (a) Periodic flow with imposed changes in weighting factors as a stress test for the adaptive DSMC algorithm. (b) Results are compared to DSMC with no variation in weighting factors.***

### 4.5 Complex Flow Simulations

The verification case studies demonstrated the applicability of the adaptive DSMC algorithm to the molecular and continuum flow regimes. More general problems relevant to technological applications often involve flow domains of different density where different $F$ numbers apply in complex flow structures (from continuum to molecular and back to continuum) that are not known *a priori.* One such compelling case is the gas-jet assisted FEBIP of nanomaterials, in which the experimentally observed beneficial effects produced by a continuum flow micro-jet can only be understood and fully exploited with full simulations of the gas flow [60][83][74]. Figure 4.8 shows the adaptive DSMC algorithm is able to seamlessly adapt to a complex flow, revealing – for oxygen injected at sonic velocity and $2.0\times10^{-7}$ *kg/s via* a $75\mu m$ nozzle – a stagnation pocket at the solid surface. The local Knudsen number, based on the inner diameter, indicates that the complexity of flow regimes developed in the domain preclude any *a priori* designation of regions for distinct computational strategies. A clear distinction is revealed between the free isentropic expansion of the gas jet and the region of jet interaction with the surface, which emphasize the importance of being able to simulate the domains of widely different molecular density (from molecular to fully continuous) within a uniform computational framework. Using the lowest weighting $F$ factor throughout the domain would have required $2.91\times10^{11}$ simulation particles and a maximum cell population of $2.06\times10^{6}$. The adaptive DSMC algorithm reduced the simulation particle count to $2.20\times10^{7}$, an improvement factor of 13,000.

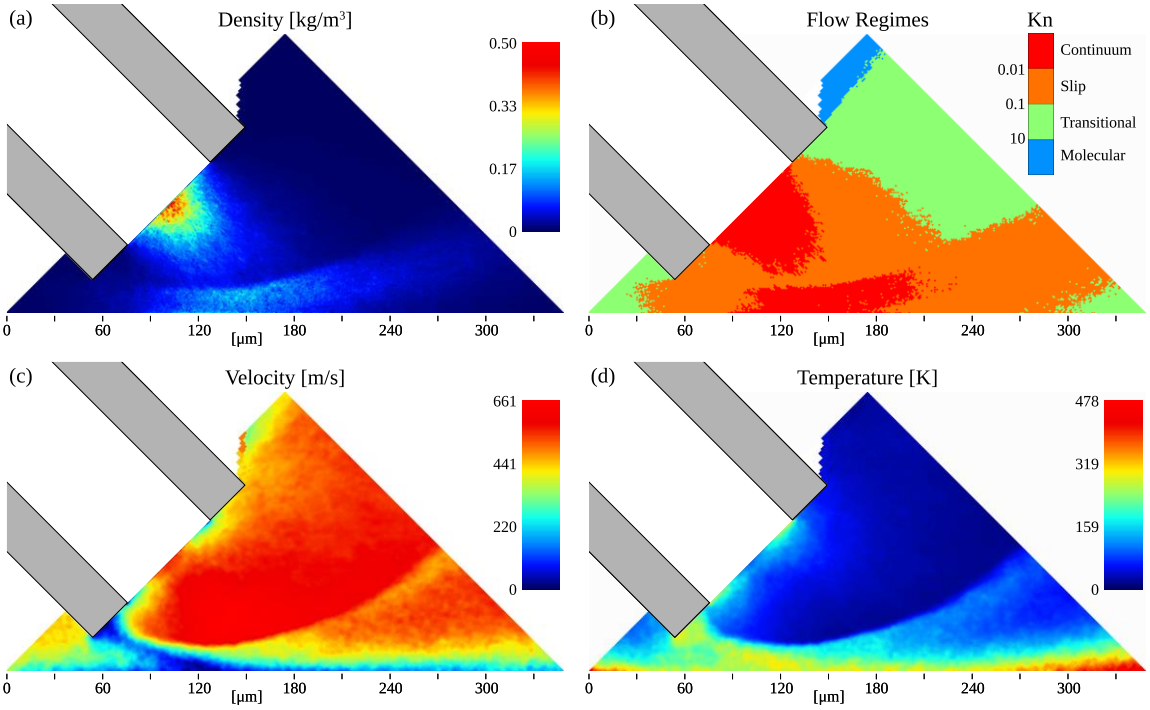


***Figure 4.8: Centerline cross-sections of adaptive DSMC results.***

Prediction of nanomaterial growth in FEBIP is defined by impingement characteristics of the gas-surface interactions, as illustrated in Figure 4.9. The spatial distribution of per-particle impingement energy is critical to determining the local molecular sticking coefficient for precursor molecules entrained in the gas jet. Depending on surface roughness, the sticking coefficient may depend on the total or the orthogonal impingement energy [28]. The sticking coefficient, combined with the spatial distribution of the impingement rate, reveal the rate of molecular precursor supply to the solid surface. Finally, the local velocity distribution, combined with impingement rate, determine the local surface temperature, which influence the diffusion rate of surface adsorbed precursor molecules [40][60].

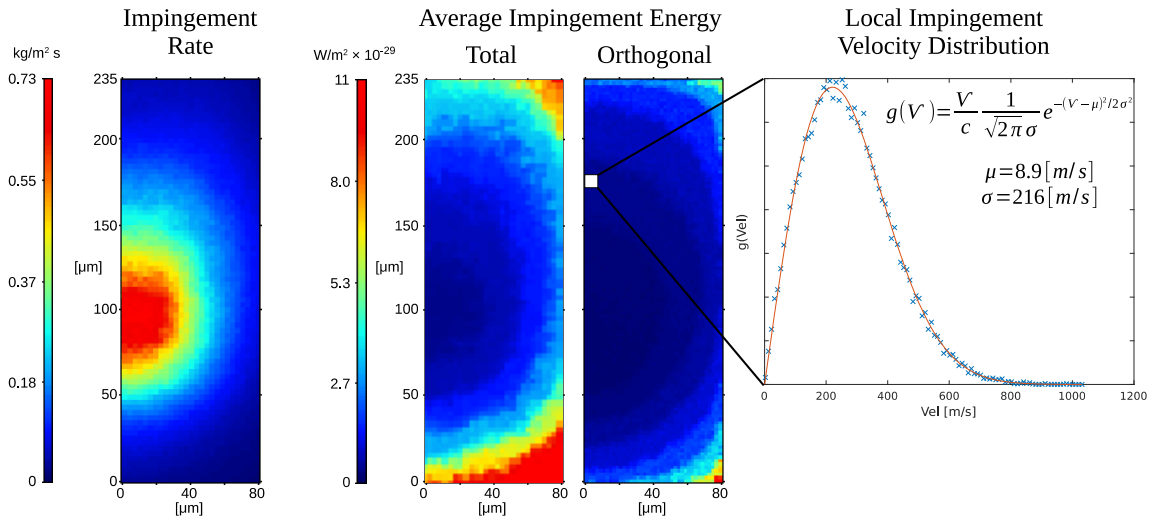


***Figure 4.9: The DSMC algorithm predicts the impingement distribution, the impingement energy, and the localized impingement velocity. This provides a comprehensive set of information on how the gas jet interacts with the surface and contributes to FEBIP of nanomaterials.***

## 4.6 Conclusions

The new adaptive algorithm developed for DSMC enables computationally efficient simulation of multi-scale gas flows without using regime specific computational techniques for different regions of the domain, thus improving simulation accuracy and computation efficiency. Central to the adaptive algorithm are 1) seeding/splitting simulation particles with the current cell property data to prevent data aliasing and 2) auto-adjusting local weighting factors (ratio of actual to simulation particles) to maintain a sufficient and not excessive number of simulation particles in each cell. We have demonstrated viability of the technique with the hard sphere collision model for each flow regime of interest by comparing results generated with the adaptive DSMC algorithm with established literature results. By using the adaptive DSMC algorithm to simulate a continuum gas jet used in FEBIP, as a challenging example, the computational speed and memory requirement were improved by a factor of 13,000 over an equivalent simulation

performed with a constant weighting factor. For adaptive DSMC, the trade-off between temporal and spatial resolution is the same fundamental trade-off as faced by standard DSMC methods. Further, the adaptive algorithm is not affected by the collision model used and has no impact on any other aspects of the computational procedure, so it should be readily adaptable as an additional tool for any DSMC software.

# CHAPTER 5: ACTIVE CONTROL OF THERMAL NON-EQUILIBRIUM OF SURFACE ADSORBED MOLECULES ENABLES NEW MODES OF DIRECT WRITE NANOFABRICATION

The sticking coefficient and surface diffusion rate of deposition precursor molecules allow, enhance, and/or modulate various additive nanofabrication techniques. The diffusion rate depends on the effective temperature of adatoms, which is found to differ significantly from the surface temperature and can be drastically altered *via* gas impingement in previously unpredictable ways. Because the adatom temperature cannot be directly measured, the modified hard-cube model using Lennard-Jones 12-6 potential parameters is developed to quantify the gas-adatom and adatom-surface interactions in order to predict the effective adatom temperature. The model is verified by accurately predicting the experimentally measured thermal response of the surface due to gas jet impingement, and to predict an experimentally measured sticking coefficient reported in literature. Understanding of the adsorbed layer effective temperature and how it can be controlled *via* gas jet impingement provides new degrees of freedom in controlling processes dependent on surface diffusion. These include enhanced diffusion of precursor molecules without bulk heating and extremely localized regions of high diffusivity, which enable new modes of additive nanofabrication.

## 5.1 Motivation

Surface diffusion of adatoms is a critical factor in thin layer deposition and other forms of nanoscale fabrication with a limitless range of applications. In general, a higher surface diffusion rate of adatoms increases epitaxial growth rates [97][98] and improves deposition quality by preventing the dendrite formation that may occur in diffusion limited growth regimes [99][100]. And the diffusion rate can be modulated to adjust deposition

properties, such as increased porosity or increased grain size [101]. Conventionally, this is done by increasing or decreasing temperature; however, experiments show that gas impingement to the substrate also modulates surface diffusion. In some cases, increased gas impingement decreases diffusion [102][103]. In other cases, gas impingement enhances diffusion [60][99].

Modes of enhanced (or diminished) surface diffusion can be accessed *via* an externally applied energetic molecular beam that activates surface diffusion, not by heating the surface, but by bringing adatoms into a state of strong thermal non-equilibrium with the surface. Since there is no way to directly measure the adatom temperature without perturbing its intrinsic thermodynamic state, the only alternative is to rely on the predictions using a suitable model capturing the key physics of interactions and validated by comparison to carefully designed control experiments. To this end, the classical hard-cube model (Figure 5.1.a) is modified to include three interacting bodies (Figure 5.1.b) such that the effective temperature of the middle body, the adatom, may be determined. In the classical hard-cube model, the tangential velocity of an impinging particle is conserved, and the velocity normal to the surface is used in an elastic collision with a surface adsorption site to determine the post-collision particle energy. In the original application of this model, the post-collision particle energy is compared to the adsorption energy to predict the sticking coefficient of precursor deposition molecules to the substrate [28][104]. It is expanded here to also predict the adatom and surface temperatures in response to energized gas impingement. Application of the hard-cube model in the prediction of temperature is verified by predicting complex heating and cooling surface profiles in response to gas jet impingement, which can be used to bring the surface adsorbed precursor

molecules into an excited thermodynamic state favorable for locally controlled nanofabrication. For example, modulation of the surface adsorbed precursor state by a supersonic inert gas jet in Focused Electron Beam Induced Deposition (FEBID) shows an enhancement of the surface adsorbed precursor diffusion rate (and therefore the nanostructure growth rate) by 10x [60], indicative of substantially elevated adatom temperature while the substrate temperature is predicted to rise by less than $0.01K$. Predictions by the modified hard-cube model reported here reveal that using an energetic jet impingement, one can dramatically elevate the effective temperature of adatoms - bringing them into a state of thermal non-equilibrium with the surface with significant beneficial effects, such as enhanced growth rate, improved deposit morphology and structure, for many nanofabrication techniques that rely on the optimal state of the surface adsorbed precursor.

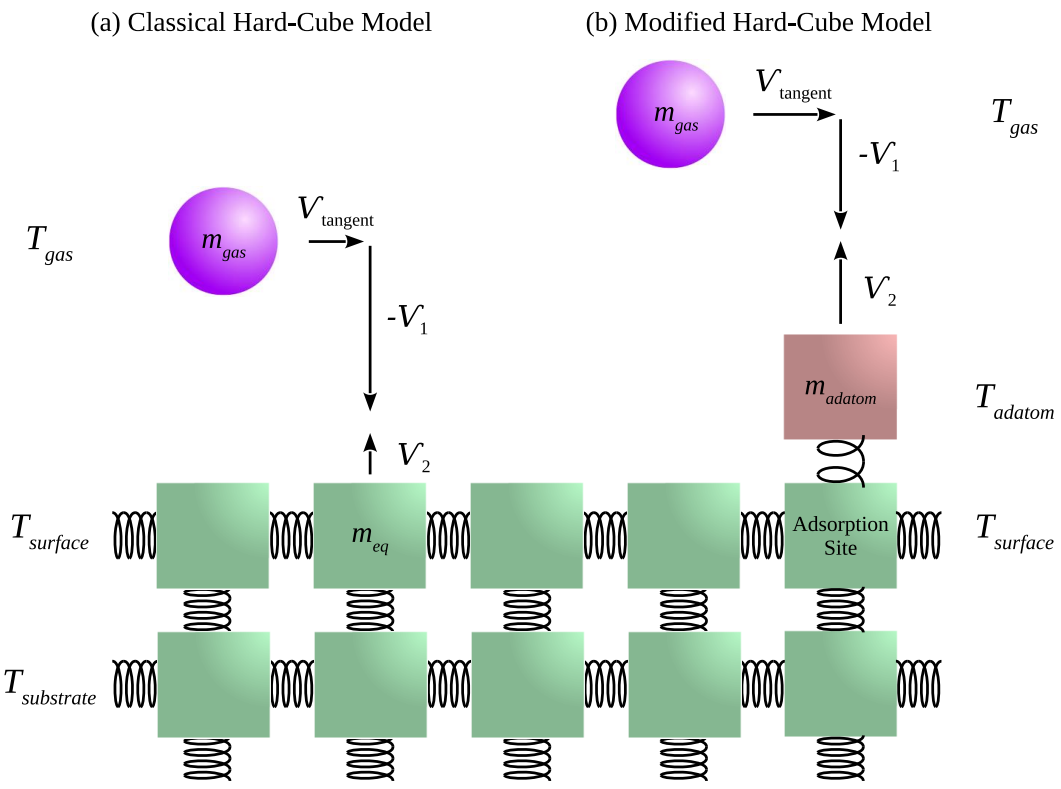


***Figure 5.1: (a) The classical hard-cube model is used to predict the surface temperature. (b) The modified hard-cube model is used to predict the adatom effective temperature.***

## 5.2 Experimental Measurements of Surface Temperature

In order to validate the classical hard-cube model in prediction of the adsorption layer temperature, its predictions of the surface temperature response to a gas jet are compared against spatially-resolved local temperature measurements. The magnitude of the thermal response is limited by the thermal conductivity of the substrate. Borosilicate glass, which has a low thermal conductivity, is selected to increase thermal sensitivity to gas impingement. An RTD of dimensions 20$\mu m$ by 20$\mu m$ was fabricated on the substrate with deposition of a 10$nm$ chromium/35$nm$ platinum high electrical resistance serpentine pattern supported by low resistance legs, which is covered by a thin layer (~10$nm$) of silicon

dioxide to protect the RTD from oxidation. The RTD response was calibrated in a temperature controlled oven, showing the expected linear behavior of electrical resistance vs temperature. During operation, the substrate is mounted to a nano-scale positioning table in a scanning electron microscope (SEM) vacuum chamber such that the RTD position relative to the gas jet can be directly controlled as indicated in Figure 5.2.a and b. Data is collected in steps of 20$\mu m$ (equal to the effective size of the "measurement point") to map the thermal response profile over the 2D surface. Measurement of each RTD position stabilizes to quasi-steady state in sub-second time, which indicates that the heat flux to the substrate and the far-field ambient temperature of the substrate can be considered constants for the duration of collection at each data point.

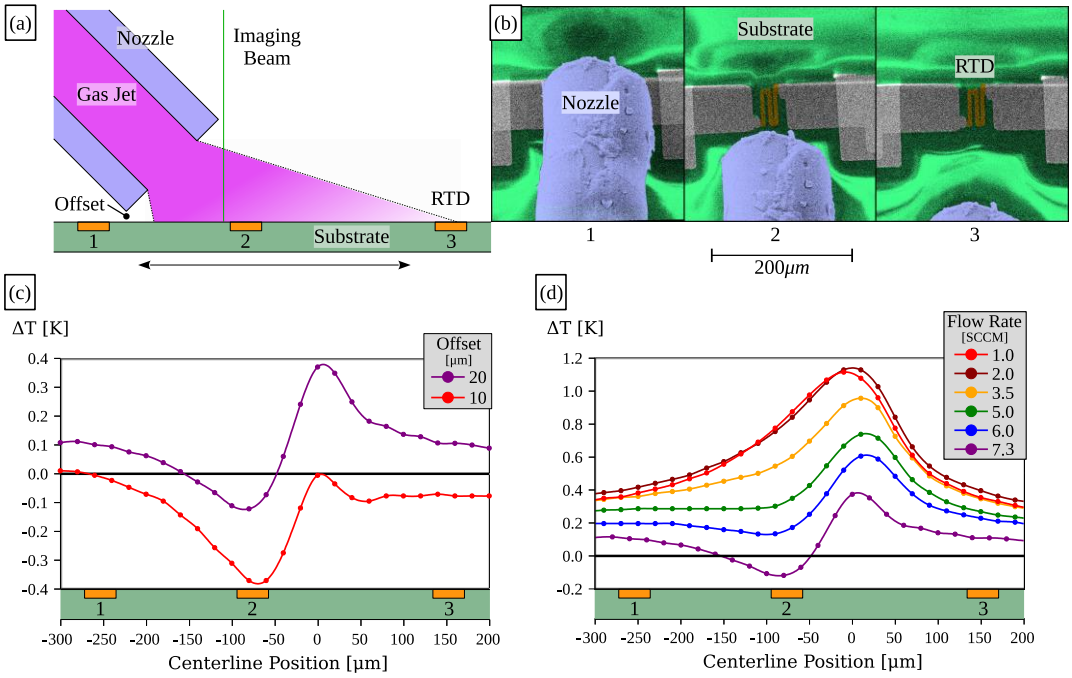


***Figure 5.2: (a) Schematic side-profile of the RTD lateral translation range. (b) The SEM top-view. (c) Thermal response to a 7.3 ± 0.1 sccm oxygen gas jet with a 10μm and 20μm vertical offset from the substrate. (d) Thermal response to various flow rates***

***of oxygen gas with a 20μm offset from the substrate. RTD temperature measurement uncertainty is ± 0.002K.***

During measurements, the gas jet nozzle is mounted at a 45° tilt from the surface normal and the 138$\mu m$ outer diameter edge is offset 20$\mu m$ above the substrate. Gas jets exit the 75$\mu m$ inner diameter nozzle at sonic velocity in the continuum flow regime at a stagnation temperature equal to the substrate far-field temperature. Detailed 2D surface maps of RTD measurements are collected for argon gas jets at 4.3 ± 0.14 and 7.0 ± 0.14 *sccm* flow rate with exit Knudsen numbers (defined by the ratio of the mean free path of gas molecules to the nozzle inner diameter) of 0.009 and 0.005, respectively, and an oxygen gas jet of 7.3 ± 0.1 *sccm* with a Knudsen number of 0.006 (see additional data in Appendix D). Representative centerline temperature profiles are collected with the oxygen gas jet at varying flow rates and reported in Figure 5.2.c. The peak differential thermal response, defined relative to the equilibrium far field substrate temperature, occurs in the slip flow regime between 1.0 and 2.0 *sccm* with Knudsen numbers 0.04 and 0.02, respectively. At lower flow rates (not shown due to lesser relevance), the thermal response diminishes due to the diminished gas particle impingement rate to the substrate. At higher flow rates, the effect of isentropic acceleration is diminished due to the formation of a stagnation region at the substrate surface. For Figure 5.2.d, centerline differential temperature profiles are collected with the oxygen gas jet of 7.3 *sccm* with vertical offsets of the nozzle tip from the substrate of 10$\mu m$ and 20$\mu m$. The thermal response profiles are comparable, but shifted by an average of 0.2$K$. The higher surface temperature at the greater offset distance is due to a slightly increased path length for isentropic expansion resulting in increased peak impingement velocity and increased kinetic energy delivered to the surface.

### 5.3 Prediction of Surface Temperature via the Classical Hard-Cube Model

In order to predict the surface temperature response to a gas jet, the distribution of gas particle impingement to the surface and the velocity distribution at each surface location must be determined. The Direct Simulation Monte Carlo (DSMC) method was applied to simulate the gas flows for the experimental configurations. Each simulation compiled a log of every particle that impinged upon the substrate, its velocity orthogonal to the substrate, its location on the substrate, and its time of impact. This information is then sorted into finite substrate elements of $10\mu m \times 10\mu m$, which provides the gas impingement rate for each substrate element. Particles in each element are then sorted into a velocity histogram. The expected form of a velocity distribution orthogonal to the substrate is $g(\mathrm{V}_0) = c(-\mathrm{V}_0)f(\mathrm{V}_0)$ where $f(V_0)$ is the Gaussian distribution $\exp\left[-(\mathrm{V}_0 - \mu)^2/2\,\sigma_{gas}^2\right]/\sqrt{2\pi}\,\sigma_{gas}$, and it is weighted by a particle's orthogonal velocity $V_0$ towards the substrate. This equation is fitted to each sampled velocity histogram *via* linear regression to obtain the distribution parameters $c$, $\mu$, and $\sigma$, where $\mu$ indicates the mean orthogonal velocity of gas and the standard deviation $\sigma$ indicates the gas temperature immediately above the substrate. The rate of impingement, mean orthogonal velocity, and gas temperature are used with the classical hard-cube model to predict the substrate thermal response [28].

The velocity distribution of gas particles adjacent to the substrate is defined by the Gaussian distribution based on the parameters obtained *via* DSMC. However, the particles that collide with a surface adsorption site are accelerated by addition of the adsorption energy $E_{ads}$ according to Equation 5.1 [28]. Since $V_0$ maps directly to $V_1$, the probability distribution $g(V_1)$ of particles impinging upon the substrate can be expressed as $f(V_0)$

weighted by the relative velocity between a particle and a surface adsorption site (requiring that $V_2 > V_1$), and weighted by the probability distribution $g(V_2)$ of the surface adsorption site velocities being impinged upon by gas particles, as indicated by Equation 5.2. By symmetry, $g(V_2)$ is given in Equation 5.3 where $f(\mathrm{V}_2) = \exp\left[-\mathrm{V}_2^2/2\,\sigma_{surface}^2\right]/\sqrt{2\pi}\,\sigma_{surface}$ is the Gaussian velocity distribution of surface adsorption sites and $\sigma_{surface}$ is the standard deviation of velocity, which is dependent on the surface temperature $T_{surface}$ and its equivalent mass $m_{eq}$.

$$\frac{1}{2}M_1\mathrm{V}_0^2 + E_{ads} = \frac{1}{2}M_1\mathrm{V}_1^2 \tag{5.1}$$

$$g(\mathrm{V}_1) = \int (\mathrm{V}_2 - \mathrm{V}_1)\, f(\mathrm{V}_0) g(\mathrm{V}_2) d\mathrm{V}_2 \tag{5.2}$$

$$g(\mathrm{V}_2) = \int (\mathrm{V}_2 - \mathrm{V}_1)\, f(\mathrm{V}_2) g(\mathrm{V}_1) d\mathrm{V}_1 \tag{5.3}$$

Since a surface adsorption site is elastically coupled to the rest of the substrate, it is modeled by an equivalent mass somewhat greater than the actual adsorption site mass and is typically increased by a factor between one and two [105]. Earlier implementations of the classical hard-cube model used a factor of three [104]. Since this is the least defined parameter, its impact is considered in the uncertainty of all results. The post-collision velocity of the impinging particle is calculated in Equation 5.4 where $\mu$ is the ratio of impinging particle mass to the hard-cube mass. This is used to determine how much energy is transferred to the substrate and whether the post-collision particle energy is greater than the adsorption energy. If the particle final energy is greater than $E_{ads}$, then the sticking

coefficient is zero for the particular $V_1$ and $V_2$ pairing; otherwise it is one [28]. Integrating the energy delivered and the sticking coefficient across all surface adsorption site velocities and all impingement particle velocities provides both the average energy $E_{avg}$ delivered per particle (Equation 5.5) and the sticking coefficient $S$ at the given substrate element (surface site). The energy captured by the substrate due to a particle sticking is neglected because it is equal, on average, to the energy released in desorption when the rate of adsorption is equal to the rate of desorption (quasi-steady-state).

$$\mathrm{V}_1^{\mathrm{I}} = \frac{\mu - 1}{\mu + 1}\mathrm{V}_1 + \frac{2}{\mu + 1}\mathrm{V}_2 \tag{5.4}$$

$$E_{avg} = \int\int 0.5 M_1\left(\mathrm{V}_1^2 - V_1^{*2}\right) g(\mathrm{V}_1) g(\mathrm{V}_2) d\mathrm{V}_1 d\mathrm{V}_2 \tag{5.5}$$

In the case of single-layer adsorption, the fraction of occupied surface adsorption sites $\theta$ is given by Equation 5.6 where $P$ is the local gas pressure, the rate constants of adsorption and desorption are $k_{ads} = r_{ads}/P(1-\theta)d$ and $k_{des} = r_{des}/\theta d$, and $d$ is the number of adsorption sites per unit area. The rates of adsorption and desorption are $r_{ads} = S(1-\theta)(JA)$ and $r_{des} = \theta A d\upsilon \cdot exp\left(-E_{ads}\, M_1/k_B\, T_{surface}\right)$, $J$ is the rate of gas particle impingement per unit area, $A$ is the surface area, and $\upsilon$ is the desorption attempt frequency [106]. Consolidating terms allows the fraction of occupied surface adsorption sites to be expressed with readily obtained values as indicated in Equation 5.6.

$$\theta = \frac{(k_{ads}/k_{des})P}{1 + (k_{ads}/k_{des})P} \rightarrow \frac{SJe^{E_{ads}M_1/k_B T_{surface}}}{d\upsilon + SJe^{E_{ads}M_1/k_B T_{surface}}} \tag{5.6}$$

If the region of gas impingement to the surface is approximated as a disk of diameter $D$ and uniform surface temperature $T_{surface}$, then the rate $Q_2$ of thermal energy dissipated from that disk into the substrate is given by Equation 5.7 where $k$ is the thermal conductivity of the substrate material [107]. However, neither the temperature nor the impingement rate is uniform over the disk area. In order to compare the heat flux delivered by the gas jet to the heat flux dissipated into the substrate, analysis of each finite substrate element is considered as though the local impingement rate and the impingement velocity distribution are representative of the entire impingement region. The diameter of the equivalent disk region is calculated from the total area with an impingement rate greater than half the maximum jet impingement rate; this is approximately $100\mu m$ in our experiments. The rate $Q_1$ of energy delivered by the gas jet to the disk area (representing a specific finite surface element) is indicated in Equation 5.8. Since quasi-steady-state measurements are obtained within a sub-second response time of moving to a new finite substrate element, $Q_1$ must equal $Q_2$, which allows prediction of the local surface temperature $T_{surface}$.

$$Q_2 = \underbrace{2D}_{\text{Shape Factor}} \; k\left(T_{surface} - T_{substrate}\right) \tag{5.7}$$

$$Q_1 = J \underbrace{\left(\pi D^2/4\right)}_{\text{Area}} \underbrace{\left(1-\theta\right)}_{\text{Available Sites}} E_{avg} \tag{5.8}$$

The thermal conductivity of the borosilicate glass substrate is $k = 1.2\,W/mK$. The bulk number density of silicon dioxide groups is $n = 2.24 \times 10^{18} m^{-3}$, which yields the density of surface adsorption sites in the surface layer as $d = n^{2/3} = 7.93 \times 10^{18} m^{-2}$. The adsorption energies and vibrational frequencies are calculated based on the Lennard-

Jones 12-6 potential parameters in Table 5.1, which is an appropriate model for closed-shell physisorption bonds. Specific pairings between components are calculated *via* the customary Lorentz-Berthelot mixing rules. The desorption attempt frequency is calculated by equating the parabolic term of the 12-6 potential curve to a spring model in order to identify the approximate spring stiffness $k_s = 72\, E_{ads}/2^{1/3}\, \sigma_{L\text{-}J}^2$ and the frequency $\upsilon = (k_s/m)^{1/2}/2\,\pi$.

***Table 5.1: Lennard-Jones 12-6 Potential Parameters***

| Material | Phase* | $E_{ads}$ [J] | $\sigma_{L\text{-}J}$ [$m$] | Ref. |
|---|---|---|---|---|
| Silicon Dioxide | S-S | $9.972\times10^{-22}$ | $3.265\times10^{-10}$ | [108] |
| Argon | G-G | $1.654\times10^{-21}$ | $3.405\times10^{-10}$ | [108] |
| Oxygen | G-G | $1.695\times10^{-21}$ | $3.382\times10^{-10}$ | [108] |
| Tungsten Hexacarbonyl | G-G | $4.317\times10^{-21}$ | $3.400\times10^{-10}$ | [109] |
| *S-S denotes solid phase, G-G denotes gaseous phase | | | | |

## 5.4 Hard-Cube Model Validation

The RTD measured and hard-cube predicted surface temperature responses to the 7.0 *sccm* argon gas jet and 7.3 *sccm* oxygen gas jet are displayed in Figure 5.3. The coupled DSMC-Hard-Cube predictions capture both the magnitude and complex features (transition between cooling and heating) of the surface RTD measurements. In the region farthest from the nozzle, the model predicts a $\Delta T$ that vanishes to zero, while the experimental results maintain a value of 0.2*K*. In this region, the impingement rate is low, and no thermal response is expected. However, the gas is accelerated to its near terminal velocity, and the direction vector of mean velocity is nearly tangent to the surface. Consequently, tangential velocity interaction with the surface becomes the dominant contributor to surface heating despite generally being a negligible factor [28] that is excluded from the hard-cube model. In the region directly under the nozzle, the model and

experimental measurements indicate a slight cooling effect. Particles that reach this region of the surface must depart from the jet centerline at an abrupt angle, resulting in a diminutive mean velocity as compared to other regions of the gas jet. Concurrently, the temperature of these particles is significantly reduced from the stagnation temperature. The resultant total root-mean-square velocity of impingement gas particles corresponds to a lower than ambient temperature, which cools the surface. The model results in Figure 5.3 are predictions for an equivalent mass factor of 1.5, and results generated with factors of one and two are indistinguishable from the reported results, which indicates low sensitivity of the surface temperature on the equivalent mass of the surface adsorption site.

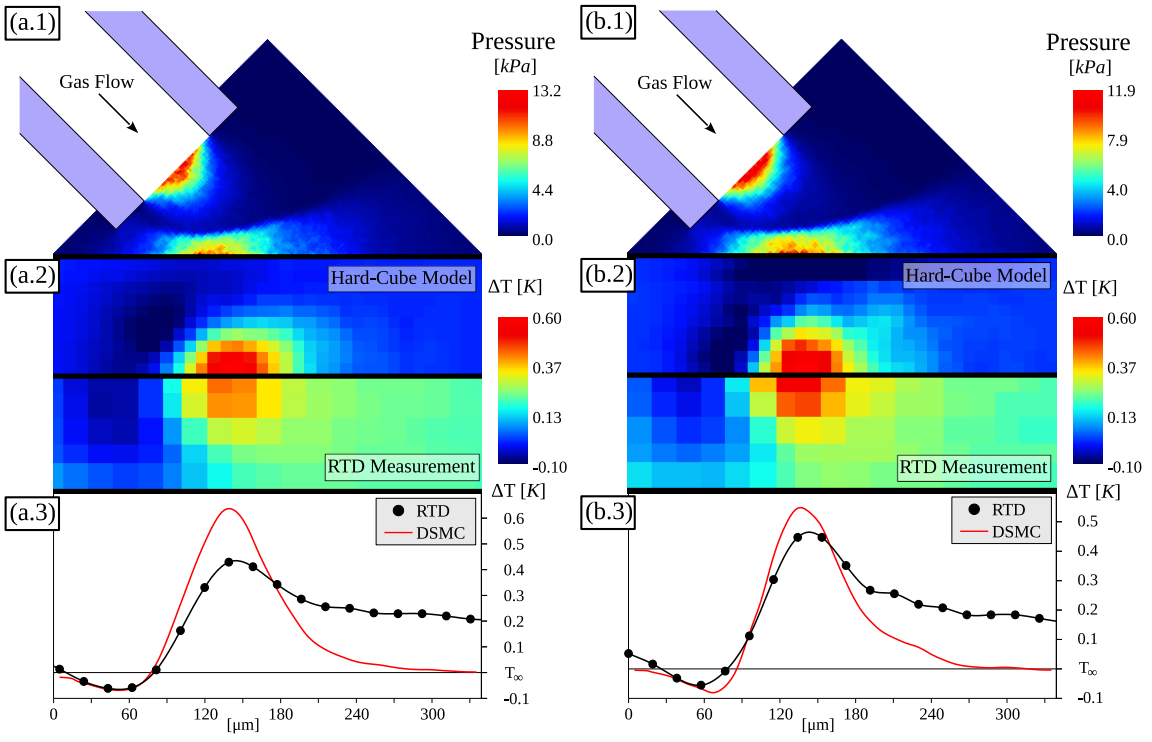


***Figure 5.3: RTD measurements and coupled DSMC-Hard-Cube model predictions for (a) 7.0 ± 0.1 sccm argon gas jet and (b) 7.3 ± 0.1 sccm oxygen gas jet. (1) The cross-section view of the pressure field via DSMC. (2) Surface maps of the thermal response via model predictions and RTD measurements. (3) Centerline profiles of the thermal***

***response via model predictions and RTD measurements. RTD temperature measurement uncertainty is ± 0.002K.***

## 5.5 Prediction of Adatom Temperature via the Modified Hard-Cube Model

The modified hard-cube model is next applied to predict the adsorption layer temperature. In the same manner that the surface temperature was determined by adjusting the adsorption site temperature such that the energy supplied by gas impingement and heat dissipated into the substrate are balanced, the adsorption layer temperature is determined by adjusting the adatom temperature such that the energy of impinging gas molecules that is transferred to the adsorption site is equal to the heat rejected from the adatom to the substrate. Thus, as indicated in Figure 5.1.b, the hard cube in the modified hard-cube model is the adsorbed molecule. Since the adatom is weakly bound to the substrate, its equivalent mass factor is one. The average energy, identified here as $E_1$, delivered to an adatom from a gas particle is given by Equation 5.5. The rate of energy delivered to the adatom depends on the average energy delivered per impingement particle and the impingement rate to the adatom as indicated in Equation 5.9.

$$q_1 = (J/d)E_1 \tag{5.9}$$

Regarding the thermal energy transfer from the adatom to the substrate, there are three possibilities. The first possibility is that the adatom undergoes an elastic collision with the substrate at a frequency $\upsilon$ corresponding to the adatom's vibrational frequency. This is a limiting case in which the high frequency of energy exchange forces the adatom to equilibrate to the surface temperature. However, in contrast to an impinging particle which does undergo an elastic collision with the surface, an adsorbed particle oscillating at

the trough of an energy well is not colliding with the surface. Since the adatom is known to be in a highly non-equilibrium state relative to the surface, the vibrational energy exchanged between adatoms and the surface adsorption site is negligible relative to other factors. The second possibility is that the adatom exchanges no energy with the surface adsorption site. This is the other limiting case in which the adatom equilibrates with the impinging gas particles. In the third possibility, the impinging gas particles are driving adatoms to collide with adsorption sites at the frequency of gas particle impingement. These three possibilities are represented by Equation 5.10 where $E_2$ is the average hard-cube energy transfer from the adatom to the surface adsorption site as determined by Equation 5.5. Since the adatom is residing in the surface energy well, the attractive energy of adsorption cannot accelerate adatom motion and its Gaussian velocity $V_0$ distribution is therefore the same as that of the impinging particles, i.e. $\mathrm{V}_1 = \mathrm{V}_0$.

$$q_2 = \begin{cases} \upsilon E_2 & \text{Limit of } T_{adatom} = T_S \\ 0 & \text{Limit of Complete Decoupling} \\ (J/d)E_2 & \text{Impingement Driving Frequency} \end{cases} \tag{5.10}$$

As an example relevant to nanofabrication applications for e-beam direct-write of nanostructures (FEBID), the adsorption layer temperature is predicted for tungsten hexacarbonyl precursor molecules introduced with an argon carrier gas jet with the flow rate of 4.3 *sccm* as indicated in Figure 5.4. The predicted and measured surface $\Delta T$ is compared in Figure 5.4.b and c for the borosilicate glass substrate used in the hard-cube model validation experiments. In nanostructure growth experiments, FEBID is done with a silicon dioxide surface layer on a silicon substrate ($k = 148\,W/mK$) [83]. While the peak thermal response for such a substrate is predicted to be less than 0.01 *K*, the expected effective temperature of adsorbed tungsten hexacarbonyl is given in Figure 5.4.d, along with the predicted precursor sticking coefficient in Figure 5.4.e. Importantly, within the region of elevated gas particle

impingement, the adatom experiences a significant temperature rise $\Delta T$ (anywhere between 35$K$ and 130$K$ depending on the strength of molecular interactions between the adsorbed molecules and substrate), which is consistent with the experimentally observed enhanced surface diffusion and an increase in the growth rate [83]. Outside this region, the adsorption layer temperature is predicted to drop below the substrate temperature, suggesting diminished surface diffusion. However, due to the diminished impingement frequency outside the gas jet impact region, the weak energetic coupling between the adatom and the surface is expected to become a contributing factor to adatom temperature, drawing the adatom temperature towards the surface temperature.

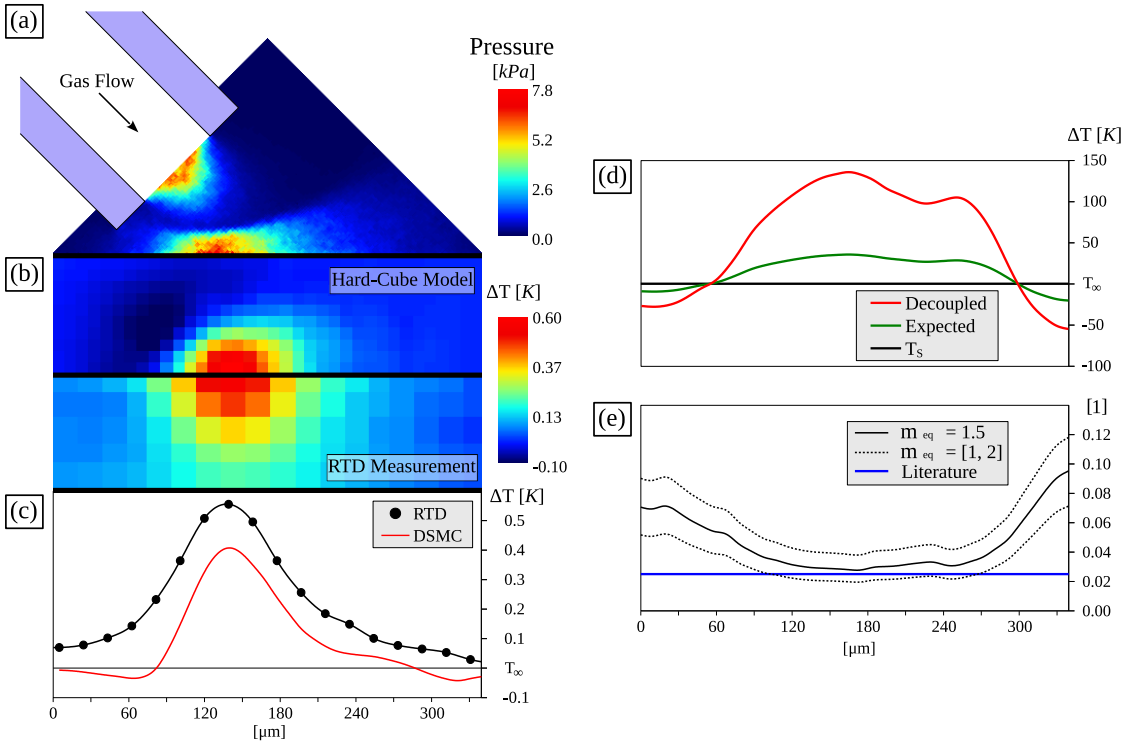


***Figure 5.4: (a) The cross-section view of the pressure field via DSMC for an argon jet at the flow rate 4.3 ± 0.14 sccm. (b) Surface maps of the thermal response via the modified DSMC-Hard-Cube model predictions and RTD measurements. (c) Centerline profiles of the thermal response via model predictions and RTD measurements. (d) Adatom temperature predictions for the three possible scenarios interaction strength between an adsorbed layer and the surface. (e) The sticking coefficient of tungsten hexacarbonyl onto silicon dioxide and the corresponding sticking coefficient measured in literature [29]. RTD temperature measurement uncertainty is ± 0.002K.***

When tungsten hexacarbonyl is injected as a minority species in a continuum flow carrier gas its particle velocities approximately match the carrier gas particle velocities [110]. Therefore the argon jet impingement velocity distributions generated by DSMC are used to calculate the tungsten hexacarbonyl sticking coefficient via the hard-cube model. As indicated in Figure 5.4.e, the equivalent mass factor has a significant impact on the sticking coefficient but does not preclude meaningful estimation of the sticking coefficient. The sticking coefficient predicted via the hard-cube model is consistent with an experimentally determined sticking coefficient for tungsten hexacarbonyl on a silicon dioxide surface [29].

### 5.6 Outlook

In summary, we have developed a hybrid DSMC-hard-cube model for predicting the local temperature of an adsorbed layer suitable for application under non-equilibrium conditions. The model was verified through detailed microscopic measurements of the thermal response of a surface subjected to supersonic gas jet impingement in vacuum. Further, by considering data from the FEBID nanostructure growth experiments, we showed that the model may be applied to predict the effective adsorption layer temperature and its impact on the precursor molecular surface diffusion rates. Since the predicted adatom temperature has little dependence on the equivalent mass factor, and all other parameters are readily determined from the first principles, the described method enables making quantitative predictions for any solid/adsorbate pairs in vacuum upon energetic stimulation *via* gas impingement with no use of empiricism. This creates the unique opportunity to access modes of enhanced surface diffusion without bulk substrate heating – which may be destructive to desired surfaces features – and within a spatially confined

domain should the adsorbate surface mobility be undesirable in neighboring regions. The ability to predict the sticking coefficient and adatom effective temperature (diffusion rate) can be combined in the surface transport equation [40] to predict the precursor molecular supply rate for nanostructure fabrication using emerging beam-based direct-write techniques [111].

# CHAPTER 6: CONCLUSIONS AND RECOMMENDATIONS FOR FUTURE WORK

In this thesis a new approach to FEBID use of a continuum flow gas injection system is presented to address the ongoing challenges of FEBID, namely deposition rate, deposition purity, and the thermal competition between surface diffusion and precursor adsorption, to contribute to and promote ongoing development and application of FEBID as a nanofabrication technique. In Chapter 2, impingement *via* a continuum gas jet was shown to increase deposition rate to parity with FIBID. The fact that this enhancement is due only to the kinetic activation of surface adsorbed precursor molecules indicates that the chief advantage of FIBID is that impinging ions deliver sufficient kinetic energy to locally stimulate diffusion. In Chapter 3, the continuum gas jet was demonstrated – particularly when heated – to enhance deposit purity. Since operation with a continuum gas jet *via* carrier gas is naturally compatible with other methods of *in situ* techniques to enhance purity, it is expected that FEBID can operate on full parity with FIBID, but at higher resolution and without damaging the substrate.

Since gas flow and impingement is appreciably more complex with a continuum gas jet than a molecular gas jet, the DSMC method was adapted to provide impingement flux information just as electron trajectory Monte Carlo simulations have provided secondary electron distribution information for FEBID modeling. Therefore, the continuum gas jet method can be directly incorporated into the existing growth predictions based on the reaction-diffusion equation coupled with Monte Carlo input. The new piece of information in Chapter 6 (that is not exclusive to continuum gas jets), is that the adsorption layer effective temperature is strongly dependent upon gas impingement. The hard-cube model

(verified by surface temperature predictions) provides a new tool for predicting the adatom temperature for use in growth simulations. By extension, the surface adsorbed precursor diffusion rate can be predicted based on material properties and the adatom temperature. This, combined with the precursor impingement flux and sticking coefficient, is sufficient to determine (*via* the surface transport equation [40]) the maximum achievable deposition rate prior to experimental testing. Further refinement of this model for predicting adatom temperature is the most immediately interesting direction for future research.

The strong thermal non-equilibrium between the adatom and the surface (due to the adatom's weak thermal coupling to the surface adsorption sites) means that the substrate temperature has little bearing on the adatom temperature when exposed to a continuum gas jet. It may therefore be advantageous to cool the substrate to increase sticking coefficient while simultaneously maintaining enhanced surface diffusion.

# APPENDIX A. NOZZLE PREPARATION FOR HIGH TEMPERATURE OPERATION IN VACUUM

Current best practices for the construction of temperature-adjustable, continuum flow, micron-scale diameter, vacuum nozzles that do not introduce contaminants to either the gas or the vacuum chamber are presented for reference. A nozzle mount that already has a heater built onto it may be recycled with new capillaries to replace broken ones.

## A.1 Construction

Previous success is based on Resbond 920 as the ceramic (maximum temperature: 1650°*C*). After initially applying the ceramic between the silica nozzle and metal sheath, it has to set in ambient conditions for 24*hrs* (or at 65°*C* for 4*hrs*). At this point the seal is fragile (slowly curing in heat seems to be necessary to set the ceramic) and it contains moisture within its matrix. The ceramic cannot yet be exposed to vacuum or the moisture will damage the matrix (powder the ceramic) on the way out. First the moisture must be slowly driven off with a gradually ramped temperature over the course of 24*hrs*. The heat is am limited to 150°*C* to avoid oxidizing the exposed nichrome wire used in the nozzle heater.

At this point the ceramic is left in a porous state (pores remain due to moisture escape). Sputter is applied over the surface of the ceramic to establish a full seal. The nozzle is moved as directly as possible from the heater to the sputter vacuum such that the heat will minimize re-entry of moisture below the surface of the ceramic.

After the sputter layer, and additional layer of ceramic is applied over the entire seal to provide mechanical protection for the sputter layer. The final layer of Resbond 920

requires an additional 24*hrs* to set. The final ceramic is still fragile and prone to shatter into dust if bumped. To prevent dust contamination into the chamber, glaze seal is applied. Upon firing, this leaves a glass layer over the seal. Even if full temperature is not reached to fire the glass, it still seems to re-enforce the surface layer of the ceramic and prevent dusting.

### A.2 Verification

Although consistency of producing viable nozzles increases with practice, the best yield remains limited to 3 out of 4 attempts. Leaks are first checked for under ambient conditions, then the flow is measured relative to temperature. At ambient conditions, the full pressure expected for experiments is applied to the nozzle and a bead of water is carefully applied to the surface of the ceramic. Dragging the bead over the entire surface will reveal a small stream of bubbles coming from any potential leaks (a jet of bubbles should be observed from the nozzle orifice). Soapy water such as Snoop cannot be used to check for leaks because it dissolves the ceramic. If the nozzle has no leaks, then vacuum is applied and a mass flow is applied such that an appreciable upstream pressure is measured. If the flow restriction is so low that the highest flow rate sustainable in chamber vacuum does not result in a significant upstream pressure, then this validation method will not apply (flat line of flow versus temperature). The initial combination of pressure and mass flow is recorded as the reference point.

For a specified mass flow rate, the parameters determining the upstream pressure are diameter, length, viscosity, temperature, and specific heat. The Buckingham Pi groups are $\mu d/(\mathrm{d}m/\mathrm{d}t)$, $d/L$, and $(\mathrm{d}m/\mathrm{d}t)\ (c_P T)^{1/2}/Pd^2$. Diameter, length, and mass flow rate are all

constants. Specific heat and viscosity may (depending on the gas and temperature range) be approximated as constants. Therefore, the only variables are in the third Pi group which must be a constant. This provides the guide $P \propto (T)^{1/2}$. (For a system with insufficient flow restriction, the proportionality constant is zero.) Sample validations are given in Figures A.1 and A.2.

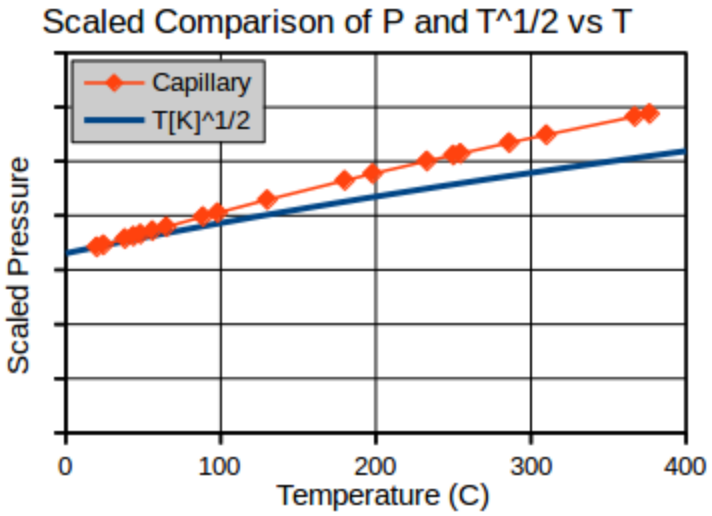


***Figure A.1: Pressure for argon flow 1.00 sccm starting at inlet 0.23 bar (absolute) and 20.1°C is measured against ramping nozzle temperature.***

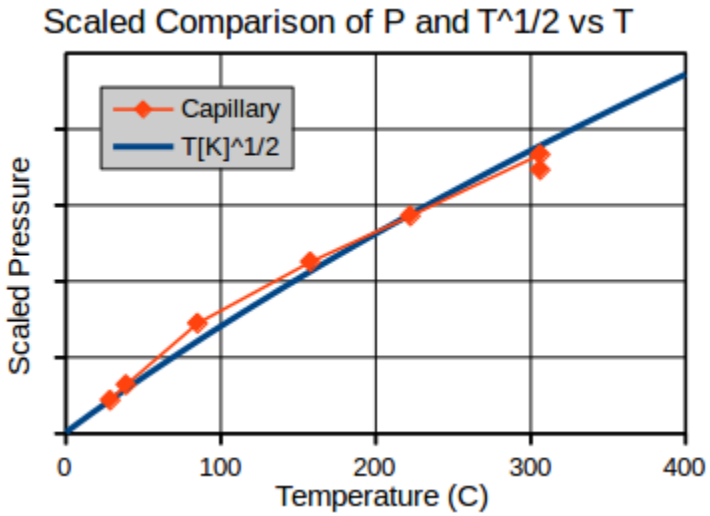


***Figure A.2: Pressure for oxygen flow 1.64 sccm starting at inlet 0.215 bar (absolute) and 28.6°C is measured against ramping nozzle temperature.***

A successful validation should show some relationship between pressure and temperature; however, the exact curve depends on the gas and – by extension – the geometry. Since specific heat typically increases with temperature, and viscosity typically decreases with temperature, there is no universal rule regarding whether the real curve should always be above or always be below the expected curve. If a leak develops while gradually ramping the temperature then the upstream pressure will drop down from the established curve. If a leak develops at any point, then cycling back to the original temperature will result in a lower upstream pressure than was initially uses. Validation requires the ability to measure mass flow rate, upstream pressure, and nozzle temperature.

Finally, since the experimentally requisite maximum pressure was not likely known before validation. A second validation may be performed at which that pressure is exceeded in the operational temperature range. Also, it is essential that the chosen mass flow rate remains in the continuum flow regime even at the maximum temperature.

### A.3 Heaters

In the vacuum chamber, the energy of the heater is dissipated by radiation and by direct conduction along the nozzle mount. Make sure that any delicate components directly attached to the nozzle mount have sufficient thermal resistance between them and the heater such that the desired nozzle temperature will not result in damage. The power source being used to heat the nozzle is limited to 2 A and 25 V. The power delivered is $P = I^2R$. To maximize heating and minimize the thermal time response, the greatest possible length of wire per volume is desired. Typically, nichrome wires of diameter less than 0.4 mm to burn out under typical heating (~300°C) conditions. Nichrome wire is wrapped around a spool (of diameter slightly greater than the metal gas line) with a slight gap between wraps to produce a coil of about 1.5 cm. Paper is wrapped around the first coil to introduce a gap and the wire is wrapped back in the opposite direction. The ends of the wire are folded back and secured to provide loops that are easy for the power line to clip to. The spool is pulled out and the paper is removed by burning.

The coils are then slid onto the metal gas line and aluminum foil is shaped into a bath around the coil. The Resbond 920 is mixed per instructions and added to the bath to completely cover the coils. The components are gently moved and twisted relative to each other to ensure the ceramic settles into every crevice – preventing air pockets and electrical shorts. Additional Resbond should be applied to the base of the nichrome loops to produce reasonably robust stubs to attach wiring clips to. It is found that the position of the heater should within 3 cm of the end of the metal tube, and tubes with thinner walls are preferable. In the case of Swagelok tubes, the thermal resistance is relatively high. The primarily mode of cooling between the heater and the nozzle is radiation, which for a broad temperature

range is negligible. However, with the high thermal resistance along the tube, the radiation can be sufficient to cause a temperature drop towards the end of the tube.

Just as with the nozzle seals, gradual heat-treating up to 150°C should be done to drive off water and set the ceramic. This temperature must not be exceeded in oxygen in order to protect the nichrome wires. Also, as with the nozzle seals, glaze may be applied to the outside of the heater in increase its structural integrity and prevent dusting into the chamber. To set the glaze requires greater temperatures. Higher temperatures may be reached in a vacuum or in an inert gas bath – such as Argon. In either case, the nozzle heater may be used to finish setting the ceramic and the glaze. It is not necessary to reach the full firing temperature of the glaze to still gain some benefit from it. A typical configuration is shown in Figure A.3.

***Figure A.3: A nozzle heater is mounted in typical configuration with a thermocouple and without heat shielding.***

Finally, to protect other components in the vacuum chamber, to minimize power dissipation, and to increase the maximum temperature that can be reached, the heater should be loosely wrapped with layers of aluminum foil. The Resbond stubs around the

base of the nichrome loops (and coated with glaze) prevent the aluminum foil from contacting and shorting out the power lines.

### A.4 Thermocouple

The thermocouple (as shown in Figure A.3) must be mounted close to the end of the metal tube. The abrupt change in diameter (from about 2 mm down to tens of microns) means that the gas is approximately stagnant before passing through the nozzle at high velocity. Therefore, the temperature of the tube at the end is the best indicator of the gas temperature at the inlet of the nozzle. The thermocouple shown was mounted using Resbond each time the setup was configured for use. As discussed, this is a source of aluminum oxide dust into the chamber. Two alternative approaches are apparent: 1) A metallic epoxy may be used to set the thermocouple in place and establish thermal conductance to the nozzle (in the absence of other currents, the thermocouple measurement should not be compromised). 2) The thermocouple, heater, and nozzle mount may be more permanently coupled together as a single component (the mount shown was used for a wide variety of heaters). As such, the Resbond coupling between the thermocouple and the nozzle can receive the same, more permanent, glaze treatment.

In the wiring, it may be necessary to switch to a different material (SEM wall feedthrough wires) from the thermocouple materials before the circuit makes its way back to the readout device. To prevent readout errors, the temperature at the transition of materials must match the temperature at the readout device. For this purpose, a break is introduced in the thermocouple wires. At the break, the thermocouple wires of the same

material clip together. The electrical signal is uninterrupted through the contact; however, the contact introduces a great deal of thermal resistance.

# APPENDIX B. ENHANCED PURITY INVESTIGATION

## B.1 Measuring Volumetric Change of Deposits due to Heating

AFM measurements taken before and after heating are used to calculate the volume changes. Since AFM images represent height with coloring, measuring the volume is a simple matter of integrating the heights of each pixel (deducting the base height) over the area of the deposit. This was complicated by the fact that the gold-palladium layer applied via sputtering to a silicon oxide substrate both ablates and forms nanoparticles when heated. A portion of the gold-palladium layer was gently scraped off to reveal the surface of the silicon oxide substrate such that the thickness of the gold-palladium layer could be measured by AFM before and after heat treatment. The thickness before heating is measured at multiple points as 749*nm* with a standard deviation of 49*nm*. The thickness after heating is 654*nm* with a standard deviation of 26*nm*. The loss of substrate thickness is therefore 95*nm* with a standard deviation of 55*nm*. The gold-palladium layer directly under the deposit is shielded by the deposit and takes on the morphology of the deposit as the rest of the surface is ablated. As a result, the additional pseudo-height of each deposit after heating must be deducted as illustrated in Figure B.1 when calculating volume. The deposit illustrated in this comparison was measured to have a purity of 42% and a volume loss of 16%.

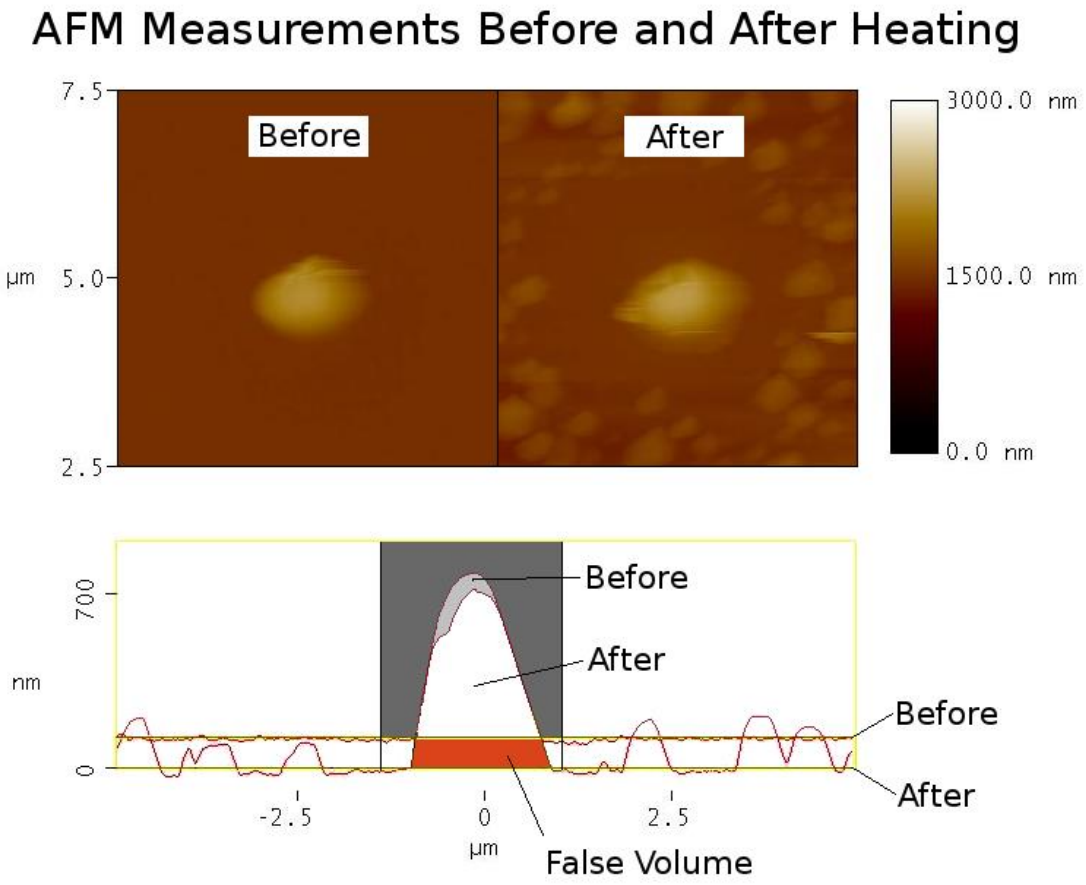


***Figure B.1: Top view AFM measurements compared to cross-sectional view of a deposit before and after heating to 450 °C.***

If the volume of the deposits after heating were calculated using the substrate surface as the baseline, then the false volume added to the deposit illustrated would create the illusion of a 67% volume increase instead of a 16% volume loss. Instead, 95 *nm* is added to the baseline height to all deposits to account for substrate ablation. Because the standard deviation of heights to add is 55*nm*, several different baseline adjustments were used (with the constraint that no deposits could increase in volume after carbon material is removed). All results in Figure B.2 produced the same trend between Knudsen number and percent volume loss. The percent volume loss versus Knudsen number is calculated by taking into

account a range of plausible changes to the baseline substrate height. The observed trend is consistent in all cases.

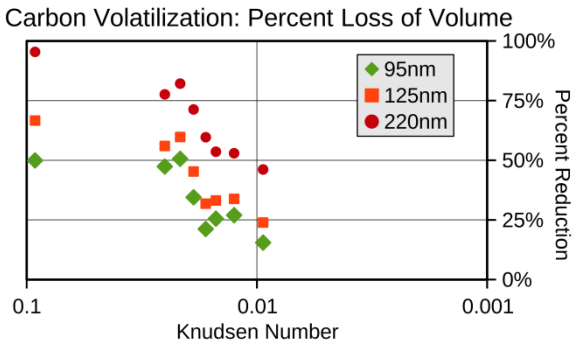


***Figure B.2: The percent volume loss versus Knudsen number.***

The volumetric reduction experiment was also performed on the silicon dioxide substrate which is not susceptible to surface loss. The tilted SEM images in Figure B.3 qualitatively indicate that less volume is lost at the lowest Knudsen number. The deposits were to $450°C$ for $20min$, and each image is labeled with the AFM measurement of its maximum height. Images suggest less volume change at lower Knudsen number.

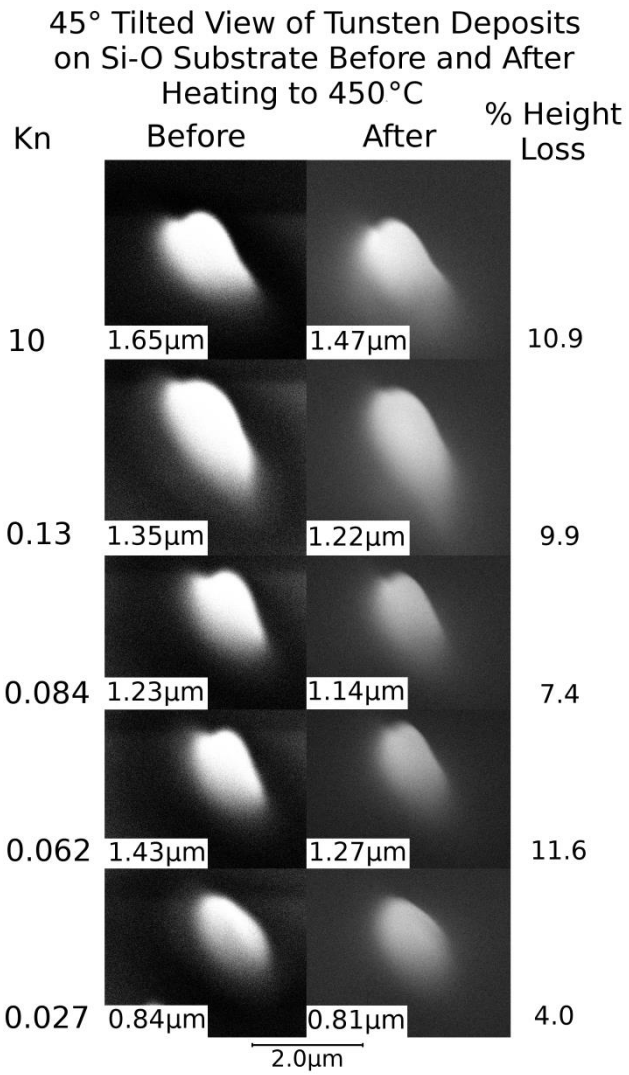


***Figure B.3: SEM deposit cross-sections on Si-O substrate tilted at 45° before and after heating.***

### B.2 Consistency of Deposit Growth Relative to Position under the Nozzle

The flux and velocity of the argon gas jet depends on impingement location relative to the nozzle. For consistency of experiments, great care was taken to keep the deposition location consistently 20$\mu m$ along the nozzle centerline away from the top edge. Simulations show that in this region there is relatively little variation of flux and impingement velocity. To test for potential alignment error and impact on the repeatability of deposition outcomes,

three deposits were grown under identical conditions but in slightly differing locations surrounding the target deposition zone. Three deposits grown for 2*min* each at varying locations relative to the nozzle, indicated in Figure B.4, with a 75$\mu m$ ID nozzle, an argon carrier gas, and the Knudsen number 0.0083. The tip of the nozzle is shown in the lower-left corner. The deposit (2) was made 20$\mu m$ further from the 75$\mu m$ inner diameter (ID) nozzle and (3) was made 20$\mu m$ to the side (relative to the target deposition spot marked as (1). No variation is observed in the morphology of the deposits. Figure B.5 shows that the EDS measurement of tungsten to carbon do not vary between these deposits, and the results are consistent with previous measurements at the same conditions reported in Chapter 3.

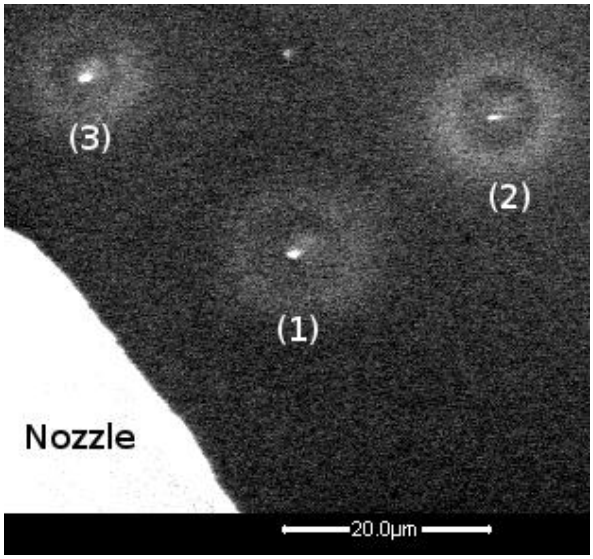


***Figure B.4: Deposits of slight variation of location relative to the nozzle indicate the consistency of growth.***

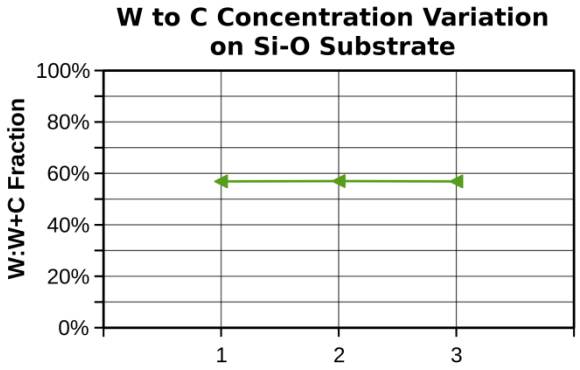


***Figure B.5: EDX measurements of three identically grown deposits with a varying spatial position relative to the nozzle.***

### B.3 Negligible Effect of Surface Heating

Surface heating by impinging gas jet is considered as a possible mechanism to assist in ligand removal during deposition. To investigate the thermal effect of the argon gas jet interacting with the substrate, a platinum RTD was microfabricated onto a glass substrate of low thermal conductivity to minimize heat loss through the substrate. The RTD fabrication process, calibration, and application for microscale temperature measurements follows an approach established by Narayanan, et al [112]. Figure B.6 presents SEM images of the RTD sensing element (seen as a zig-zagged line connected to the square pad) in different positions relative to the 75$\mu m$ ID nozzle. Those positions define the position axis of Figure B.7 where temperature measurements have been performed. The thermal response of a point on the substrate relative to nozzle position is presented in Figure B.7 for both an unheated nozzle and for the nozzle heated to the inlet temperature of 205$°C$. As the results indicate, the gas jet heating effect on the substrate is negligible, thus supporting the exclusion of the thermally-induced contaminant desorption from the possible mechanisms of enhanced purity.

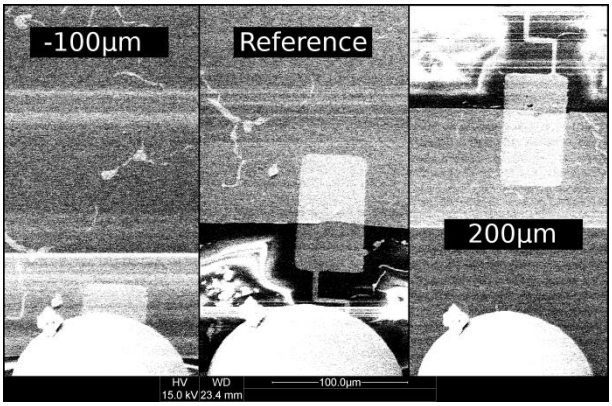


***Figure B.6: Positioning the resistance temperature detector relative to the 75 µm ID nozzle.***

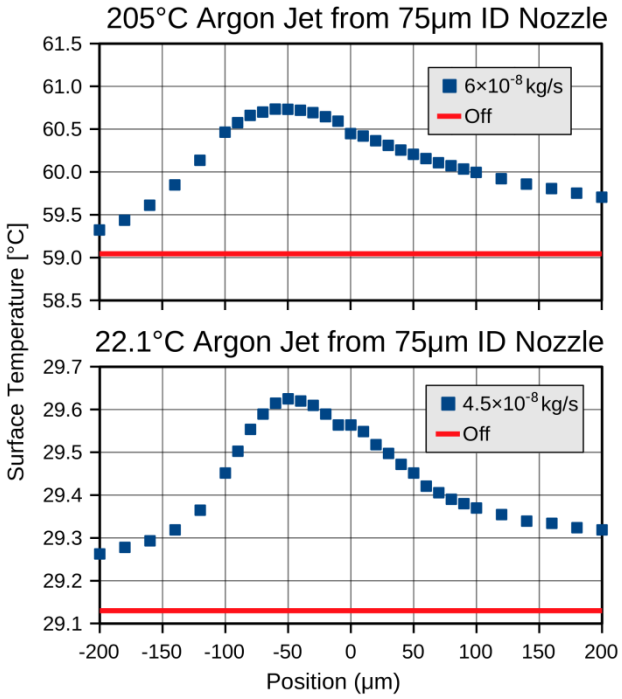


***Figure B.7: Thermal response of the substrate over a range of positions relative to the nozzle for the relevant range of mass flow rates used in FEBID experiments. The heated and unheated Argon jet Knudsen numbers are 0.024 and 0.025, respectively.***

## B.4 Decomposition Temperature of Tungsten Hexacarbonyl

The decomposition rate of tungsten hexacarbonyl is approximated by the Arrhenius equation with constants determined by the environment composition. Figure B.8 plots are

based on data for an argon environment at various temperatures as adopted from reference [64]. For a 24 hour period, the effective decomposition temperature is 240°*C*.

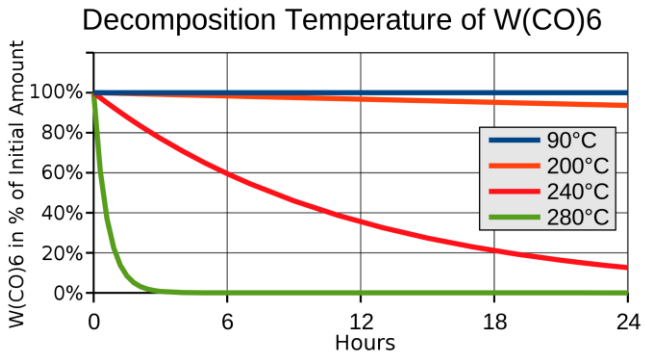


***Figure B.8: Decay curves for tungsten hexacarbonyl over the course of a 24 hour period, starting at 100% amount.***

# APPENDIX C. ADAPTIVE DSMC ALGORITHM

## C.1 Statistical Error of Particle Cloning Versus Particle Seeding

The particle seeding method in the adaptive DSMC algorithm addresses the development of statistical error inherent in particle cloning when a simulated gas flow undergoes significant expansion. A sample 1D scenario is illustrated in Figure C.1 in which an argon gas jet is introduced at 40$Pa$, 200$K$, 300 $m/s$, and $Mach$ 1.14 then exits to vacuum at 100$\mu m$. The first five rows of cells (1$\mu m^3$ each*)* along the flow axis are assigned the weighting factor of 1024. A drop in weighting factor is imposed upon each subsequent row of cells, as shown in Figure C.1.b, until the eleventh position. The velocity distribution of this cell is sampled for 1000 particles for velocities normal to the mean flow velocity, and the particle cloning and particle seeding methods are compared in Figure C.1.c with the expected Gaussian distribution for argon gas at 191$K$. In principle, the DSMC algorithm is not designed to capture the true velocity distribution of gas particles, but rather to discretize it with an adequate number of simulation particles. However, when a particle's velocity is duplicated in particle cloning, its particular velocity becomes over-represented and the velocity distribution becomes artificially distorted for the given number of particles. Particle seeding averts this problem by introducing velocity information spawned from the local cell temperature and mean velocity. The distribution discretization generated by particle seeding in Figure C.1.c is consistent with the true discretization, based on local temperature and average velocity that must occur for 1000 random particles. Since the local cell properties in this case are determined equally from upstream information and old information (due to seeding), the particle statistics will converge towards the true cell properties.

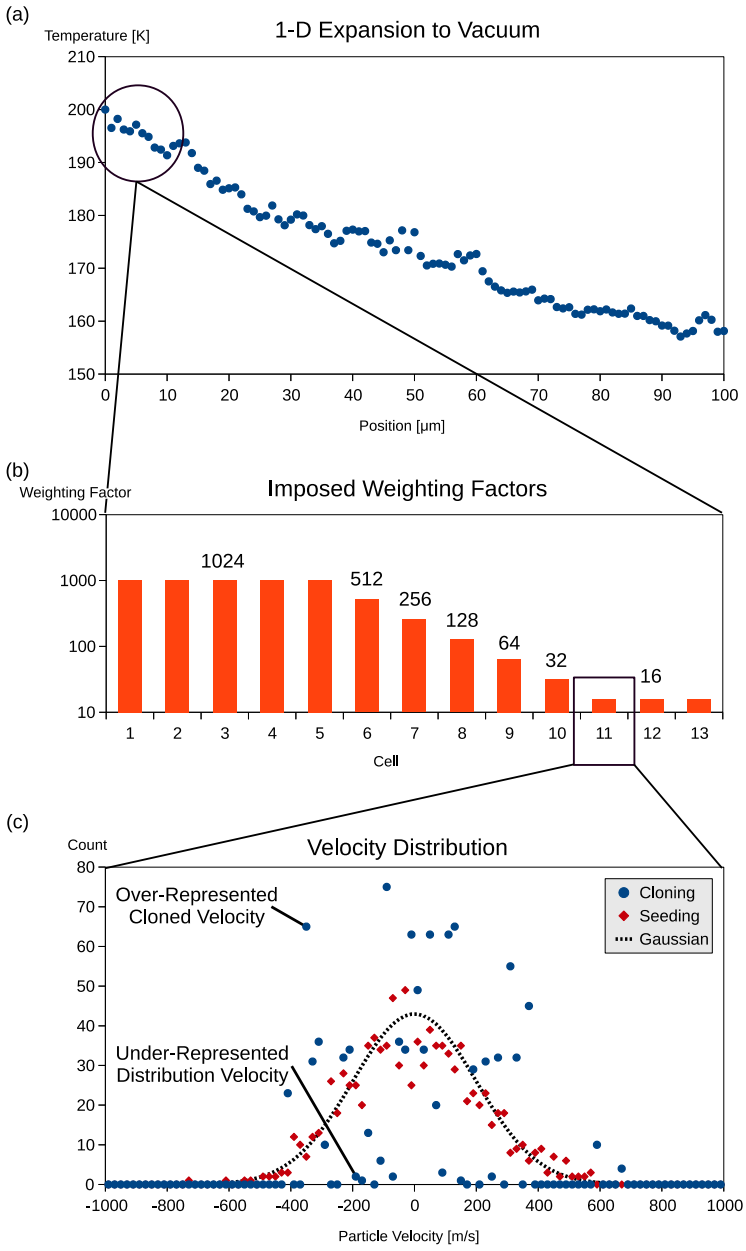


***Figure C.1: (a) A 1D argon gas isentropically expands from inlet conditions to an imposed vacuum at 100μm. (b) Weighting factors are imposed to produce a controlled particle-splitting scenario. (c) Histograms of 1000 sampled particles from each flow (cloning and seeding) show that particle seeding significantly superior in capturing the Gaussian velocity distribution.***

### C.2 Material Conservation in Adaptive DSMC Algorithm

Fundamentally, DSMC algorithms that accommodate variations in density with varying weighting factors cannot strictly conserve mass, energy, or momentum. In the case of the adaptive DSMC algorithm, each cell neighboring another with a lower weighting factor monitors whether the previous incoming particle was deleted or doubled in mass and alternates this action for each subsequent particle; thus, the conservation of mass is strictly enforced. However, energy and momentum both have an equal probability of being either increased or decreased in a random walk fashion. In the atypical case of adiabatic, isolated flow involving multiple weighting factors, it is possible for conservation errors to accumulate. To validate that any statistical errors are non-biased, total system momentum and energy are monitored, as shown in Figure C.2.a and b for periodic flow of oxygen gas at 40$Pa$, 300$K$, and 50 $m/s$ in the lengthwise direction. The domain consists of 40×10×10 cells of one cubic micrometer in volume each, and a lower weighting factor is imposed upon cell positions from 10 through 30, such that the gas flow continuously causes the simulation particle splitting and a merging event.

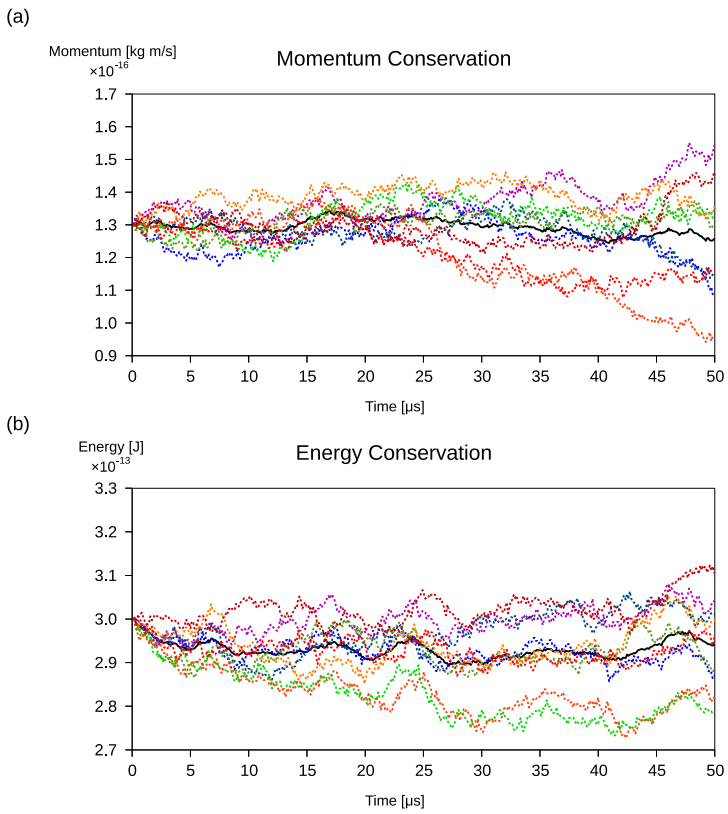


***Figure C.2: 1D periodic flow of oxygen in a channel. The random walk of (a) total momentum in the lengthwise direction and (b) total energy over an entire simulation domain are monitored for nine identical simulations to validate that the necessary conservation error is not biased. The average of all simulations is indicated in black, showing excellent conservation of momentum and energy after averaging over multiple independent statistical realizations.***

## C.3 Viscosity Variation with Temperature in Hard Sphere Model

Each simulation presented uses the hard sphere model with the Van der Waals diameter $D = [3k_B T_{cr}/4\pi P_{cr}]^{1/3}$, where $k_B$ is the Boltzmann constant, $T_{cr}$ is the gas critical temperature, and $P_{cr}$ is the gas critical pressure. The hard sphere model is validated for the continuum flow regime in Figure C.3.a using Couette flow with a gap size of $H$=1$m$, wall velocity $U_{Wall}$=100 $m/s$, and argon gas at 0.4$Pa$. Three simulations cases are presented with wall temperatures of $T_{Wall}$=100$K$, 200$K$, and 273$K$, corresponding to Knudsen numbers 0.004, 0.007, and 0.01. The expected temperature profiles are analytically

determined from Equation 4.7, accounting for volumetric heat generation due to viscous heat dissipation. Since variation of thermal conductivity with temperature is nearly identical to that of viscosity, the differential temperature profile (relative to the prescribed wall temperature) is indistinguishable for each simulation case.

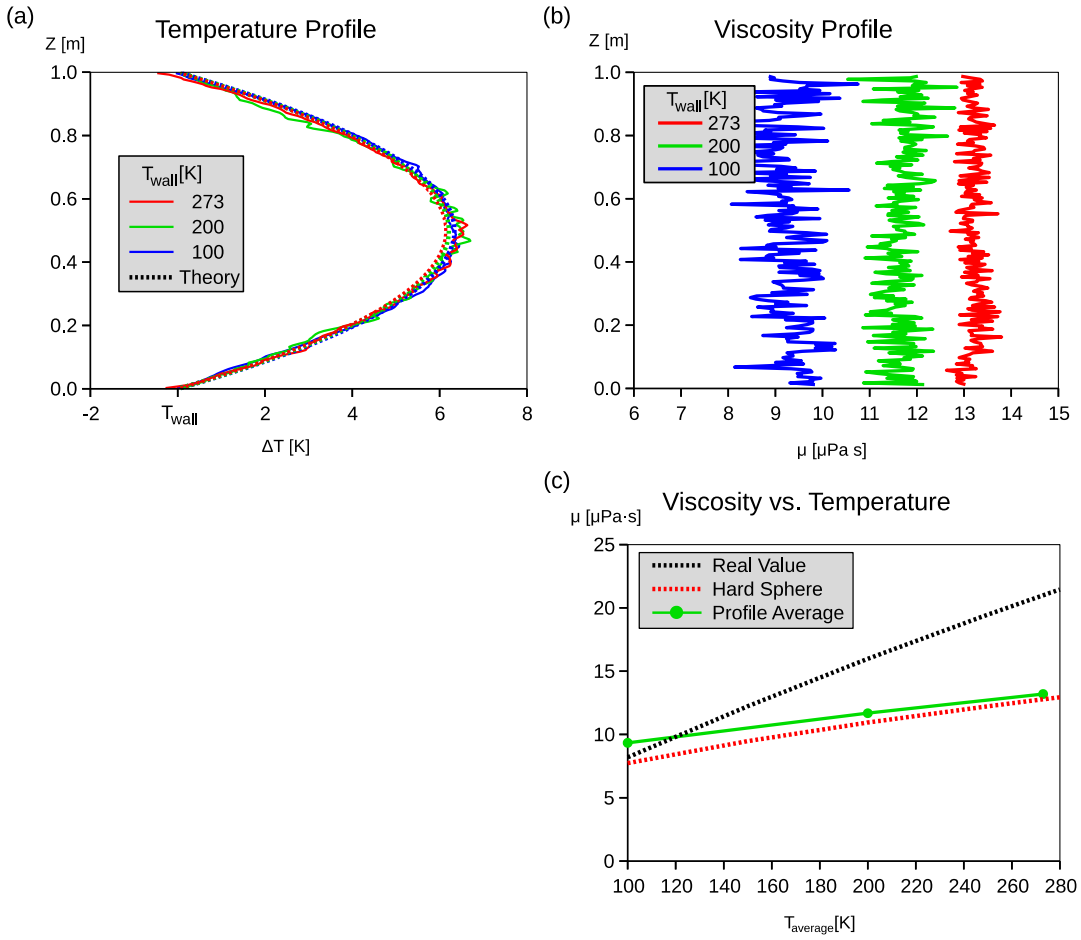


***Figure C.3: (a) The temperature profile realized in Couette flow with viscous heat dissipation is used to validate the hard sphere collision model. (b) Viscosity profiles across the channel show an expected increase with an average gas temperature with little cross sectional variation. (c) Viscosity values obtained via DSMC are plotted against temperature along with the expected trend of the hard sphere model and the real viscosity values.***

The viscosity of an individual cell that is subject to shear stress along the vertical z-axis only can be calculated by Equation C.1, in which $m_P$ is the mass of a particle, $N$ is the number of simulation particles in the cell, $u$ and $v$ are the particle velocities on the horizontal axis, $\forall$ is the volume of the cell, and $dU/dz$ is the vertical z-gradient of mean velocity [72]. This is used to calculate the viscosity profiles of Figure C.3.b.

$$\mu = m_P \frac{\sum^N uv}{\forall} \frac{dz}{dU} \tag{C.1}$$

The hard sphere model predicts the viscosity relationship with temperature indicated in Equation C.2 [72], which does not fully capture the real variation of viscosity with temperature. The average viscosity values obtained for each wall temperature in Figure C3.b are consistent in Figure C.3.c with the expected values for the hard sphere model, but deviate from the real viscosity values at higher temperatures.

$$\mu = \frac{5}{16D^2}\left(\frac{k_B T m_P}{\pi}\right)^{1/2} \tag{C.2}$$

The hard sphere model is adequate for lower temperatures, and the hard-sphere viscosity becomes inaccurate only at higher temperatures. The case study of free expansion of an argon gas jet into vacuum (Figures 4.4 through 4.6) validates the use of the hard sphere model for all temperatures below $220K$. In gas jet applications relevant to this thesis work, the temperate only exceeds this limit in the surface region in the gas stagnation pocket. The viscosity in this region can deviate from the expected viscosity by a factor of almost two. This is readily addressed by basing the hard sphere diameter on the local cell

temperature according to Equation C.3, where $T_{cell}$ is the local cell temperature, and $\mu(T_{cell})$ is the known relationship between viscosity and temperature [113].

$$D = \left[\frac{5\sqrt{m_P T_{cell}\, k_B/\pi}}{16\mu(T_{cell})}\right] \tag{C.3}$$

### C.4 Configuration Information for Each Simulation

For each simulation, Table C.1 provides the configuration information and Figure C.4 indicates the distribution of the inverse mean-free-path. The sampling interval is the number of time-steps evolved between the collection of samples in order to avoid double-sampling of identical states. Samples are procured until a minimum threshold of simulation particles is obtained. The approximate number of samples for evaluation of local properties is based on the minimum threshold and the target population of simulation particles per sub-cell. Local properties are recorded with the sampling weight $\alpha$ for the new value and (1-$\alpha$) for the old value to stabilize steady-state predictions.

***Table C.1: Simulation Configuration Details***

| | Argon Plug Jet | | Shear Flow | Complex Flow |
|---|---|---|---|---|
| | Kn=0.1 | Kn=0.01 | | |
| Time Step [$s$] | $4.37\times10^{-11}$ | $1.72\times10^{-10}$ | $2.97\times10^{-7}$ | $9.10\times10^{-11}$ |
| Cell Dimension [$m$] | $5\times10^{-7}$ | $3\times10^{-7}$ | $2.5\times10^{-3}$ | $1\times10^{-6}$ |
| Domain | 300x80x80 [$\mu m$] | | 1x0.015x1 [$m$] | 251x91x251 [$\mu m$] |
| Cells | 1,968,300 | 8,978,000 | 240,000 | 5,733,091 |
| Simulation-Particles | 30,281,000 | 137,217,000 | 418,000 | 56,341,000 |
| Real-Particles | $4.87\times10^{9}$ | $5.66\times10^{9}$ | $7.85\times10^{17}$ | $9.53\times10^{11}$ |
| Sampling Interval | 5 | 5 | 15 | 5 |
| Samples per Evaluation | 4 | 4 | 5 | 4 |
| Sampling Weight ($\alpha$) | 0.08 | 0.6 | 0.05 | 0.7 |

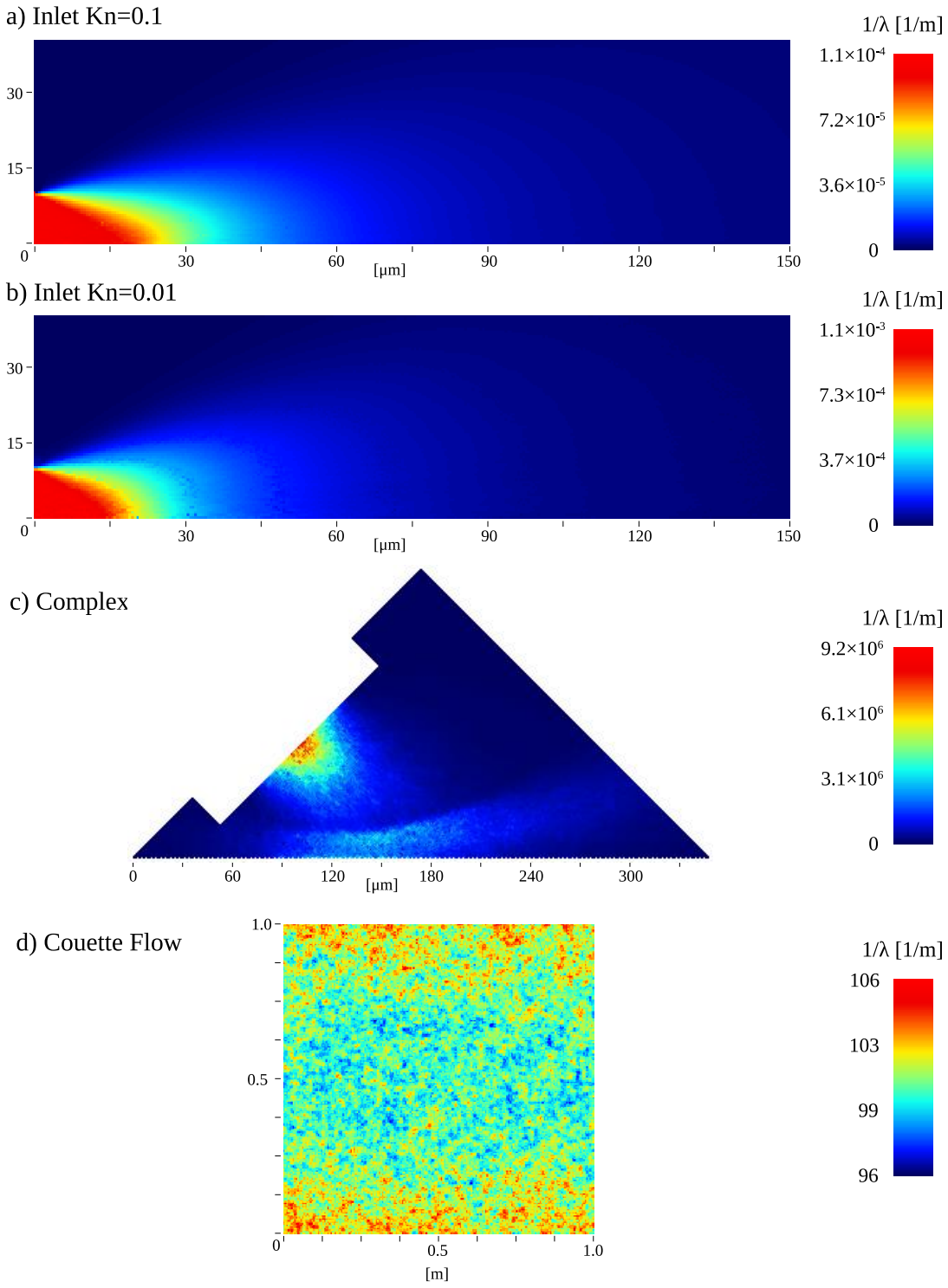


***Figure C.4: The local distribution of the inverse of the mean free path, when compared to the cell dimension, is indicative of the mean particle collision distance throughout the domain.***

### C.5 Conservation Assessment for Each Simulation

In Figure C.5, the location of the local observation box is indicated for each simulation. Mass and energy conservation data for the local observation box and total domain is reported in Table C.2. The sampling interval is the number of time-steps evolved between the collection of samples in order to avoid double-sampling of identical states. Samples are procured until a minimum threshold of simulation particles are obtained. The approximate number samples collected for each results evaluation is based on minimum threshold and the target population of simulation particles per sub-cell. In the case of the complex flow simulation, diffuse energy exchange with the substrate is accounted for in the difference between energy flowing into and out of the domain.

***Table C.2: Mass and Energy Conservation***

| | Argon Plug Jet | | Shear Flow | Complex Flow |
|---|---|---|---|---|
| | Kn=0.1 | Kn=0.01 | | |
| Sampling Time [s] | $1.73\times10^{-8}$ | $3.81\times10^{-8}$ | $1.33\times10^{-4}$ | $4.19\times10^{-9}$ |
| Domain Percent Differences | | | | |
| Energy | 3.1% | 3.1% | N/A | 8.05% |
| Mass | 0.33% | 1.7% | N/A | 1.8% |
| Local Sample Box Percent Differences | | | | |
| Sample Box [μm] | 20x10x10 [μm] | | 0.2x0.2 [m] | 30x50x50 [μm] |
| Energy | 0.95% | 0.35% | 0.42% | 12.0% |
| Mass | 0.70% | 0.50% | 0.33% | 11.9% |

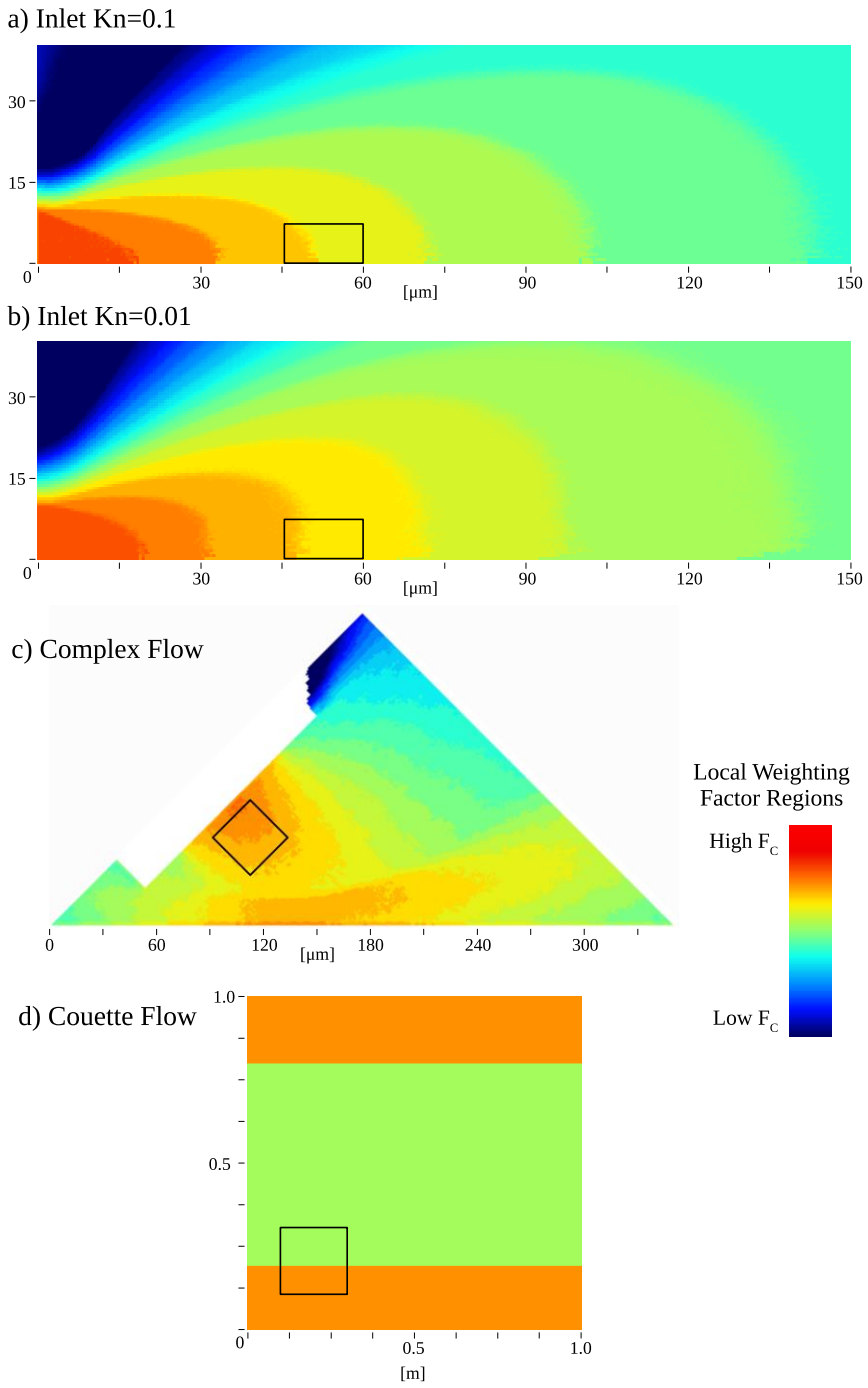


***Figure C.5: Local observation boxes are assigned to each simulation to verify local conservation of mass and energy.***

## C.6 Implementing Appropriate Non-Adiabatic Diffuse Boundary Surfaces in Direct Simulation Monte Carlo

In Figure C.6, three implementations of a non-adiabatic diffuse surface are compared for static argon gas bounded at the top and bottom by non-adiabatic diffuse walls maintained at 273 $K$. When a particle interacts with a non-adiabatic diffuse surface, it is expected to rebound from the wall in a direction randomly selected with a velocity statistically selected from the wall temperature. For the two axes tangent to the surface, the velocities are selected from the Gaussian distribution $f(V)$. In order to maintain the diffuse distribution of directions, the velocity along the orthogonal axis must also be $f(V)$. The orthogonal velocity distribution of a gas impinging upon the surface, that is in thermal equilibrium with the surface, is $g(V)=V f(V)$. Therefore, the energy delivered to the surface following the $g(V)$ distribution is greater than the energy of particles rebounded from the surface that follow the $f(V)$ distribution. As a result, the Diffuse surface simulated for Figure C.6, cools the simulated gas, which is a numerical artifact with no physical significance.

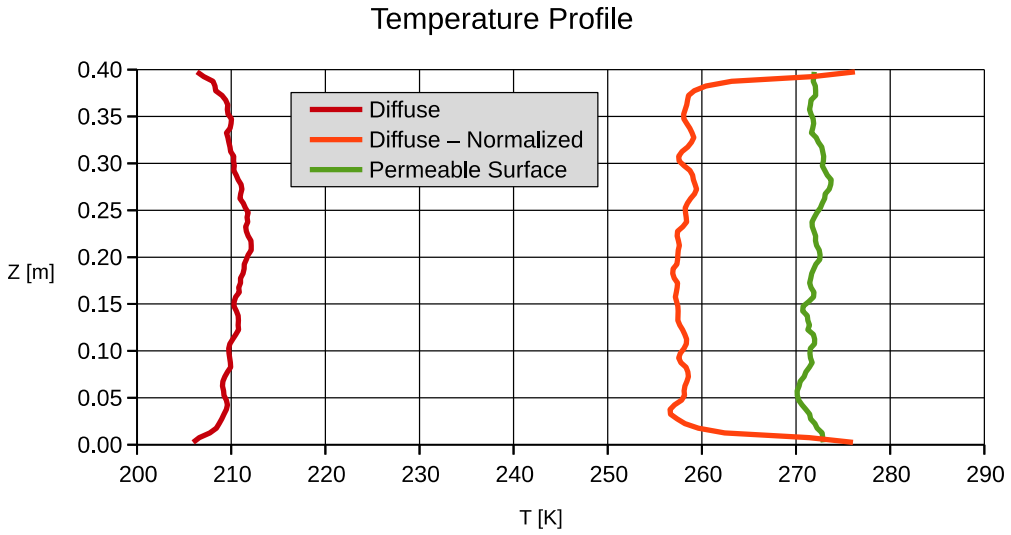


***Figure C.6: Three implementations of a non-adiabatic diffuse surface are simulated to identify the appropriate model for DSMC. The Diffuse surface chooses velocity components from the Gaussian distribution on all three axis - 3×f(V). The Diffuse-Normalized surface takes the energy from 2×f(V)+1×V f(V) and applies it in the direction of 3×f(V). The Permeable Surface uses the velocity and direction from 2×f(V)+1×V f(V).***

To equalize the impinging and rebounding particle energies for a gas in thermal equilibrium with the wall, the particle velocity may be determined by selecting two $f(V)$ velocities and one $g(V)$ velocity, then applying that velocity to a diffuse direction. This method takes energy of particles that are arriving to the wall primarily in the orthogonal direction and redirects it towards the tangential axis. As a result, the Diffuse-Normalized surface simulated in Figure C.6 yields a temperature spike at the walls and drop in the center, which is unphysical.

To obtain the physically meaningful result, the $f(V)$ distribution needs to be used along the tangential axes and the $g(V)$ distribution needs to be used along the orthogonal to the wall axis. This method does effect a no-slip surface condition, but it does not strictly

represent a diffuse surface. This is functionally analogous to the Permeable Surface where the other side of the boundary is a static argon gas at the specified temperature.

## APPENDIX D. ACTIVE CONTROL OF ADATOM TEMPERATURE

An RTD was fabricated on borosilicate glass with dimensions 20$\mu m$ by 20$\mu m$, using depositions patterns of 10$nm$ chromium, 35$nm$ platinum, and finally a thin layer (~10$nm$) of silicon dioxide. The RTD response was calibrated in a temperature controlled oven to be 2.393 $K/k\Omega$. Used in conjunction with a picoammeter, the RTD has a resolution uncertainty of 0.002$K$. The RTD substrate is mounted to a nano-scale positioning table in an SEM vacuum chamber. Temperature measurements were collected *via* RTD from a gas jet nozzle mounted at a 45° tilt from the surface normal and the 138$\mu m$ outer diameter edge is offset 20$\mu m$ above the substrate. Gas jets exit the 75$\mu m$ inner diameter nozzle in the upward direction relative to Figures D.1 through D.3, which report the full 2D surface maps of the RTD measurements collected for argon gas jets at the flow rates 4.3 and 7.0 *sccm* and an oxygen gas jet of 7.3 *sccm*. The surface region compared to DSMC-hard-cube model predictions is outlined in each figure.

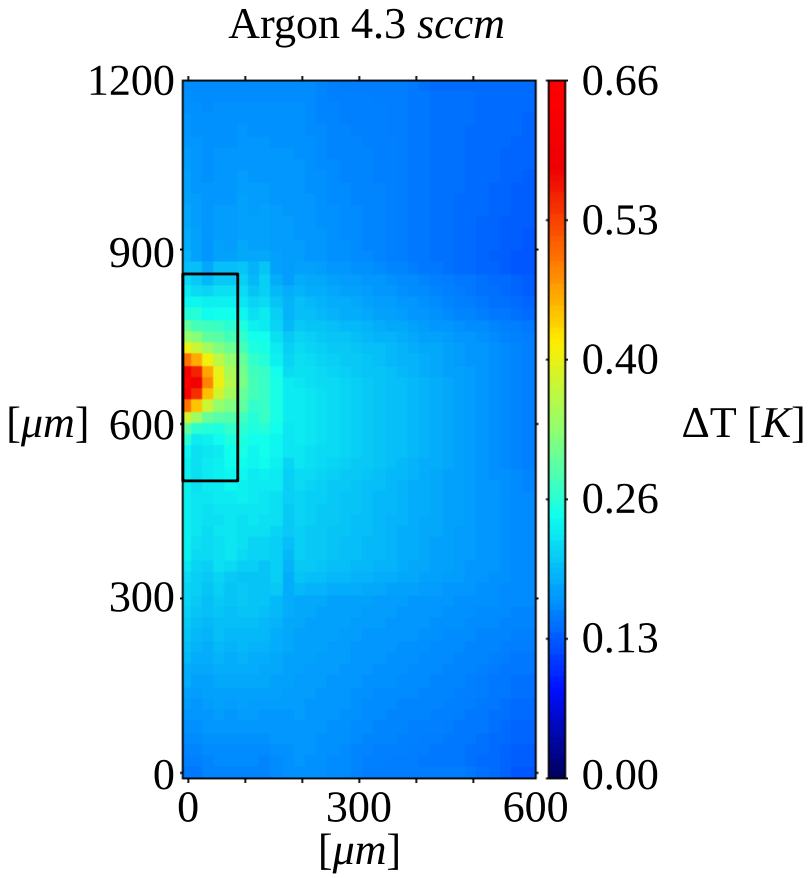


***Figure D.1: RTD measurements of the surface thermal response is collected for an argon gas jet at the flow rate of 4.3 ± 0.14 sccm. RTD temperature measurement uncertainty is ± 0.002K.***

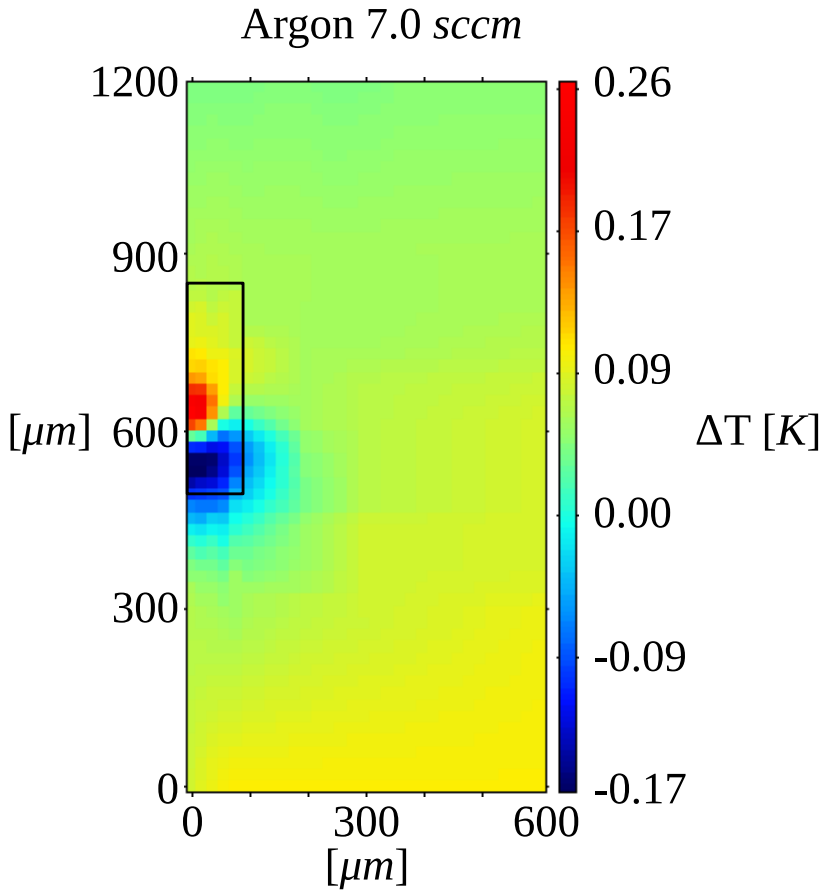


***Figure D.2: RTD measurements of the surface thermal response is collected for an argon gas jet at the flow rate of 7.0 ± 0.14 sccm. RTD temperature measurement uncertainty is ± 0.002K.***

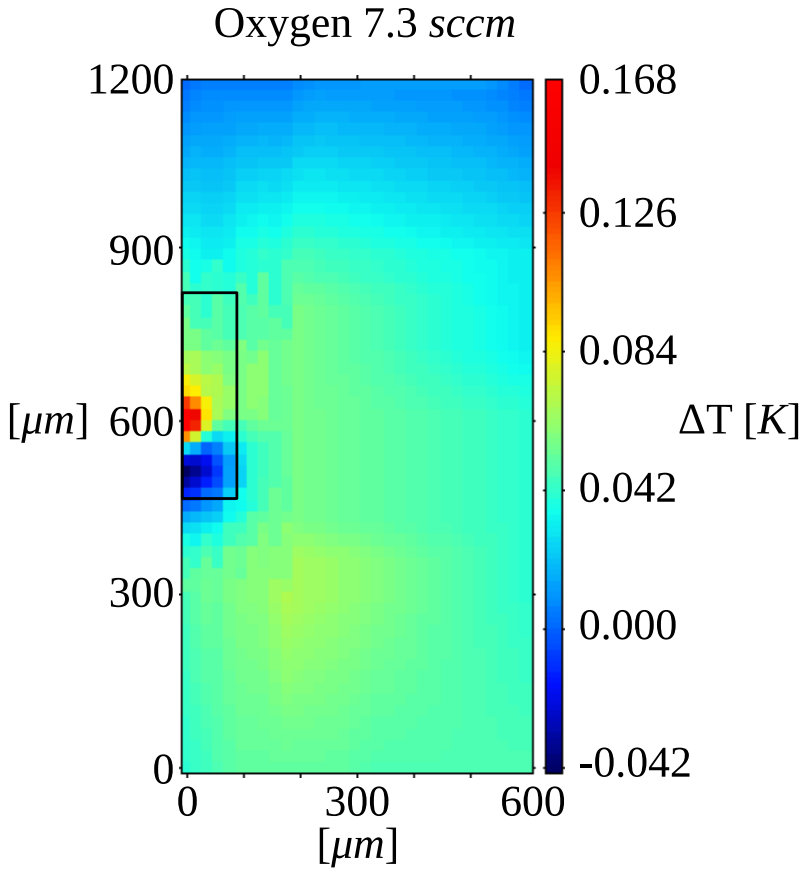


***Figure D.3: RTD measurements of the surface thermal response is collected for an oxygen gas jet at the flow rate of 7.3 ± 0.1 sccm. RTD temperature measurement uncertainty is ± 0.002K.***

## REFERENCES


[1] Gavagnin, M.; Wanzenboeck, H. D.; Wachter, S.; Shawrav, M. M.; Persson, A.; Gunnarsson, K.; Svedlindh, P.; Stöger-Pollach, M.; Bertagnolli, E.; Free-Standing Magnetic Nanopillars for 3D Nanomagnet Logic. *American Chemical Society Applied Materials & Interfaces*. **6**, 20254-20260 (2014).

[2] Makise, K.; Mitsuishi, K.; Shimojo, M.; Shinozaki, B.; Microstructural Analysis and Transport Properties of MoO and MoC Nanostructures Prepared by Focused Electron Beam-Induced Deposition. *Scientific Reports*. **4**, 5740 (2014).

[3] Winhold, M.; Weirich, P. M.; Schwalb, C. H.; Huth, M.; Superconductivity and Metallic Behavior in PbxCyOδ Structures Prepared by Focused Electron Beam Induced Deposition. *Applied Physics Letters*. **105**, 162603 (2014).

[4] Sengupta, S.; Li, C.; Baumier, C.; Kasumov, A.; Guéron, S.; Bouchiat, H.; Fortuna, F.; Superconducting Nanowires by Electron-Beam-Induced Deposition. *Applied Physics Letters*. **106**, 042601 (2015).

[5] Huth, M.; Granular Metals: From Electronic Correlations to Strain-Sensing Applications. *Journal of Applied Physics*. **107**, 113709 (2010).

[6] Che, R. C.; Takeguchi, M.; Shimojo, M.; Zhang, W.; Furuya, K.; Fabrication and Electron Holography Characterization of FePt Alloy Nanorods, *Applied Physics Letters*. **87**, 223109 (2005).

[7] Winhold, M.; Schwalb, C. H.; Porrati, F.; Sachser, R.; Frangakis, A. S.; Kämpken, B.; Terfort, A.; Auner, N.; Huth, M.; Binary Pt-Si Nanostructures Prepared by Focused

Electron-Beam-Induced Deposition, *American Chemical Society Nano*. **5**, 9675–9681 (2011).

[8] Porrati, F.; Kämpken, B.; Terfort, A.; Huth, M.; Fabrication and Electrical Transport Properties of Binary Co-Si Nanostructures Prepared by Focused Electron Beam-Induced Deposition. *Journal of Applied Physics*. **113**, 053707 (2013).

[9] Porrati, F.; Begun, E.; Winhold, M.; Schwalb, C. H.; Sachser, R.; Frangakis, A. S.; Huth, M.; Room Temperature L10 Phase Transformation In Binary CoPt Nanostructures Prepared by Focused-Electron-Beam-Induced Deposition, *Nanotechnology*. **23**, 185702 (2012).

[10] Shawrav, M. M.; Belić, D.; Gavagnin, M.; Wachter, S.; Schinnerl, M.; Wanzenboeck, H. D.; Bertagnolli, E.; Electron Beam-Induced CVD of Nanoalloys for Nanoelectronics. *Chemical Vapor Deposition*. **20**, 251–257 (2014).

[11] Porrati, F.; Sachser, R.; Gazzadi, G. C.; Frabboni, S.; Huth, M.; Alloy Multilayers and Heusler Nanostructures by Direct-Write Approach. *Nanotechnology*. **28**, 415302 (2017).

[12] Porrati, F.; Sachser, R.; Gazzadi, G. C.; Frabboni, S.; Huth, M.; Fabrication of FeSi and Fe3Si Compounds by Electron Beam Induced Mixing of [Fe/Si]2 and [Fe3/Si]2 Multilayers Grown by Focused Electron Beam Induced Deposition. *Journal of Applied Physics*. **119**, 234306 (2016).

[13] Utke, I.; Hoffmann, P.; and Melngailis, J.; Gas-Assisted Focused Electron Beam and Ion Beam Processing and Fabrication. *Journal of Vacuum Science & Technology B*. **26**, 1197-1276 (2008).

[14] Bresin, M.; Thiel, B. L.; Toth, M.; Dunn, K. A.; Focused Electron Beam-Induced Deposition at Cryogenic Temperatures. *Journal of Materials Research*. **26**, 357–364 (2011).

[15] Bresin, M.; Toth, M.; Dunn, K. A.; Direct-Write 3D Nanolithography at Cryogenic Temperatures. *Nanotechnology*. **24**, 035301 (2013).

[16] Fisher, J. S.; Kottke, P. A.; Kim, S.; Fedorov, A. G.; Rapid Electron Beam Writing of Topologically Complex 3D Nanostructures Using Liquid Phase Precursor. *Nano Letters*. **15**, 8385-8391 (2015).

[17] Bresin, M.; Chamberlain, A.; Donev, E. U.; Samantaray, C. B.; Schardien, G. S.; Hastings, J. T.; Electron-Beam-Induced Deposition of Bimetallic Nanostructures from Bulk Liquids. *Angewandte Chemie International Edition*. **125**, 8162–8165 (2013).

[18] Botman, A.; Mulders, J. J. L.; Hagen, C. W.; Creating Pure Nanostructures from Electron-Beam-Induced Deposition Using Purification Techniques: A Technology Perspective. *Nanotechnology*. **20**, 372001 (2009).

[19] Plank, H,; Noh, J. H.; Fowlkes, J. D.; Lester, K.; Lewis, B. B.; Rack, P. D.; Electron-Beam-Assisted Oxygen Purification at Low Temperatures for Electron-Beam-

Induced Pt Deposits: Towards Pure and High-Fidelity Nanostructures. *American Chemical Society Applied Materials & Interfaces*. **6**, 1018-1024 (2014).

[20] Geier, B.; Gspan, C.; Winkler, R.; Schmied, R.; Fowlkes, J.; Fitzek, H.; Rauch, S.; Rattenberger, J.; Rack, P. D.; Plank, H.; Rapid and Highly Compact Purification for Focused Electron Beam Induced Deposits: A Low Temperature Approach Using Electron Stimulated H2O Reactions, *The Journal of Physical Chemistry C*. **118**, 14009–14016 (2014).

[21] Mehendale, S.; Mulders, J. J. L.; Trompenaars, P. H. F.; A New Sequential EBID Process for the Creation of Pure Pt Structures from MeCpPtMe3. *Nanotechnology*. **24**, 145303 (2013).

[22] Lewis, B. B.; Stanford, M. G.; Fowlkes, J. D.; Lester, K.; Plank, H.; Rack, P. D.; Electron-Stimulated Purification of Platinum Nanostructures Grown via Focused Electron Beam Induced Deposition. *Beilstein Journal of Nanotechnology*. **6**, 907–918 (2015).

[23] Winkler, R.; Schmidt, F. P.; Haselmann, U.; Fowlkes, J. D.; Lewis, B. B.; Kothleitner, G.; Rack, P. D.; Plank, H.; Direct-Write 3D Nanoprinting of Plasmonic Structures. *American Chemical Society Applied Materials & Interfaces*. **9**, 8233–8240 (2017).

[24] Roberts, N. A.; Fowlkes, J. D.; Magela, G. A.; Rack, P. D.; Enhanced Material Purity And Resolution Via Synchronized Laser Assisted Electron Beam Induced Deposition Of Platinum. *Nanoscale*. **5**, 408 (2012).

[25] Roberts, N. A.; Gonzalez, C. M.; Fowlkes, J. D.; Rack, P. D.; Enhanced by-Product Desorption via Laser Assisted Electron Beam Induced Deposition of $W(CO)_6$ with Improved Conductivity and Resolution. *Nanotechnology*. **24**, 415301 (2013).

[26] Villamor, E.; Casanova, F.; Trompenaars, P. H. F.; Mulders, J. J. L.; Embedded Purification for Electron Beam Induced Pt Deposition Using MeCpPtMe3. *Nanotechnology*. **26**, 095303 (2015).

[27] Joy, D. C.; An Introduction to Monte Carlo Simulations. *Scanning Microscopy*. **5**, 329–337 (1991).

[28] Kolasinski, K.; Surface Science – Foundations of Catalysis and Nanoscience. *Chichester; Wiley.* (2002).

[29] Fowlkes, J. D.; Rack, P. D.; Fundamental Electron-Precursor-Solid Interactions Derived from Time-Dependent Electron-Beam-Induced Deposition Simulations and Experiments. *American Chemical Society Nano*. **4**, 1619-1629 (2010).

[30] Toth, M.; Lobo, C.; Friedli, V.; Szkudlarek, A.; Utke, I.; Continuum Models of Focused Electron Beam Induced Processing. *Beilstein Journal of Nanotechnology*. **6**, 1518–1540 (2015).

[31] Bishop, J.; Lobo, C. J.; Martin, A.; Ford, M.; Phillips, M.; Toth, M.; Role of Activated Chemisorption in Gas-Mediated Electron Beam Induced Deposition, Physical Review Letters. **109**, 146103 (2012).

[32] Smith, D. A.; Fowlkes, J. D.; Rack, P. D.; A Nanoscale Three-Dimensional Monte Carlo Simulation of Electron-Beam-Induced Deposition with Gas Dynamics. *Nanotechnology*. **18**, 265308 (2007).

[33] Fowlkes, J. D.; Winkler, R.; Lewis, B. B.; Stanford, M. G.; Plank, H.; Rack, P. D.; Simulation-Guided 3D Nanomanufacturing via Focused Electron Beam Induced Deposition. *American Chemical Society Nano*. **10**, 6163–6172 (2016).

[34] Donev, E. U.; Hastings, J. T.; Electron-Beam-Induced Deposition of Platinum from a Liquid Precursor. *Nano Letters*. **9**, 2715 (2009).

[35] Ding, W.; Diken, D. A.; Chen, X.; Piner, R. D.; Ruoff, R. S.; Zussman, E.; Mechanics of Hydrogenated Amorphous Carbon Deposits from Electron-Beam-Induced Deposition of a Paraffin Precursor. *Journal of Applied Physics*. **98**, 014905 (2005).

[36] Jackman, R. B.; Foord, J. S.; Electron Beam Stimulated Chemical Vapor Deposition of Patterned Tungsten Films on Si (100). *Applied Physics Letters*. **49**, 196 (1986).

[37] Bell, D. A.; Falconer, J. L.; Lű, Z.; McConica, C. M.; Electron Beam Induced Deposition of Tungsten. *Journal of Vacuum Science & Technology B*. **12**, 2976 (1994).

[38] Smith, D. A.; Fowlkes, J. D.; Rack, P. D.; Simulating the Effects of Surface Diffusion on Electron Beam Induced Deposition via a Three-Dimensional Monte Carlo Simulation. *Nanotechnology*. **19**, 415704 (2008).

[39] Fedorov, A. G.; Rykaczewski, K.; White, W. B.; Transport Issues in Focused Electron Beam Chemical Vapor Deposition. *Surface & Coatings Technology*. **201**, 8808-8812 (2007).

[40] Rykaczewski, K.; White, W. B.; Fedorov, A. G.; Analysis of Electron Beam Induced Deposition (EBID) of Residual Hydrocarbons in Electron Microscopy. Journal of Applied Physics. **101**, 054307 (2007).

[41] Matsui, S.; Kaito, T.; Fujita, J.; Komuro, M.; Kanda, K.; Haruyama, Y.; Three-Dimensional Nanostructure Fabrication By Focused-Ion-Beam Chemical Vapor Deposition. *Journal of Vacuum Science & Technology B.* **18**, 211-229 (2000).

[42] Bakker, G. L.; Hess, D. W.; Surface Cleaning and Carbonaceous Film Removal Using High Pressure, High Temperature Water, and Water/CO2 Mixtures. Journal of Electrochemical Society. **145**, 284-291 (1998).

[43] Rodenburg, C.; Jepson, M. A. E.; Bosch, E. G. T.; Dapor, M.; Energy Selective Scanning Electron Microscopy to Reduce the Effect of Contamination Layers on Scanning Electron Microscope Dopant Mapping. *Ultramicroscopy*. **110**, 1185 (2010).

[44] Watanabe, N.; Nittono, T.; Ito, H.; Kondo, N.; Nanishi, Y.; Surface Cleaning of C-Doped P GaAs With Hydrogen Electron Cyclotron Resonance Plasma. *Journal of Applied Physics*. **73**, 8146-8150 (1993).

[45] Hess, D. W.; Oxidation of Silicon in an Electron Cyclotron Resonance Oxygen Plasma: Kinetics, Physicochemical, And Electrical Properties. *Journal of Vacuum Science & Technology A*. **8**, (1990).

[46] Komatsu, S.; Kasamatsu, M.; Yamada, K.; Moriyoshi, Y.; Effects Of Plasma And/Or 193 Nm Excimer Laser Irradiation In Chemical Vapor Deposition Of Boron Films From B2H6+He. *Journal of Applied Physics*. **71**, (1992).

[47] Baker, M. A; Plasma Cleaning And The Removal Of Carbon From Metal Surfaces *Thin Solid Films*. **69**, 359 (1980).

[48] Jablonski, A.; Salvat, F.; Powell, C. J.; Differential Cross Sections for Elastic Scattering of Electrons by Atoms and Solids. *Journal of Electron Spectroscopy and Related Phenomena*. **137-140**, 299-303 (2004).

[49] Vasenkov, A. V.; Nonequilibrium Argon Plasma Generated by an Electron Beam. *Physical Review E*. **57**, 2212-2221 (1998).

[50] Gomer, R.; Diffusion of Adsorbates on Metal Surfaces. *Reports on Progress in Physics*. **53**, 917-1002 (1990).

[51] Wei, X. L.; Liu, Y.; Chen, Q.; Peng, L. M.; Controlling Electron-Beam-Induced Carbon Deposition on Carbon Nanotubes by Joule Heating. *Nanotechnology*. **19**, (2008).

[52] Matsuda, A.; Growth Mechanism of Microcrystalline Silicon Obtained from Reactive Plasmas. *Thin Solid Films*. 337 (1999).

[53] Koops, H. W. P.; Weiel, R.; Kern, D. P.; Baum, T. H.; High-Resolution Electron-Beam Induced Deposition. *Journal of Vacuum Science & Technology B.* **6**, 477-481 (1988).

[54] Hoyle, P. C.; Cleaver, J. R. A.; Ahmed, H.; Electron Beam Induced Deposition from $W(CO)_6$ at 2 to 20keV and Its Applications. *Journal of Vacuum Science & Technology B.* **1996,** *14*, 662-673 (1996).

[55] Botman, A.; Mulders, J. J. L.; Weemaes, R.; Mentink, S.; Purification of Platinum and Gold Structures after Electron-Beam-Induced Deposition. *Nanotechnology*. **17**, 3779 (2006).

[56] Sychugov, I.; Nakayama, Y.; Mitsuishi, K.; Composition Control of Electron Beam Induced Nanodeposits by Surface Pretreatment and Beam Focusing. *The Journal of Physical Chemistry C*. **113**, 21516-21519 (2009).

[57] Mulders, J. J. L.; Belova, L. M.; Riazanova, A.; Electron Beam Induced Deposition at Elevated Temperatures: Compositional Changes and Purity Improvement. *Nanotechnology*. **22**, 055302 (2011).

[58] Lai, K. K.; Lamb, H. H.; Tungsten Chemical Vapor Deposition Using Tungsten Hexacarbonyl: Microstructure of As-Deposited and Annealed Films. *Thin Solid Films*. **370,** *370*, 114-121 (2000).

[59] Córdoba, R.; Sesé, J.; De Teresa, J. M.; Ibarra, M. R.; High-Purity Cobalt Nanostructures Grown by Focused-Electron-Beam-Induced Deposition at Low Current. *Microelectronic Engineering*. **87**, 1550-1553 (2010).

[60] Henry, M. R.; Kim, S.; Rykaczewski, K.; Fedorov, A. G.; Inert Gas Jets for Growth Control in Electron Beam Induced Deposition. *Applied Physics Letters*. **98,** *98,* 263109 (2011).

[61] Flitsch, F. A.; Swanson, J. R.; Friend, C. M.; Thermal and Photoinduced Decomposition of $W(CO)_6$ on W(110) *Surface Science.* **245**, 85-95 (1991).

[62] Zaera, F.; Tungsten Hexacarbonyl Thermal Decomposition on Ni(100) Surfaces *Journal of Physical. Chemistry.* **96**, 4609-4615 (1992).

[63] Rosenberg, S. G.; Barclay, M.; Fairbrother, D. H.; Electron Induced Reactions of Surface Adsorbed Tungsten Hexacarbonyl ($W(CO)_6$) *Physical Chemistry Chemical Physics.* **15**, 4002-4015 (2013).

[64] Knapp, S. B.; Kinetics of the Thermal Decomposition of Tungsten Hexacarbonyl. *Ph.D. Thesis, Oregon State University, Corvallis, OR*. (1966).

[65] Lubman, D. M.; Rettner, C. T.; Zare, R. N.; How Isolated Are Molecules in a Molecular Beam? *Journal of Physical Chemistry.* **86**, 1129-1135 (1982).

[66] Durst, F.; Fluid Mechanics – An Introduction to the Theory of Fluid Flows. *Springer-Verlag: Berlin, Germany*. 351-355 (2008).

[67] Christen, W.; Rademann, K.; Even, U.; Efficient Cooling in Supersonic Jet Expansions of Supercritical Fluids: CO and $CO_2$. *Journal of Chemical Physics.* **125**, 174307 (2006).

[68] Warren, A.; Nylund, A.; Olefjord, I.; Oxidation of Tungsten and Tungsten Carbide in Dry and Humid Atmospheres. *International Journal. of Refractory Metals and Hard Materials.* **14**, 345-353 (1996).

[69] Cole, R. J.; Transmission Probability of Free Molecular Flow Through a Tube. *Rarefied Gas Dynamics; 10th International Symposium, Technical Papers. American Institute of Aeronautics and Astronautics*. 261-272 (1977).

[70] Lander, J. J.; Germer, L. H.; Plating Molybdenum, Tungsten, and Chromium by Thermal Decomposition of Their Carbonyls. *Transactions of the American Institute of Mining and Metallurgical Engineers*. **175**, 648-692 (1948).

[71] Bird, G. A.; Molecular Gas Dynamics and the Direct Simulation of Gas Flows. *2nd Ed. Gloucestershire; Clarendon.* (1994).

[72] Wanzenboeck, H. D.; Hochleitner, G.; Mika, J.; Gavagnin, M.; Bertagnolli, E.; Mapping of Local Argon Impingement on a Virtual Surface: an Insight for Gas Injection During FEBID. *Applied Physics A.* **117**, 1749 (2014).

[73] Utke, I.; Friedli, V.; Amorosi, S.; Michler, J.; Hoffmann, P.; Measurement and Simulation of Impinging Precursor Molecule Distribution in Focused Particle Beam Deposition/Etch Systems. *Microelectronic Engineering.* **83**, 1499 (2006).

[74] Kim, S.; Henry, M.; Fedorov, A. G.; Using an Energized Oxygen Micro-Jet for Improved Graphene Etching by Focused Electron Beam. *Applied Physics Letters.* **107**, 233102 (2015).

[75] Ivanov, M. S.; Markelovf, G. N.; Gimelshein, S. F.; Statistical Simulation of Reactive Rarefied Flows: Numerical Approach and Applications, *American Institute of Aeronautics and Astronautics Journal.* (1998).

[76] Wu, J. S.; Tseng, K. C.; Wu, F. Y.; Parallel Three-Dimensional DSMC Method Using Mesh Refinement and Variable Time-Step Scheme, *Computational Physics Communications*. **162**, 166–187 (2004).

[77] Darbandi, M.; Roohi, E.; Applying a Hybrid DSMC/Navier–Stokes Frame to Explore the Effect of Splitter Catalyst Plates in Micro/Nanopropulsion Systems. *Sensors and Actuators A.* **189**, 409-419 (2013).

[78] Garcia, A. L.; Bell, J. B.; Crutchfield, W. Y.; Alder, B. J.; Adaptive Mesh and Algorithm Refinement Using Direct Simulation Monte Carlo. *Journal of Computational Physics.* **154**, 134–155 (1999).

[79] Aktas, O.; Aluru, N. R.; A Combined Continuum/DSMC Technique for Multiscale Analysis of Microfluidic Filters, *Journal of Computational Physics*. **178**, 342–372 (2002).

[80] J.S. Wu, Y.Y. Lian, G. Cheng, R.P. Koomullil, K.C. Tseng, Development and Verification of a Coupled DSMC–NS Scheme Using Unstructured Mesh, J. Comput. Phys. 219 (2006) 579–607.

[81] Lian, Y. Y.; Chen, Y. S.; Tseng, K. C.; Wu, J. S.; Wu, B.; Yang, L.; Improved Parallelized Hybrid DSMC–NS Method, *Computers & Fluids*. **45**, 254–260 (2011).

[82] Li, Z.; Li, Z.; Li, H.; Yang, Y.; Jiang, X.; N-S/DSMC Hybrid Simulation of Hypersonic Flow over Blunt Body Including Wakes. *American Institute of Physics Conference Proceedings*. **1628**, 519-526 (2014).

[83] Henry, M. R.; Kim, S.; Fedorov, A. G.; High Purity Tungsten Nanostructures via Focused Electron Beam Induced Deposition with Carrier Gas Assisted Supersonic Jet Delivery of Organometallic Precursors. *The Journal of Physical Chemistry C*. **120**, 10584−10590 (2016).

[84] Meiburg, E.; Comparison of the Molecular Dynamics Method and the Direct Simulation Monte Carlo Technique for Flows around Simple Geometries. *The Physics of Fluids*. **29**, 3107 (1986).

[85] Liou, W. W.; Fang, Y.; Microfluid Mechanics – Principles and Modeling. *McGraw-Hill Nanoscience and Technology Series*. (2006).

[86] Tumuklu, O.; Levin, D. A.; Austin, J. M.; Shock-Shock Interactions for a Double Wedge Configuration in Different Gases. *Proceedings of the 53rd AIAA Aerospace Sciences Meeting, Florida.* (2015).

[87] Macrossan, M. N.; A Fast Simulation Method with Arbitrary Viscosity Law. *Proceedings of the 24th International Symposium on Rarefied Gas Dynamics, Italy*. (2004).

[88] Bird, G. A.; Monte-Carlo Simulation in an Engineering Context, *Progress in Astronautics and Aeronautics*. **74**, 239-255 (1981).

[89] Hash, D. B.; Moss, J. N.; Hassan, H. A.; Direct Simulation of Diatomic Gases Using the Generalized Hard Sphere Model, *Journal of Thermophysics and Heat Transfer*. **8**, 758-764 (1994).

[90] Koura, K.; Matsumoto, H.; Variable Soft Sphere Molecular Model for Inverse-Power-Law or Lennard-Jones Potential. *Physics of Fluids* A. **3**, 2459-2465 (1991).

[91] Moss, J. N.; DSMC Computations for Regions of Shock/Shock and Shock/Boundary Layer Interaction, *American Institute of Aeronautics and Astronautics Journal.* 1027 (2001).

[92] Nanbu, K.; Watanabe, Y.; Igarashi, S.; Conservation of Angular Momentum in the Direct Simulation Monte Carlo Method, *Journal of the Physical society of Japan*. **57**, 2877-2880 (1988).

[93] Bird, G. A.; Forty Years of DSMC, and Now? *American Institute of Physics Conference Proceedings*. **585**, 372-380 (2001).

[94] Kannenberg, K. C.; Boyd, I. D.; Strategies for Efficient Particle Resolution in the Direct Simulation Monte Carlo Method, Journal of Computational Physics. **157**, 727–745 (2000).

[95] Wilmoth, R. G.; Carlson, A. B.; LeBeau, G. J.; DSMC Grid Methodologies for Computing Low-Density, Hypersonic Flows about Reusable Launch Vehicles. *American Institute of Aeronautics and Astronautics Journal*. 1812 (1996).

[96] Robertson, S. J.; Willis, D. R.; Method-of-Characteristics Solution of Rarefied, Monatomic Gaseous Jet Expansion into a Vacuum. *American Institute of Aeronautics and Astronautics Journal*. **9**, 291-296 (1971).

[97] Buchner, F.; Flechtner, K.; Bai, Y.; Zillner, E.; Kellner, I.; Steinrück, H.; Marbach, H.; Gottfried, J. M.; Coordination of Iron Atoms by Tetraphenylporphyrin Monolayers and Multilayers on Ag(111) and Formation of Iron-Tetraphenylporphyrin. *The Journal of Physical Chemistry C.* **112**, 15458–15465 (2008).

[98] Gao, J.; Zhang, G.; Zhang, Y. W.; Exploring Ag(111) Substrate for Epitaxially Growing Monolayer Stanene: A First-Principles Study. *Scientific Reports.* **6**, 29107 (2016).

[99] Jung, D. H.; Kang, C.; Nam, J. E.; Jeong, H.; Lee, J. S.; Surface Diffusion Directed Growth of Anisotropic Graphene Domains on Different Copper Lattices. *Scientific Reports.* **6**, 21136 (2016).

[100] Ozhabes, Y.; Gunceler, D.; Arias, T. A.; Stability and Surface Diffusion at Lithium-Electrolyte Interphases with Connections to Dendrite Suppression. *Condensed Matter.* 1504.05799 (2015).

[101] Vicka, D.; Friedricha, L. J.; Dewa, S. K.; Bretta, M. J.; Robbiea, K.; Setoa, M.; Smy, T.; Self-Shadowing and Surface Diffusion Effects in Obliquely Deposited Thin Films. *Thin Solid Films.* **339**, 88-94 (1999).

[102] Barwicz, T.; Cohen, G. M.; Reuter, K. B.; Bangsaruntip, S.; Sleight, J. W.; Anisotropic Capillary Instability of Silicon Nanostructures Under Hydrogen Anneal. *Applied Physics Letters.* **100**, 093109 (2012).

[103] Day, R. W.; Mankin, M. N.; Gao, R.; No, Y. S.; Kim, S. K.; Bell, D. C.; Park, H. G.; Lieber, C. M.; Plateau–Rayleigh Crystal Growth of Periodic Shells on One-Dimensional Substrates. *Nature Nanotechnology.* **10**, 345-352 (2015).

[106] Grimmelmann, E. K.; Tully, J. C.; Cardillo, M. J.; Hard-Cube Model Analysis of Gas-Surface Energy Accommodation. *Journal of Chemical Physics.* **72**, 1039-1043 (1980).

[105] Arumainayagam, C. R.; Schoofs, G. R.; McMaster, M. C.; Madix, R. J.; Dynamics of Molecular Adsorption of Ethane with Pt(111): A Supersonic Molecular Beam Study. *The Journal of Physical Chemistry.* **95**, 1041-1047 (1991)

[106] Masel, R. I.; Principles of Adsorption and Reaction on Solid Surfaces. *New York; Wiley.* (1996).

[107] Nellis, G.; Klein, S; Heat Transfer. *New York; Cambridge University Press.* 204 (2009).

[108] Talu, O.; Myers, A. L; Reference Potentials for Adsorption of Helium, Argon, Methane, and Krypton in High-Silica Zeolites. *Colloids and Surfaces A.* ***187-188***, 83-93 (2001).

[109] Bernardes, C. E. S.; Lopes, J. N. C.; Piedade, M. E. M.; All-Atom Force Field for Molecular Dynamics Simulations on Organotransition Metal Solids and Liquids. Application to M(CO)n (M = Cr, Fe, Ni, Mo, Ru, or W) Compounds. *Journal of Physical Chemistry A.* **117**, (2013).

[110] Raghuraman, P.; Davidovits, P.; Velocity Slip of Gas Mixtures in Free Jet Expansions. *Physics of Fluids*. **21**, 1485-1489 (1978).

[111] Jesse, S.; Borisevich, A. Y.; Fowlkes, J. D.; Lupini, A. R.; Rack, P. D.; Unocic, R. R.; Sumpter, B. G.; Kalinin, S. V.; Belianinov, A.; Ovchinnikova, O. S.; Directing Matter: Toward Atomic-Scale 3D Nanofabrication. *American Chemical Society Nano*. **10**, 5600-5618 (2016).

[112] Narayanan, S.; Fedorov, A. G.; Joshi, Y. K. On-Chip Thermal Management of Hotspots Using a Perspiration Nanopatch. *Journal of Micromechanics and Microengineering*. **2010,** *20*, 075010.

[113] Macrossan, M. N.; μ-DSMC: A General Viscosity Method for Rarefied Flow. *Journal of Computational Physics.* **185**, 612-627 (2003)